MICROCOPY RESOLUTION TEST CHART

NATIONAL BUREAU OF STANDARDS-1963-A

AD-A142 383

ANALYSIS OF THE SUSPENDED H-WAVEGUIDE AND OTHER RELATED DIELECTRIC WAVEGUIDE STRUCTURES

T. N. TRINH
R. MITTRA

DTIC
ELECTE
JUN 2 5 1984
S
D
B

DTIC FILE COPY

LINOIS A   FAIGN

84   06   25   025

REPORT DOCUMENTATION PAGE		READ INSTRUCTIONS BEFORE COMPLETING FORM
1. REPORT NUMBER	2. GOVT ACCESSION NO. *AD-A142 383*	3. RECIPIENT'S CATALOG NUMBER
4. TITLE (and Subtitle) ANALYSIS OF THE SUSPENDED H-WAVEGUIDE AND OTHER RELATED DIELECTRIC WAVEGUIDE STRUCTURES		5. TYPE OF REPORT & PERIOD COVERED Technical Report
		6. PERFORMING ORG. REPORT NUMBER R-984;UILU-ENG 83-2205
7. AUTHOR(s) T. N. Trinh and R. Mittra		8. CONTRACT OR GRANT NUMBER(s) N0001479C-0424
9. PERFORMING ORGANIZATION NAME AND ADDRESS Coordinated Science Laboratory University of Illinois at Urbana-Champaign Urbana, IL 61801		10. PROGRAM ELEMENT, PROJECT, TASK AREA & WORK UNIT NUMBERS
11. CONTROLLING OFFICE NAME AND ADDRESS Joint Services Electronics Program		12. REPORT DATE January 1983
		13. NUMBER OF PAGES 153
14. MONITORING AGENCY NAME & ADDRESS(if different from Controlling Office)		15. SECURITY CLASS. (of this report) UNCLASSIFIED
		15a. DECLASSIFICATION/DOWNGRADING SCHEDULE

16. DISTRIBUTION STATEMENT (of this Report)

Approved for public release; distribution unlimited.

17. DISTRIBUTION STATEMENT (of the abstract entered in Block 20, if different from Report)

**DTIC
ELECTE
JUN 2 5 1984
B**

18. SUPPLEMENTARY NOTES

19. KEY WORDS (Continue on reverse side if necessary and identify by block number)

Millimeter-waves, Integrated circuits, Dielectric waveguide structures, Suspended waveguides

20. ABSTRACT (Continue on reverse side if necessary and identify by block number)

In this report, the field and propagation characteristics of many dielectric waveguide structures that are of direct importance to the areas of millimeter-wave integrated circuits are studied. A rigorous method of analysis of the propagation constants and the field distributions of a newly developed suspended H-waveguide based on the mode matching techniques is described. The derived eigenvalue equation for determining the propagation constant of this waveguide structure is very general and can be applied directly to other planar

DD FORM 1 JAN 73 **1473**

dielectric structures of rectangular cross section. However, for applications where only approximate values of the propagation constants are necessary, simple effective parameter approximations are employed. Even though the effective parameter approximations do not provide very accurate results for the propagation constants in some cases, they always provide useful information on the where-abouts and the existences of certain modes which, in turn, can be used as the initial values for iterating in the more rigorous mode matching technique. As frequency increases, the values obtained by the effective parameter technique approach those obtained by the mode matching method.

The loss characteristics of a suspended H-waveguide are also analyzed. The overall low loss figure of this waveguide structure promises wider applications in the millimeter-wave integrated circuits.

Finally, some essential integrable dielectric components, such as the dielectric resonators and the leaky-wave antennas, are studied. A theoretical formulation of the eigenvalue equation based on the spectral domain approach for determining the complex propagation constants of a slot leaky-wave antenna array constructed from a suspended H-waveguide is presented. A technique for improving the radiation characteristics of an image guide leaky-wave antenna is also described.

Accession For		
NTIS GRA&I	✓	
DTIC TAB	☐	
Unannounced	☐	
Justification		
By		
Distribution/		
Availability Codes		
Dist	Avail and/or Special	
A-1		

ANALYSIS OF THE SUSPENDED H-WAVEGUIDE AND

OTHER RELATED DIELECTRIC WAVEGUIDE STRUCTURES

by

T. N. Trinh and R. Mittra

iv

TABLE OF CONTENTS

Page

1. INTRODUCTION

The renewed interest in the millimeter-wave spectrum is due primarily to the recent advances in the development of solid state devices up to 300 GHz. Attempts have been made to utilize microwave technology in the millimeter-wave frequency range but only with limited successes. The conventional metal waveguides become very lossy and more difficult to fabricate as the wavelengths become shorter. Extremely tight surface tolerance requirements of metal waveguide components at millimeter-wave range contribute to the high cost of conventional systems. Microstrips and other forms of printed circuits have been used successfully at the lower millimeter-wave range [1],[2]. However, in the upper millimeter-wave bands, the extreme miniaturization of the center metal strip or the slot (in a slot-line) makes fabrication very difficult. The dielectric substrate thickness must be very small to avoid higher-order modes. The microstrip lines also suffer high metal loss due to the high concentration of the current density on the metal surfaces and near the edges of the metal strips. This has led to the investigation of alternate forms of low-loss low-cost dielectric-based waveguide designs suitable for integrated circuit applications at the millimeter-wave frequency range.

Several types of dielectric waveguide structures are currently available as the guiding medium for millimeter-wave applications, such as image guide [3], insular guide [4], H-guide [5], and trapped

image guide [6]. In this thesis, another form of dielectric wave-guide structure is presented--the suspended H-waveguide.

This suspended H-waveguide is similar in many ways to other waveguide structures. It consists of a guiding dielectric core with dielectric constant ϵ_2 sandwiched between two low-loss dielectric layers of dielectric constants ϵ_1 and ϵ_3 (see Fig. 1). The dielec-tric arrangement is then shielded to obtain a closed structure. In practice, these two insulating dielectric layers are metal-cladded dielectric sheets which are commercially available. Since $\epsilon_2 > \epsilon_1$, ϵ_3, most of the electromagnetic energy is carried in the guiding dielectric core, and therefore, the conductor loss is smaller than for the microstrip or image guide. Compared with other dielectric-based guiding structures mentioned above, the suspended H-waveguide enjoys a rigid mechanical support due to the metal enclosure. Also, the radiation loss is probably less than for other waveguide structures due to the closed metal walls. For this same reason, cross-talk among circuit elements can be eliminated. Presently, most of the com-mercial dielectric-base millimeter-wave ICs are shielded, hence, the metal surfaces around the suspended H-waveguide become a natural enclosure. Note that the side walls can be removed if the separation between the dielectric core and these walls is large enough. This allows the adjustment of the relative locations of the dielectric core and other components in the circuit without removing the top dielectric layer. The metal enclosure also allows plenty of ground for dc biasing in solid state applications. Ferrite applications,

3
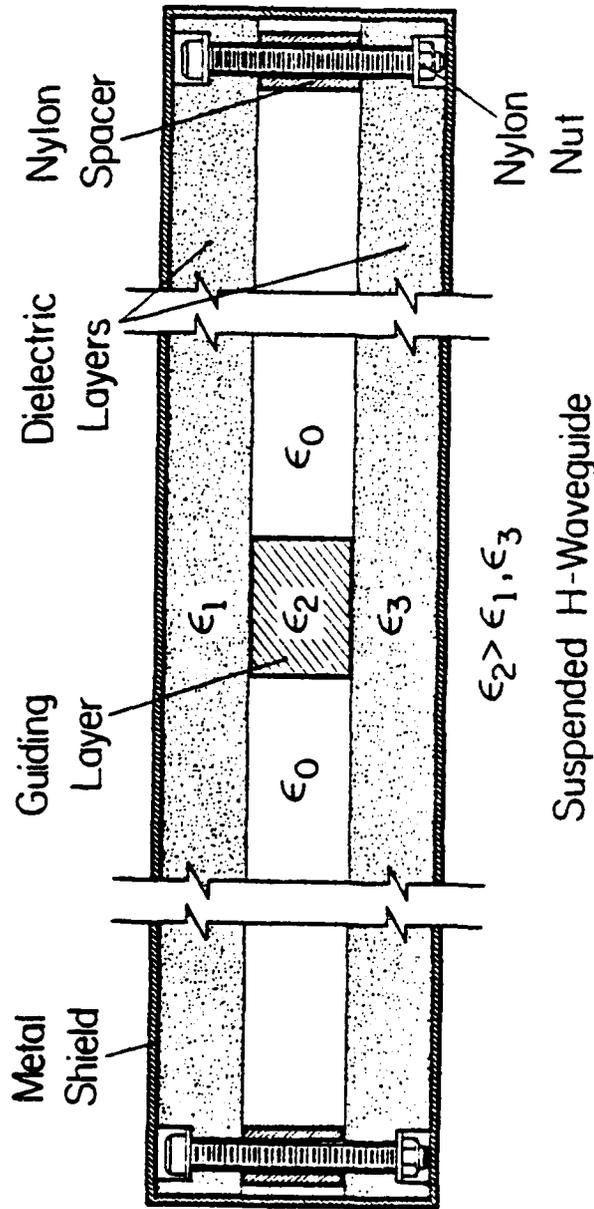
Figure 1. Suspended H-Waveguide.

such as the phase shifter or field displacement isolator, can readily be integrated since the top and bottom metal plates can be used to support a dc magnetic field. Bonding between dielectric materials may not be needed since the metal enclosure will secure all dielectric layers tightly in place.

Like any other oversized shielded waveguide structure, higher-order modes may arise. This situation may not be desirable for many applications. However, due to the unique structural arrangement, dielectric resonators can be used to eliminate the unwanted modes. Section 5.1 describes the designs of some modified dielectric resonators which can be used in circuits that employ the suspended H-waveguide.

In order to obtain reliable design information for the designs of both active and passive components derived from these waveguides, accurate theoretical predictions of the field and propagation characteristics must be available. A number of theoretical studies on the propagation properties of certain dielectric structures have been presented in the literature based on the effective permittivity and permeability [4],[7]-[9]. These methods are simple and usually provide reasonably accurate propagation information. However, they do not provide information on complete field distributions, and hence, certain loss characteristics. A rigorous mode-matching technique based on the field expansion in each subregion of the guide cross-section and the subsequent matching of the fields at the dielectric interfaces appeared recently in the literature [10]-[14]. Peng et al. [15] proposed a similar approach using the transverse resonant procedures.

In this thesis, a similar mode matching technique is applied to the investigation of the suspended H-waveguide. All relevant characteristic equations for the propagation constant of the waveguide . structure are given. It will be shown later that the field and propagation characteristics of other dielectric structures, such as image guide and insular guide, can be obtained directly from the formulation of the eigenvalue problem of the suspended H-wavegt ε. For generality, a coupled suspended H-waveguide is analyzed, which `n then be easily reduced to a single H-waveguide.

The loss characteristics of this waveguide structure are included in Chapter 4. Some components derived from the suspended H-waveguide are described in Chapter 5.

2. METHODS OF ANALYSIS

2.1 Mode Matching

2.1.1. Suspended H-Waveguide

The cross-section of a coupled suspended H-waveguide is shown in Figure 2a. For generality, the thickness of the top and bottom layers and their respective dielectric constants ε_1 and ε_3 are different. The width and the height of the dielectric core are 2w and 2h, respectively. The locations of the top and bottom conductor walls of the guide are d and 1. Because of the symmetry of the structure about the x = -a plane, even and odd modes can propagate in the coupled structure. The analysis of the coupled lines can then be reduced to that shown in Figure 2b where a perfect conducting (pec) wall implies odd mode propagation, and a perfect magnetic conducting (pmc) wall implies even mode propagation. For a = b, the coupled line reduces to that of a single uncoupled structure.

The analysis using the mode matching technique can be applied by separating the cross-section into five subregions (I)-(V). The fields in each region can be appropriately expanded in terms of regional eigenfunctions which satisfy the boundary conditions at the conductor walls. It is well-known that an infinite set of discrete modes is supported by an enclosed metal structure. Of these, only a small number of surface waves exist. The remainder are discrete higher-order modes some of which are propagating and the rest are below cut-off.
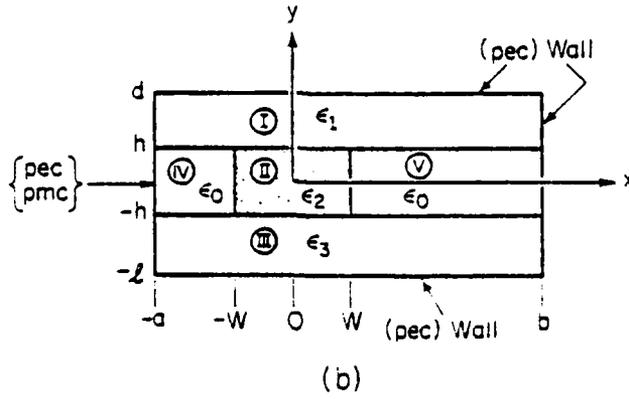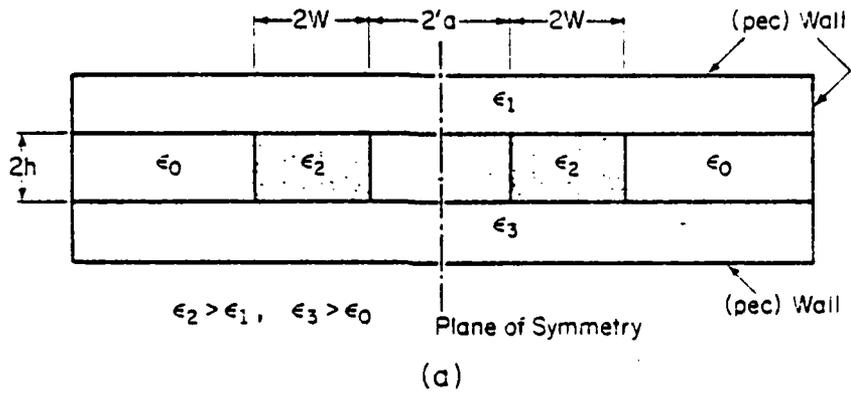
Figure 2. (a) Cross section of the coupled suspended H-waveguide.

(b) Structure adopted for analysis.

The total fields are derived from the Hertzian potentials Π_e and Π_h which have a single x-directed component [16]. The relationships between fields and potentials are:

$$E = \nabla \times \nabla \times \Pi_e - j\omega\mu_o \nabla \times \Pi_h \tag{1a}$$

$$H = j\omega\varepsilon_o\varepsilon_i \nabla \times \Pi_e + \nabla \times \nabla \times \Pi_h \tag{1b}$$

where ε_i is the relative dielectric constant of each region. Π_e and Π_h are referred to as longitudinal-section electric (LSE) mode and longitudinal-section magnetic (LSM) mode, respectively. Assuming that the propagation is in the z-direction, the field potential eigenfunctions can be expressed as follows ($\exp(-jk_z z)$ suppressed for clarity).

Region I

$$\Pi_e^{(1)} = \sum_{n=0}^{N} A_n \left\{ \begin{array}{c} \cos\left[k_{xn}^{(1)}(x+a)\right] \\ \sin\left[k_{xn}^{(1)}(x+a)\right] \end{array} \right\} \sin\left[k_{yn}^{(1)}(y-d)\right] / \sin\left[k_{yn}^{(1)}(h-d)\right] \tag{2a}$$

$$\Pi_h^{(1)} = \sum_{m=0}^{M} B_m \left\{ \begin{array}{c} \sin\left[\tilde{k}_{xm}^{(1)}(x+a)\right] \\ \cos\left[\tilde{k}_{xm}^{(1)}(x+a)\right] \end{array} \right\} \cos\left[\tilde{k}_{ym}^{(1)}(y-d)\right] / \cos\left[\tilde{k}_{ym}^{(1)}(h-d)\right] \tag{2b}$$

Region II

$$\Pi_e^{(2)} = \sum_{n=1}^{N'} \left[C_n \cos\left[k_{xn}^{(2)}x\right] + D_n\left[\sin k_{xn}^{(2)}x\right] \right] \sin\left[k_{yn}^{(2)}y\right] / \sin\left[k_{yn}^{(2)}h\right]$$

$$+ \sum_{n=1}^{N'} \left[C_n' \cos\left[k_{xn}^{(2)}x\right] + D_n'\left[\sin k_{xn}^{(2)}x\right] \right] \cos\left[k_{yn}^{(2)}y\right] / \cos\left[k_{yn}^{(2)}h\right] \tag{3a}$$

$$\pi_h^{(2)} = \sum_{m=1}^{M'} \left[E_m \sin\left(\tilde{k}_{xm}^{(2)} x\right) + F_m \cos\left(\tilde{k}_{xm}^{(2)} x\right) \right] \cos\left(\tilde{k}_{ym}^{(2)} y\right) / \cos\left(\tilde{k}_{ym}^{(2)} h\right)$$

$$+ \sum_{m=1}^{M'} \left[E_m' \sin\left(\tilde{k}_{xm}^{(2)} x\right) + F_m' \cos\left(\tilde{k}_{xm}^{(2)} x\right) \right] \sin\left(\tilde{k}_{ym}^{(2)} y\right) / \sin\left(\tilde{k}_{ym}^{(2)} h\right)$$

$$(3b)$$

Region III

$$\pi_e^{(3)} = \sum_{n=0}^{N} K_n \left\{ \begin{array}{c} \cos\left(k_{xn}^{(3)} (x+a)\right) \\ \sin\left(k_{xn}^{(3)} (x+a)\right) \end{array} \right\} \sin\left(k_{yn}^{(3)} (y+1)\right) / \sin\left(k_{yn}^{(3)} (-h+1)\right)$$

$$(4a)$$

$$\pi_h^{(3)} = \sum_{m=0}^{M} L_m \left\{ \begin{array}{c} x \sin\left(\tilde{k}_{xm}^{(3)} (x+a)\right) \\ \cos\left(\tilde{k}_{xm}^{(3)} (x+a)\right) \end{array} \right\} \cos\left(\tilde{k}_{ym}^{(3)} (y+1)\right) / \cos\left(\tilde{k}_{ym}^{(3)} (-h+1)\right)$$

$$(4b)$$

Region IV

$$\pi_e^{(4)} = \sum_{n=1}^{N'} \left\{ \begin{array}{c} \cos\left(k_{xn}^{(4)} (x+a)\right) \\ \sin\left(k_{xn}^{(4)} (x+a)\right) \end{array} \right\} \left[G_n \frac{\sin\left(k_{yn}^{(4)} y\right)}{\sin\left(k_{yn}^{(4)} h\right)} + G_n' \frac{\cos\left(k_{yn}^{(4)} y\right)}{\cos\left(k_{yn}^{(4)} h\right)} \right]$$

$$(5a)$$

$$\pi_h^{(4)} = \sum_{m=1}^{M'} \left\{ \begin{array}{c} \sin\left(\tilde{k}_{xm}^{(4)} (x+a)\right) \\ \cos\left(\tilde{k}_{xm}^{(4)} (x+a)\right) \end{array} \right\} \left[H_m \frac{\cos\left(\tilde{k}_{ym}^{(4)} h\right)}{\cos\left(\tilde{k}_{ym}^{(4)} h\right)} + H_m' \frac{\sin\left(\tilde{k}_{ym}^{(4)} y\right)}{\sin\left(\tilde{k}_{ym}^{(4)} h\right)} \right]$$

$$(5b)$$

Region V

$$\pi_e^{(5)} = \sum_{n=1}^{N'} \cos\left(k_{xn}^{(5)} (x-b)\right) \left[I_n \frac{\sin\left(k_{yn}^{(5)} y\right)}{\sin\left(k_{yn}^{(5)} h\right)} + I_n' \frac{\cos\left(k_{yn}^{(5)} y\right)}{\cos\left(k_{yn}^{(5)} h\right)} \right] \quad (6a)$$

$$\pi_h^{(5)} = \sum_{m=1}^{M'} \sin\left[\tilde{k}_{xm}^{(5)}(x-b)\right] \left[J_m \frac{\cos\left[\tilde{k}_{ym}^{(5)}y\right]}{\cos\left[\tilde{k}_{ym}^{(5)}h\right]} + J'_m \frac{\sin\left[\tilde{k}_{ym}^{(5)}y\right]}{\sin\left[\tilde{k}_{ym}^{(5)}h\right]} \right] \quad (6b)$$

These potentials have been chosen in such a way that the correspondent fields will satisfy all boundary conditions at the metal walls. In (2)-(6), $k_x^{(i)}$ and $k_y^{(i)}$ ($i = 1,2,3,4,5$) are the transverse wavenumbers for the LSM modes, and $\tilde{k}_x^{(i)}$ and $\tilde{k}_y^{(i)}$ ($i = 1,2,3,4,5$) are for the LSE modes. In (2), (3) and (4), the upper line in the brackets implies a pec wall at $x = -a$, while the lower line implies a pmc wall. The addition of the denominator terms in these potential functions greatly simplifies the final expressions of the eigenvalue equations obtained from the enforcing of the continuity conditions at the $y = h$ and $-h$ interfaces. An exact solution for the propagation constant and the field expressions can be obtained if N, N', M and M' are infinite. However, in practice, one must limit these values to finite numbers for numerical computations.

To satisfy the boundary conditions at both side walls, the transverse eigenvalues in regions I and III are given as follows.

	odd modes (pec at $x = -a$)	even mode (pmc at $x = -a$)
$k_{xn}^{(1)}$, $k_{xn}^{(3)}$	$\dfrac{n\pi}{a+b}$	$(n + \tfrac{1}{2})\dfrac{\pi}{a+b}$, $n = 0,1,2\ldots$
$\tilde{k}_{xm}^{(1)}$, $\tilde{k}_{xm}^{(3)}$	$\dfrac{m\pi}{a+b}$	$(m + \tfrac{1}{2})\dfrac{\pi}{a+b}$, $m = 0,1,2\ldots$

$$(7)$$

These odd (antisymmetric) and even (symmetric) modes are decoupled from each other and can exist independently in the coupled structure.

Furthermore, separate eigenvalue equations for $\tilde{k}_x^{(i)}$ and $\tilde{\tilde{k}}_x^{(i)}$ ($i = 2,4,5$) are obtained independently not only for LSE and LSM modes but also for the fields which are even and odd about the $y = 0$ plane.

Matching the tangential field components, which are derived from (1), across the interfaces at $x = \pm w$, for $-h \le y \le h$ yields different eigenvalue equations for $k_x^{(i)}$ and $\tilde{k}_x^{(i)}$:

<u>pec wall at x = -a</u>

$$\cos (A) \left\{ \chi_1 \cos (B) \sin (W) + \chi_2 \sin (B) \cos (W) \right\}$$
$$+ \chi_5 \sin (A) \left\{ \chi_3 \cos(B) \cos (W) + \chi_4 \sin (B) \sin (W) \right\} = 0 \tag{8}$$

<u>pmc wall at x = -a</u>

$$\chi_5 \cos (A) \left\{ \chi_3 \cos (B) \cos (W) + \chi_4 \sin (B) \sin (W) \right\}$$
$$- \sin (A) \left\{ \chi_1 \cos (B) \sin (W) + \chi_2 \sin (B) \cos (W) \right\} = 0 \tag{9}$$

where all parameters in Eqs. (8) and (9) are given as follows:

	LSM modes	LSE modes
A	$k_{xn}^{(4)}(-w+a)$	$\tilde{k}_{xm}^{(4)}(-w+a)$
B	$k_{xn}^{(5)}(w-b)$	$\tilde{k}_{xm}^{(5)}(w-b)$
W	$2k_{xn}^{(2)}w$	$2\tilde{k}_{xm}^{(2)}w$
χ_1	$k_{xn}^{(2)}/\varepsilon_2 k_{xn}^{(5)}$	1
χ_2	-1	$-\tilde{k}_{xm}^{(2)}/\tilde{k}_{xm}^{(5)}$

$$\tag{10}$$

	LSM modes	LSE modes
χ_3	1	1
χ_4	$\varepsilon_2\, k_{xn}^{(5)}/k_{xn}^{(2)}$	$\tilde{k}_{xm}^{(2)}/\tilde{k}_{xm}^{(5)}$
χ_5	1	$\tilde{k}_{xm}^{(2)}/\tilde{k}_{xm}^{(4)}$

and

$$\varepsilon_1 k_0^2 = k_z^2 + k_{xn}^{(1)^2} + k_{yn}^{(1)^2} = k_z^2 + \tilde{k}_{xm}^{(1)^2} + \tilde{k}_{ym}^{(1)^2} \tag{11a}$$

$$\varepsilon_2 k_0^2 = k_z^2 + k_{xn}^{(2)^2} + k_{yn}^{(2)^2} = k_z^2 + \tilde{k}_{xm}^{(2)^2} + \tilde{k}_{ym}^{(2)^2} \tag{11b}$$

$$\varepsilon_3 k_0^2 = k_z^2 + k_{xn}^{(3)^2} + k_{yn}^{(3)^2} = k_z^2 + \tilde{k}_{xm}^{(3)^2} + \tilde{k}_{ym}^{(3)^2} \tag{11c}$$

$$k_0^2 = k_z^2 + k_{xn}^{(4)^2} + k_{yn}^{(4)^2} = k_z^2 + \tilde{k}_{xm}^{(4)^2} + \tilde{k}_{ym}^{(4)^2} \tag{11d}$$

$$k_0^2 = k_z^2 + k_{xn}^{(5)^2} + k_{yn}^{(5)^2} = k_z^2 + \tilde{k}_{xm}^{(5)^2} + \tilde{k}_{ym}^{(5)^2} \tag{11e}$$

Also, by a simple comparison when applying the continuity conditions, it was found that the following relations hold:

$$k_{yn}^{(4)} = k_{yn}^{(2)} = k_{yn}^{(5)} = k_{yn} \tag{12a}$$

$$\tilde{k}_{ym}^{(4)} = \tilde{k}_{ym}^{(2)} = \tilde{k}_{ym}^{(5)} = \tilde{k}_{ym} \tag{12b}$$

There exist an infinite number of solutions for the eigenvalue equations (8) and (9). If all solutions are taken into account, the

expressions for the potentials in regions II, IV and V form a complete set to represent an exact field distribution in these regions. Each solution constitutes an eigenmode which represents a particular eigenfunction. $k_x^{(2)}$ and $\tilde{k}_x^{(2)}$ are always real which implies a transverse standing-wave within the dielectric core, whereas $k_x^{(i)}$ and $\tilde{k}_x^{(i)}$ ($i = 4,5$) can either be real or imaginary. The imaginary values represent the modes that decay exponentially away from the dielectric core. For each mode, the relations among the unknown coefficients of the field potentials in regions II, IV and V are obtained. For a reason which will become clear later, these amplitude coefficients are expressed in terms of those in region V. In other words, all unknown coefficients of regions II and IV now are represented by those in region V. For an LSM mode, the following relations hold:

$$\begin{Bmatrix} C_n \\ \\ C'_n \end{Bmatrix} = K_n^{(C-I)} \begin{Bmatrix} I_n \\ \\ I'_n \end{Bmatrix} \tag{13a}$$

$$\begin{Bmatrix} D_n \\ \\ D'_n \end{Bmatrix} = K_n^{(D-I)} \begin{Bmatrix} I_n \\ \\ I'_n \end{Bmatrix} \tag{13b}$$

$$\begin{Bmatrix} G_n \\ \\ G'_n \end{Bmatrix} = K_n^{(G-I)} \begin{Bmatrix} I_n \\ \\ I'_n \end{Bmatrix} \tag{13c}$$

where

$$K_n^{(C-I)} = -\frac{1}{\Delta_{LSM}} \frac{k_{xn}^{(2)}}{k_{xn}^{(4)}} \cos\left\{ k_{xn}^{(5)} (w-b) \right\} \tag{14a}$$

$$K_n^{(D-I)} = \frac{1}{\Delta_{LSM}} \left[-\frac{k_{xn}^{(2)}}{\epsilon_2 k_{xn}^{(4)}} \begin{Bmatrix} \cos\left[k_{xn}^{(4)}(-w+a)\right] \\ \sin\left[k_{xn}^{(4)}(-w+a)\right] \end{Bmatrix} \cos\left[k_{xn}^{(2)}w\right] \right.$$

$$\left. + \begin{Bmatrix} \sin\left[k_{xn}^{(4)}(-w+a)\right] \\ -\cos\left[k_{xn}^{(4)}(-w+a)\right] \end{Bmatrix} \sin\left[k_{xn}^{(2)}w\right] \right] \cos\left[k_{xn}^{(5)}(w-b)\right] \qquad (14b)$$

$$K_n^{(G-I)} = \frac{1}{\Delta_{LSM}} \left[\begin{Bmatrix} \sin\left[k_{xn}^{(4)}(-w+a)\right] \\ -\cos\left[k_{xn}^{(4)}(-w+a)\right] \end{Bmatrix} \cos\left[k_{xn}^{(2)}w\right] \right.$$

$$\left. + \frac{k_{xn}^{(2)}}{\epsilon_2 k_{xn}^{(4)}} \begin{Bmatrix} \cos\left[k_{xn}^{(4)}(-w+a)\right] \\ \sin\left[k_{xn}^{(4)}(-w+a)\right] \end{Bmatrix} \sin\left[k_{xn}^{(2)}w\right] \right] \cos\left[k_{xn}^{(5)}(w-b)\right]$$

$$(14c)$$

$$\Delta_{LSM} = \epsilon_2 \begin{Bmatrix} \sin\left[k_{xn}^{(4)}(-w+a)\right] \\ -\cos\left[k_{xn}^{(4)}(-w+a)\right] \end{Bmatrix} \sin\left[2k_{xn}^{(2)}w\right]$$

$$- \frac{k_{xn}^{(2)}}{k_{xn}^{(4)}} \begin{Bmatrix} \cos\left[k_{xn}^{(4)}(-w+a)\right] \\ \sin\left[k_{xn}^{(4)}(-w+a)\right] \end{Bmatrix} \cos\left[2k_{xn}^{(2)}w\right] \qquad (14d)$$

Likewise, for the LSE modes, the relationships among the unknown complex coefficients in regions II, IV and V are

$$\begin{Bmatrix} \Xi_m \\ E_m' \end{Bmatrix} = K_m^{(E-J)} \begin{Bmatrix} J_m \\ J_m' \end{Bmatrix} \qquad (15a)$$

$$\begin{bmatrix} F_m \\ F'_m \end{bmatrix} = K_m^{(F-J)} \begin{bmatrix} J_m \\ J'_m \end{bmatrix} \tag{15b}$$

$$\begin{bmatrix} H_m \\ H'_m \end{bmatrix} = K_m^{(H-J)} \begin{bmatrix} J_m \\ J'_m \end{bmatrix} \tag{15c}$$

where

$$K_m^{(E-J)} = \frac{1}{\Delta_{LSE}} \frac{\tilde{k}_{xm}^{(2)}}{\tilde{k}_{xm}^{(4)}} \sin\left[\tilde{k}_{xm}^{(5)}(w-b)\right] \tag{16a}$$

$$K_m^{(F-J)} = \frac{1}{\Delta_{LSE}} \left\{ -\frac{\tilde{k}_{xm}^{(2)}}{\tilde{k}_{xm}^{(4)}} \left\{ \begin{matrix} \sin\left[\tilde{k}_{xm}^{(4)}(-w+a)\right] \\ \cos\left[\tilde{k}_{xm}^{(4)}(-w+a)\right] \end{matrix} \right\} \sin\left[\tilde{k}_{xm}^{(2)}w\right] \right.$$

$$\left. + \left\{ \begin{matrix} \cos\left[\tilde{k}_{xm}^{(4)}(-w+a)\right] \\ -\sin\left[\tilde{k}_{xm}^{(4)}(-w+a)\right] \end{matrix} \right\} \cos\left[\tilde{k}_{xm}^{(2)}w\right] \right\} \sin\left[\tilde{k}_{xm}^{(5)}(w-b)\right] \tag{16b}$$

$$K_m^{(H-J)} = \frac{1}{\Delta_{LSE}} \left\{ \left\{ \begin{matrix} \cos\left[\tilde{k}_{xm}^{(4)}(-w+a)\right] \\ -\sin\left[\tilde{k}_{xm}^{(4)}(-w+a)\right] \end{matrix} \right\} \sin\left[\tilde{k}_{xm}^{(2)}w\right] \right.$$

$$\left. + \frac{\tilde{k}_{xm}^{(2)}}{\tilde{k}_{xm}^{(4)}} \left\{ \begin{matrix} \sin\left[\tilde{k}_{xm}^{(4)}(-w+a)\right] \\ \cos\left[\tilde{k}_{xm}^{(4)}(-w+a)\right] \end{matrix} \right\} \cos\left[\tilde{k}_{xm}^{(2)}\right] \sin\left[\tilde{k}_{xm}^{(5)}(w-b)\right] \right\} \tag{16c}$$

and

$$\Delta_{LSE} = \left\{ \begin{matrix} \cos\left[\tilde{k}_{xm}^{(4)}(-w+a)\right] \\ \sin\left[\tilde{k}_{xm}^{(4)}(-w+a)\right] \end{matrix} \right\} \sin\left[2\tilde{k}_{xm}^{(2)}w\right] + \frac{\tilde{k}_{xm}^{(2)}}{\tilde{k}_{xm}^{(4)}} \left\{ \begin{matrix} \sin\left[\tilde{k}_{xm}^{(4)}(-w+a)\right] \\ \cos\left[\tilde{k}_{xm}^{(4)}(-w+a)\right] \end{matrix} \right\} \cos\left[2\tilde{k}_{xm}^{(2)}w\right]$$
$$\tag{16d}$$

In (14)-(16), the upper line inside the brackets applies to the
pec wall at x = -a (odd modes), and the lower to the pmc wall (even
modes).

The total fields of the composite structure and the longitudinal
propagation constant can now be obtained by matching the tangential
field components at the plane y = ±h. In order to satisfy the boundary
conditions for all modes, the tangentials E_x, H_x, E_z and H_z must be
all taken into consideration. Using Eqs. (1)-(6), the resulting
eight equations are shown in Appendix A. These equations shall contain
the x-dependence which is different for each region. The x-variation
in each expansion function in regions I and III is chosen to be a
sine or cosine type harmonic function to simultaneously satisfy the
boundary conditions at both side walls. By appropriately multiplying
these functions with either $\sin\left[k_x^{(i)}(x+a)\right]$ or $\cos\left[k_x^{(i)}(x+a)\right]$, i = 1,3,
where $k_x^{(i)}$ are given in (7), and integrating over x from -a to b and
using the orthogonality properties of these expansion functions, a
system of homogeneous linear equations with unknown coefficients
A_n, B_m, K_n, L_m, I_n, I_n', J_m and J_m' is obtained. To reduce the total
number of equations, A_n, B_m, K_n and L_m, which were derived from Eqs.
(A-1), (A-2), (A-5), and (A-6), will be substituted into the remaining
four equations. Assuming an equal number of LSE modes in all regions
(i.e., M = M') and also an equal number of LSM modes (i.e., N = N'),
the reduced system 2(N+M) homogeneous linear equations with unknown
coefficients I_n, I_n', J_m and J_m' become:

$$\left\{ k_z \sum_{n=1}^{N} \left[I_n(\nu) + \frac{k_{x\nu}^{(1)} \begin{Bmatrix} -1 \\ 1 \end{Bmatrix}}{\left(\epsilon_1 k_0^2 - k_{x\nu}^{(2)^2}\right)} P_n(\nu) \right] \right\} (I_n + I_n')$$

$$+ \omega\mu_o \sum_{m=1}^{M} \left\{ \frac{\tilde{k}_{y\mu}^{(1)}}{\left(\epsilon_1 k_o^2 - \tilde{k}_{x\mu}^{(1)^2}\right)} \frac{\tan\left[\tilde{k}_{y\mu}^{(1)}(h-d)\right]}{} Q_m(\mu) - \tilde{k}_{ym} \tan(\tilde{k}_{ym}h) U_m(\mu) \right\} J_m$$

$$+ \omega\mu_o \sum_{m=1}^{M} \left\{ \frac{\tilde{k}_y^{(1)}}{\left(\epsilon_1 k_o^2 - \tilde{k}_{x\mu}^{(1)^2}\right)} \frac{\tan\left[\tilde{k}_y^{(1)}(h-d)\right]}{} Q_m(\mu) + \tilde{k}_{ym} \cot(\tilde{k}_{ym}h) U_m(\mu) \right\} J_m' = 0$$

$$(17)$$

$$\omega\epsilon_o \sum_{n=1}^{N} \left\{ k_{yn} \cot(k_{yn}h) R_n(\nu) - \frac{\epsilon_1 k_{y\nu}^{(1)} \cot\left[k_{y\nu}^{(1)}(h-d)\right] P_n(\nu)}{{}_1 k_o^2 - k_x^{(1)^2}} \right\} I_n$$

$$- \omega\epsilon_o \sum_{n=1}^{N} \left\{ k_{yn} \tan(k_{yn}h) R_n(\nu) + \frac{\epsilon_1 k_{y\nu}^{(1)} \cot\left[k_{y\nu}^{(1)}(h-d)\right] P_n(\nu)}{\left(\epsilon_1 k_o^2 - k_{x\nu}^{(1)^2}\right)} \right\} I_n'$$

$$+ \sum_{m=1}^{M} k_z \left\{ S_m(\mu) + \frac{\tilde{k}_{x\mu}^{(1)} Q_m(\mu) \begin{Bmatrix} -1 \\ 1 \end{Bmatrix}}{\left(\epsilon_1 k_o^2 - \tilde{k}_x^{(1)^2}\right)} \right\} (J_m + J_m') = 0 \qquad (18)$$

$$\sum_{n=1}^{N} k_z \left[T_n(\nu) + \frac{k_{x\nu}^{(3)} \begin{Bmatrix} -1 \\ 1 \end{Bmatrix} P_n(\nu)}{\left(\epsilon_3 k_o^2 - k_{x\nu}^{(3)^2} \right)} \right] (-I_n + I_n')$$

$$+ \omega\mu_o \sum_{m=1}^{M} \left[\tilde{k}_{ym} \tan(\tilde{k}_{ym}h) U_m(\mu) + \frac{\tilde{k}_{yu}^{(3)} \tan\left(\tilde{k}_{yu}^{(3)}(-h+1) \right)}{\left(\epsilon_3 k_o^2 - \tilde{k}_{xu}^{(3)^2} \right)} Q_m(\mu) \right] J_m$$

$$+ \omega\mu_o \sum_{m=1}^{M} \left[\tilde{k}_{ym} \cot(\tilde{k}_{ym}h) U_m(\mu) - \frac{\tilde{k}_{yu}^{(3)} \tan\left(\tilde{k}_{yu}^{(3)}(-h+1) \right)}{\left(\epsilon_3 k_o^2 - \tilde{k}_{x}^{(3)^2} \right)} Q_m(\mu) \right] J_m' = 0 \tag{19}$$

$$\omega\epsilon_o \sum_{n=1}^{N} \left[k_{yn} \cot(k_{yn}h) R_n(\nu) + \frac{\epsilon_3 k_{y\nu}^{(3)} \cot\left(k_{y\nu}^{(3)} \cot k_{y\nu}^{(3)}(-h+1) \right)}{\left(\epsilon_3 k_o^2 - k_{x\nu}^{(3)^2} \right)} P_n(\nu) \right] I_n$$

$$+ \omega\epsilon_o \sum_{n=1}^{N} \left[k_{yn} \tan(k_{yn}h) R_n(\nu) - \frac{\epsilon_3 k_{y\nu}^{(3)} \cot\left(k_{y\nu}^{(3)}(-h+1) \right)}{\left(\epsilon_3 k_o^2 - k_{x\nu}^{(3)^2} \right)} P_n(\nu) \right] I_n'$$

$$+ \sum_{m=1}^{M} k_z \left[S_m(\mu) + \frac{\begin{Bmatrix} -1 \\ 1 \end{Bmatrix} \tilde{k}_{xu}^{(3)} Q_m(\mu)}{\left(\epsilon_3 k_o^2 - \tilde{k}_{xu}^{(3)^2} \right)} \right] (J_m - J_m') = 0 \tag{20}$$

where

$$\nu = 0, \ldots N-1$$

$$\mu = \begin{cases} 1,\ldots M & \text{for pec wall} \\ 0,\ldots M-1 & \text{for pmc wall} \end{cases}$$

The upper value in the brackets applies to the pec wall at $x = -a$,
while the lower line applies to the pmc wall. $P_n(\nu),\ldots,U_m(\mu)$ are
the coupling integral terms relating the regions [11], and are shown in
Appendix B. The zeroes of the determinant of these $2(N+M) \times 2(N+M)$
homogeneous equations are the longitudinal propagation constants k_z's
of the composite waveguide structure. In (17)-(20), $k_x^{(i)}$, $k_y^{(i)}$, $\tilde{k}_x^{(i)}$
and $\tilde{k}_y^{(i)}$ are related to k_z according to (11). For each k_z, a set of
amplitude coefficients $A_n,\ldots,L_m$ are found within a constant multi-
plicative factor and, hence, a complete description of the total field
in the guide via the potential functions. It should be mentioned that
the approach to formulate the eigenvalue problem for determining the
propagation constant of the suspended H-waveguide described in this
section can also be extended to other more complicated structures whose
shapes and boundaries are rectilinear and parallel to either the x-
or the y-axis [10].

2.1.2. Related Planar Dielectric Waveguides

The system of homogeneous equations derived for the suspended
H-waveguide can directly be applied to other popular rectangular
cross-section dielectric waveguide structures as shown in Figure 3.
Since the expansion functions of the potentials in the dielectric
core region of the suspended H-waveguide are composed of both symmetric

20
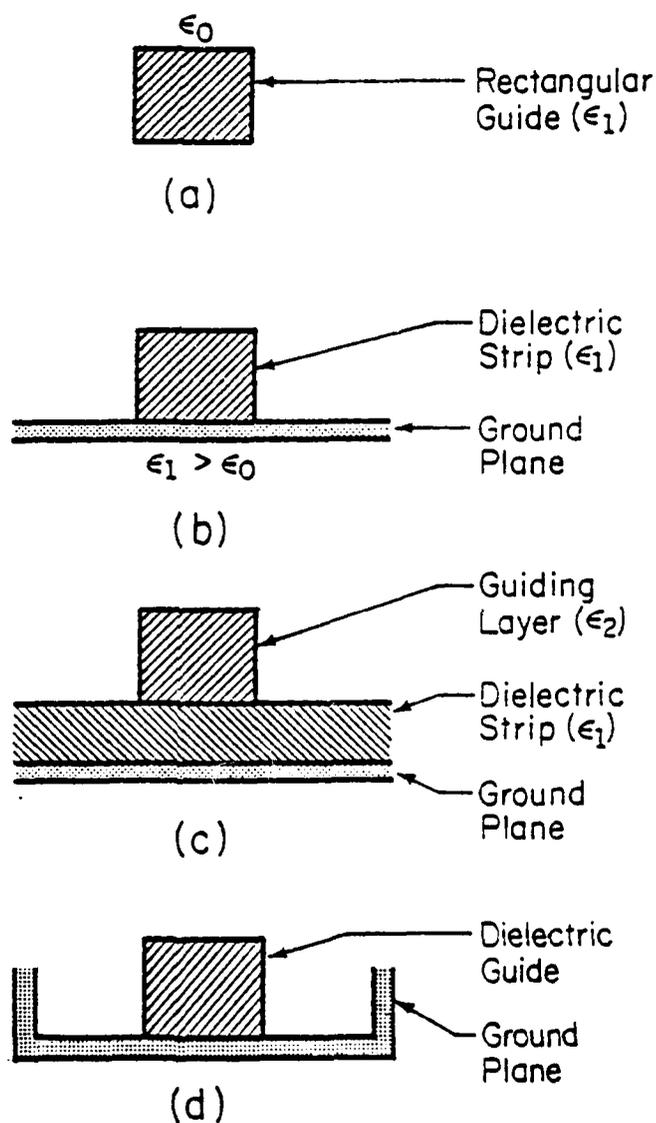
Figure 3. Other dielectric waveguide structures:

(a) Dielectric rectangular guide. (b) Image guide.

(c) Insular guide. (d) Partially-filled dielectric

trough waveguide.

and antisymmetric functions with respect to the y-axis, only a portion of (17)-(20) is needed to calculate the propagation constants of the waveguide structures shown in Figures 3a, 3b, and 3d, whose physical ground planes coincide with the y-axis. (The rectangular dielectric guide is equivalent to an image guide with twice the aspect ratio of the dielectric guide.) To analyze these structures, the top dielectric layer (ε_1) is replaced by free-space, and the top metal ground plane is moved further away from the dielectric core to minimize its effect on the propagation characteristics. By rearranging Eqs. (17)-(20) into a matrix form, it is easy to isolate the symmetric and nonsymmetric parts, i.e.,

$$\left(\begin{array}{c|c} M_1 & M_2 \\ \hline M_3 & M_4 \end{array} \right) \left(\begin{array}{c} I_n \\ J_m \\ \hline I_n' \\ J_m' \end{array} \right) = 0 \tag{21}$$

All coefficients of the matrix in (21) are given in (17)-(20). The amplitude coefficients with subscript n represent the LSM modes, and subscript m the LSE modes. A quick observation reveals that the equations that correspond to the coefficients of the submatrix in the first or third quadrant of expression (21) are indeed the eigenvalue equations of the structures shown in Figures 3a, b and d, i.e.,

$$\left(M_1 \right) \left(\begin{array}{c} I_n \\ J_m \end{array} \right) = 0 \tag{22}$$

The analysis has so far been for a coupled structure. It can be reduced to that of an uncoupled guide simply by moving the left side wall (at $x = -a$) to infinity. However, in actual calculation, the left side wall will be moved up against the dielectric core, since in a single guide, the fields can also be even or odd with respect to their centers. A pmc wall at $x = -w$ will generate a family of even modes in a guide whose total width is now $4w$. Likewise, a pec wall at $x = -w$ corresponds to a family of odd modes with respect to this new guide center. By doing this, the computation can be minimized since the number of LSE and LSM eigenmodes necessary to satisfy the continuity conditions at interfaces of regions increases with increasing ratio $(a+b)/2w$. Further discussion on this subject is given in a later section along with numerical results.

2.2 Effective Permittivity and Permeability Approximations

The mode matching technique described above will yield accurate results for both the field descriptions and the propagation constants if enough terms are taken into account. This procedure is quite involved, and unless enough terms are used, the final results may be in doubt. For many practical engineering applications, where only sufficiently accurate values of k_z are necessary, the "effective" permittivity or permeability approximation or a combination of the two is quite useful. Even though they do not provide field information, reasonably accurate results for the propagation constants of many complex structures are obtained [4],[12],[15],[17]. The techniques

described here are actually a modification of a one-term approxima-
tion of the mode matching technqiue. They consider two types of modal
fields, i.e., LSE (H-wave) and LSM (E-wave) modes, independently.
The H-wave leads to the effective dielectric constant (or permittivity)
method while the E-wave is associated with the effective permeability
method [9]. For abbreviation, when we refer to both the effective
permittivity and the effective permeability and their mean values,
the effective parameter will be used. The general applications of
these approximations can be found in all references cited above. How-
ever, it would be appropriate to reintroduce the fundamental concepts
again to facilitate their applications. Consider an H-wave (LSE-to-z)
obliquely incident upon an infinite interface between two dielectric
media I and II with relative dielectric constants and permeabilities
ϵ_1, ϵ_2, u_1 and μ_2, respectively (see Fig. 4a). The reflection (and
transmission) coefficient of this obliquely incident case can be ob-
tained from that of an equivalent "effective" normally incident one
(see Fig. 4b) if an appropriate "effective dielectric constant" can
be found, i.e.,

$$\frac{E_r}{E_i} = \frac{\left(\frac{\epsilon_1^*}{u_1}\right)^{\frac{1}{2}} - \left(\frac{\epsilon_2^*}{u_2}\right)^{\frac{1}{2}}}{\left(\frac{\epsilon_1^*}{\mu_1}\right)^{\frac{1}{2}} + \left(\frac{\epsilon_2^*}{u_2}\right)^{\frac{1}{2}}} \tag{23}$$

For an H-wave, it is apparent that the "effective" concept is valid
if the effective dielectric constants in (23) are replaced by:

24
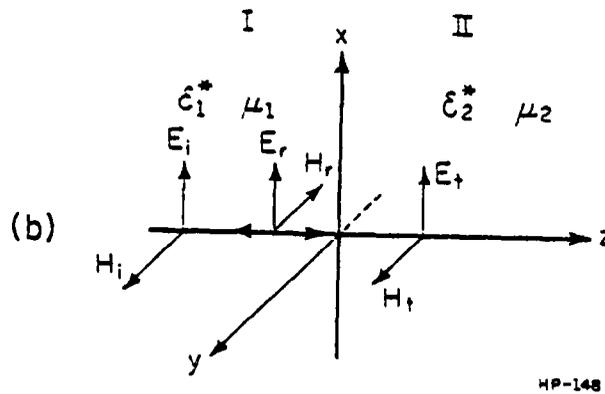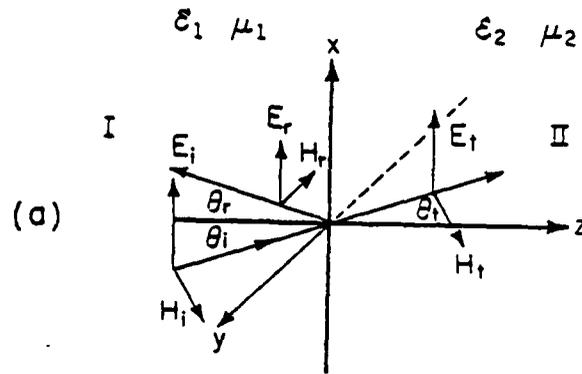
Figure 4. (a) TE obliquely incident wave.

(b) Equivalent normal incident wave using the effective dielectric constant.

$$\varepsilon_i^* = \varepsilon_i - \frac{1}{\mu_i} \left(\frac{k_{yi}}{k_o} \right)^2 \quad , \quad i = 1,2 \tag{24}$$

where k_o is the free-space wavenumber, and k_{yi} is the phase constant in the y-direction, i.e., $k_{yi} = (\varepsilon_i \mu_i)^{\frac{1}{2}} k_o \sin\theta_i$.

For an E-wave (TM) obliquely incident from medium I into II (see Fig. 5a), the equivalent normal incident wave (see Fig. 5b) for the reflection (and transmission) coefficient is obtained if the relative permeability in each medium is replaced by

$$\mu_i^* = \mu_i - \frac{1}{\varepsilon_i} \left(\frac{k_{yi}}{k_o} \right)^2 \quad , \quad i = 1,2 \tag{25}$$

In short, the effective dielectric constant (permittivity) must be used for the E-wave and the effective permeability for the H-wave. Unlike the mode-matching technique, the effective parameter approach assumes that there is no coupling between the LSE- and LSM-modes. This, in effect, assumes that the geometrical discontinuities in a dielectric guide occur (alternatively) in one plane only.

This approximate technique will now be applied to the suspended H-waveguide. Consider an LSM (TM-to-y) mode propagating in a coupled structure as shown in Figure 6a. Since this is an LSM-mode, the effective permeability will be utilized. The discontinuities in the y-direction are first ignored, and the dielectric core region (II) is extended to infinity (see Fig. 6b) so that the characteristic equations for k_x can be obtained from this two-dimensional dielectric slab. The characteristic equations for k_x have already been derived
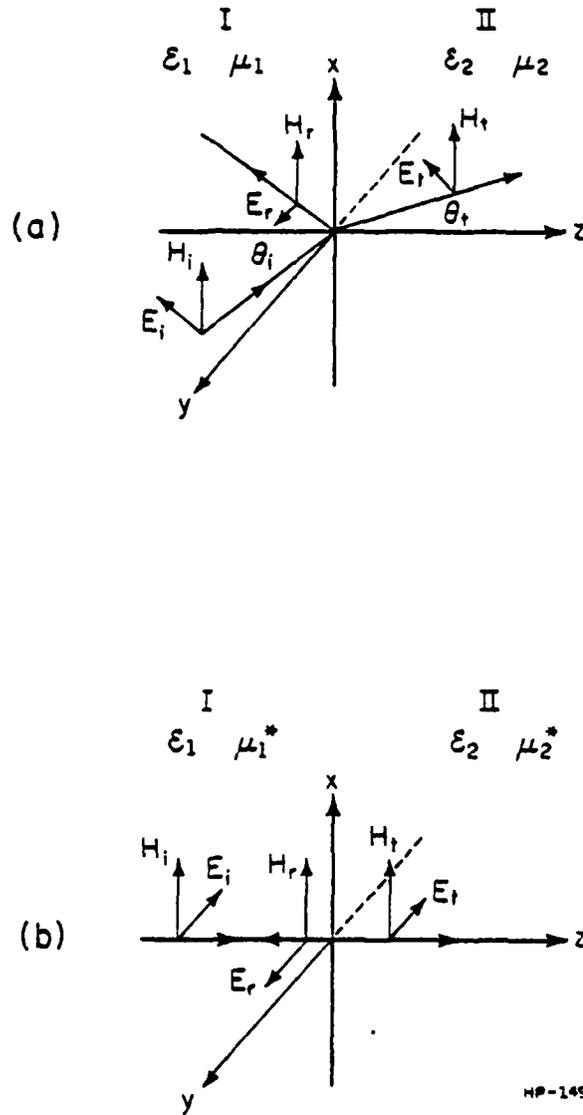
Figure 5. (a) TM obliquely incident wave.

(b) Equivalent normal incident using the effective permeability.
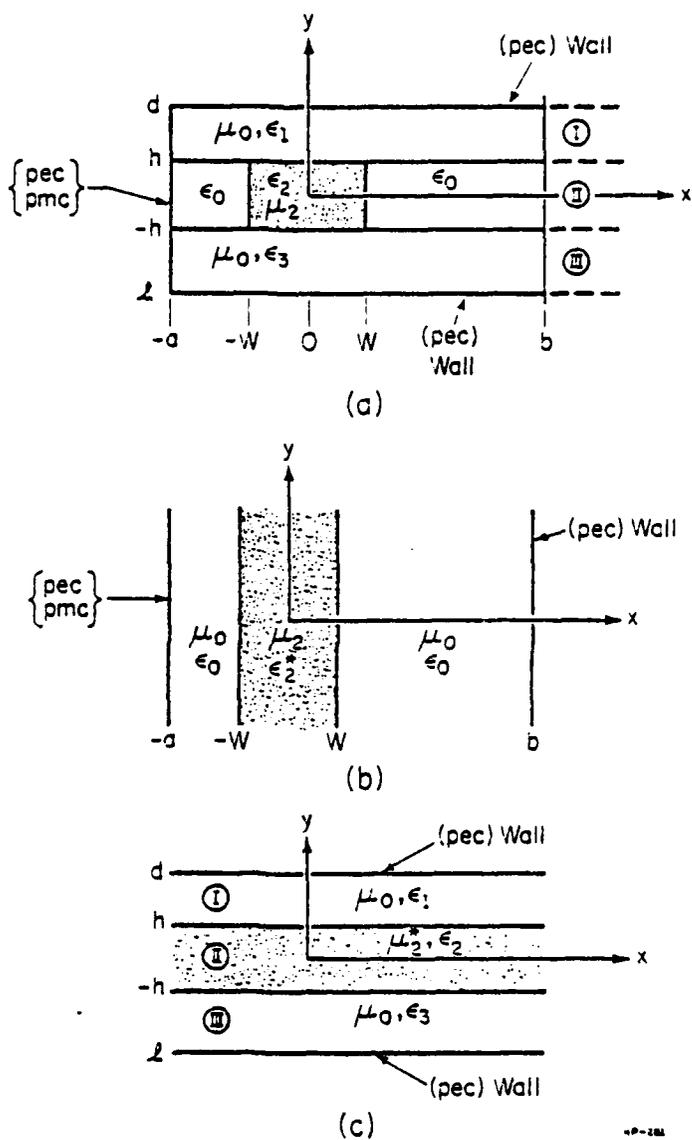
Figure 6. (a) Cross-sectional structure adopted for the effective parameter approximations.

(b), (c) Models for calculating k_x and k_y, respectively.

in Eqs. (8) and (9). Once k_x is obtained, the "effective" permeability
is defined according to (25). (Note that the coordinate system in
Fig. 6 is different from that as shown in Figs. 4 and 5.) In this case,
μ_2^* is given by

$$\mu_2^*(x) = \mu_o - \frac{1}{\varepsilon_2}\left[\frac{k_x^{(2)}}{k_o}\right]^2 \tag{26}$$

The dielectric core region is now replaced by an infinite slab with
an effective permeability μ_2^* (see Fig. 6c). If tangentials H_x and E_z
are matched at the planes $y = \pm h$, the characteristic equation for k_y is
obtained:

$$\cos\left(2k_y^{(2)}h\right)\left\{\varepsilon_1\frac{k_y^{(2)}}{k_y^{(1)}}\cos\left[k_y^{(1)}(h-d)\right]\sin\left[k_y^{(3)}(-h+1)\right]\right.$$
$$\left. - \varepsilon_3\frac{k_y^{(2)}}{k_y^{(3)}}\sin\left[k_y^{(1)}(h-d)\right]\cos\left[k_y^{(3)}(-h+1)\right]\right\}$$
$$+ \sin\left(2k_y^{(2)}h\right)\left\{\varepsilon_2\sin\left[k_y^{(1)}(h-d)\right]\sin\left[k_y^{(3)}(-h+1)\right]\right.$$
$$\left. + \frac{\varepsilon_1\varepsilon_3}{\varepsilon_2}\frac{k_y^{(2)}{}^2}{k_y^{(1)}k_y^{(3)}}\cos\left[k_y^{(1)}(h-d)\right]\cos\left[k_y^{(3)}(-h+1)\right]\right\} = 0 \tag{27}$$

where the transverse propagation constants $k_y^{(i)}$, $i = 1,2,3$, are related
by

$$k_z^2 = \varepsilon_1 k_o^2 + k_y^{(1)}{}^2 = \varepsilon_2\mu_2^*(x)\,k_o^2 + k_y^{(2)} = \varepsilon_3 k_o^2 + k_y^{(3)} \tag{28}$$

In Eq. (27), $k_y^{(i)}$ can be solved numerically. k_z and, hence, the dispersion characteristics of the original H-waveguide can then be calculated according to (28).

For LSE^x (TE-to-x) mode, the process is reversed. Using the effective permittivity approach, the procedure for obtaining the longitudinal propagation constant k_z is described as follows:

$$\text{Fig. 6C} \xrightarrow{\text{Eq. (27)}} k_y^{(i)} \xrightarrow{\varepsilon_2^*(y)} \text{Fig. 6b} \xrightarrow{\text{Eqs. (8) \& (9)}} k_x^{(i)}$$

and the following relation:

$$k_z^2 = \varepsilon_2^*(y) \; k_o^2 - k_x^{(2)^2} = k_o^2 - k_x^{(5)^2} \tag{29}$$

The LSE^y and LSM^x modes can be obtained in the same manner by considering

$$LSE^y \; : \; k_x \xrightarrow{\varepsilon_2^*(x)} k_y, k_z$$

$$LSM^x \; : \; k_y \xrightarrow{\mu_2^*(y)} k_x, k_z \tag{30}$$

The characteristic equations for k_y of these two modes are

$$\cos\left(2k_y^{(2)}h\right)\left\{\frac{k_y^{(2)}}{k_y^{(1)}} \sin\left(k_y^{(1)}(h-d)\right) \cos\left(k_y^{(3)}(-h+1)\right)\right.$$

$$\left. - \frac{k_y^{(2)}}{k_y^{(3)}} \cos\left(k_y^{(1)}(h-d)\right) \sin\left(k_y^{(3)}(-h+1)\right)\right\}$$

$$- \sin\left(2k_y^{(2)}h\right)\left\{\cos\left(k_y^{(1)}(h-d)\right) \cos\left(k_y^{(3)}(-h+1)\right)\right.$$

$$\left. + \frac{k_y^{(2)^2}}{k_y^{(1)}k_y^{(3)}} \sin\left(k_y^{(1)}(-h+d)\right) \sin\left(k_y^{(3)}(-h+1)\right)\right\} = 0 \tag{31}$$

In summary, the effective parameter approximations are based on three basic assumptions:

1) Only one surface-wave type (either LSE or LSM) can propagate.

2) Each region in the guide can alternatively be treated as a two-dimensional problem, i.e., there is no geometrical discontinuity on one side while investigating the other.

3) $\varepsilon_2 > \varepsilon_1, \varepsilon_3$

The characteristic equations for the propagation constants derived here can be applied to the other guiding structures shown in Figure 3 simply by changing the separation of certain side-wall locations and the relative dielectric constants of certain regions. Usually, the actual value of k_z (using mode-matching technique) lies somewhere between those obtained by the effective permeability and permittivity approximations. An average, e.g., geometrical mean, of these approximate values often produces a more accurate result. Numerical values obtained by the effective parameter approximations and the more rigorous mode matching technique are presented in the next section.

3. NUMERICAL AND EXPERIMENTAL RESULTS

In this chapter, the numerical computations of the propagation constant and field distribution of different waveguide structures are discussed. All calculations were done using the Vax 11/780 computer. Some experimental results are also presented.

3.1 Normalized Propagation Constant of Single and Coupled Suspended H-Waveguides

In an open dielectric waveguide structure, the range of the normalized propagation constant k_z/k_o is between 1 and $\sqrt{\varepsilon_2}$. Any mode with a normalized propagation less than one is a leaky mode. This is the cut-off condition of any normal mode in an open dielectric struc-ture. This phenomenon is not applicable to a partially dielectric-filled shielded structure whose propagation starts at k_z/k_o equal to zero. However, unlike the hollow metal waveguide, the guided modes in a partially dielectric-filled metal structure are neither pure TE nor TM. Therefore, another mode description must be used. In this thesis, the field modes are described as E_{mn}^y if the major transverse electric field is parallel to the y-axis and as E_{mn}^x if the major transverse electric field is parallel to the x-axis. The m and n subscripts are the number of maxima of the dominant electric field in the x- and y-direction, respectively. Due to the high dielectric constant of the core and the large size of the metal shield, the suspended H-waveguide can be considered as an oversized waveguide that can theoretically support few higher-order modes at the upper millimeter-wave frequency range. Unlike the fundamental mode, where a large percentage of the

energy propagating in the guide is concentrated in the dielectric core,

and decays exponentially away from the core, the higher-order modes

are loosely bounded within the dielectric core causing most of the energy

to be concentrated outside the core. Unless over-moded operation

is desired, most of these higher-order modes can be eliminated by

proper launching into and receiving from the guide. A thin absorbing

film can also be placed at the inner side walls to damp out the modes

with lateral expansion far beyond the dielectric core that are not

permitted for normal propagation [5]. Because of the large separation

between the core and the side walls, these absorbing films should not

have any effect on the propagation of the fundamental mode. As

frequency increases, many of these higher-order modes become tightly

bound to the dielectric core as in the case of an open dielectric

waveguide structure. For practical means, however, only the funda-

mental modes of two different polarizations will be investigated in

great detail in this thesis. Figure 7 shows the influence of the side-

wall location on the propagation constants of the dominant E_{11}^y and E_{11}^x

modes in a single suspended H-waveguide. Unless otherwise indicated,

in this and many following figures, the top and bottom dielectric

layers are the same, i.e., $\epsilon_1 = \epsilon_3$, $l = d$, and $a = b$. In Figure 7,

k_z/k_o remains virtually unchanged if the ratio b/w is larger than 4.5.

This suggests that the side walls have little or no effect on the

propagation characteristics of the fundamental modes if the side-wall

separation is large enough. Also shown is the effect of the total

eigenmodes (equal number of LSM and LSE modes are used) on the convergence
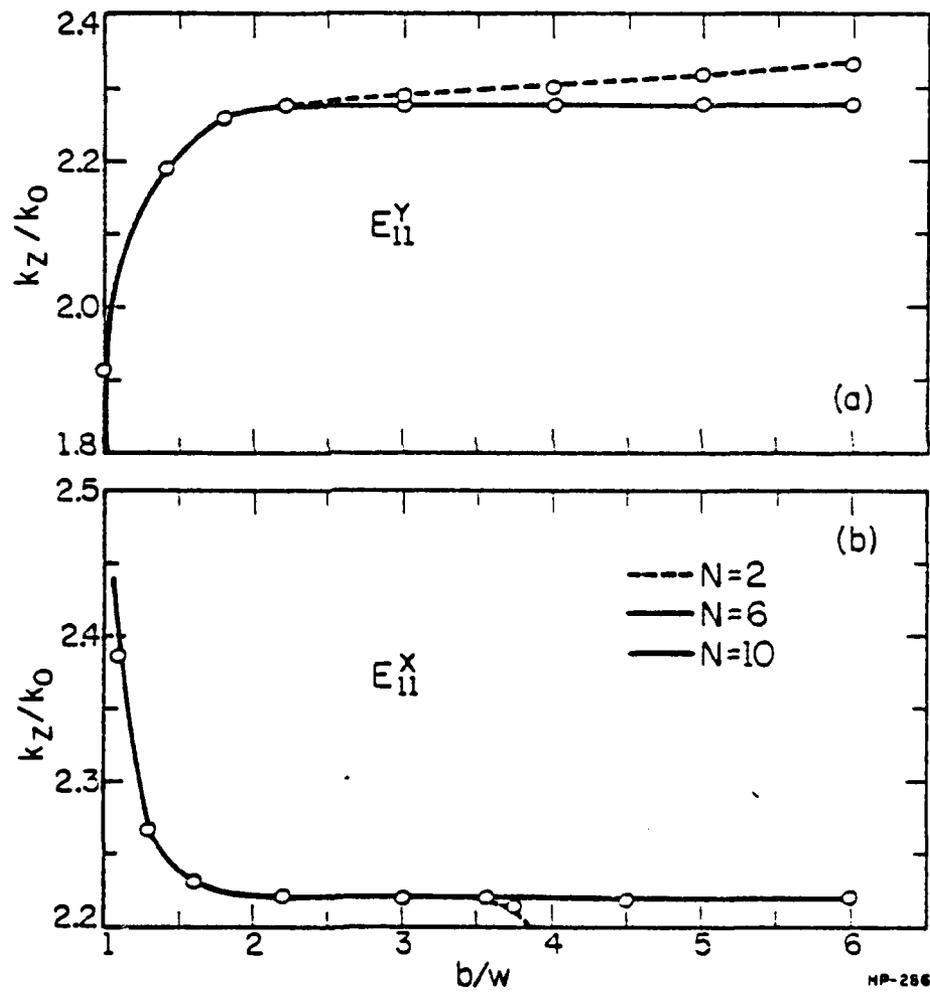
Figure 7. Normalized propagation constants vs. b/w for different numbers of eigenmodes. (a) E_{11}^Y mode. (b) E_{11}^X mode. w/h = 1.14, h/d = 0.55, ε_2 = 9.3, ε_1 = ε_3 = 2.3, d/λ_o = 0.25.

of the propagation constant. For $N = 6$ and $N = 10$, the results are almost indistinguishable. A somewhat similar conclusion was also obtained in investigations of an open dielectric image line by other authors [11],[13].

In Figs. 8 and 9, the phase characteristics are plotted as a function of h/d, which is the ratio of the dielectric core height to the total height of the suspended H-guides for different dielectric constants of the core and the normalized guide height. The values of k_z/k_o computed by the mode-matching technique are shown in solid lines whereas those calculated using the mean value of the effective parameter approximations are shown in dotted lines. Unless otherwise indicated, these line designations are used for the rest of this section. For the fundamental E_{11}^y mode, both techniques agree well except in the range where h/d is small. In most cases, the values of k_z/k_o of the E_{11}^x mode obtained by the effective parameter method are less accurate. For the latter case, it was found that either the effective permittivity or the effective permeability approximation alone usually provides a better result than their mean value. For h/d less than 0.05, the field extends far beyond the dielectric core. To obtain accurate results using the mode-matching approach, the side-wall separation must be large enough, and many more eigenmodes must be used. The computation and the convergence, therefore, are very slow. For this reason, the values of k_z/k_o for small h/d are not presented. In this case, other methods, such as perturbation techniques [20], may be numerically more efficient.
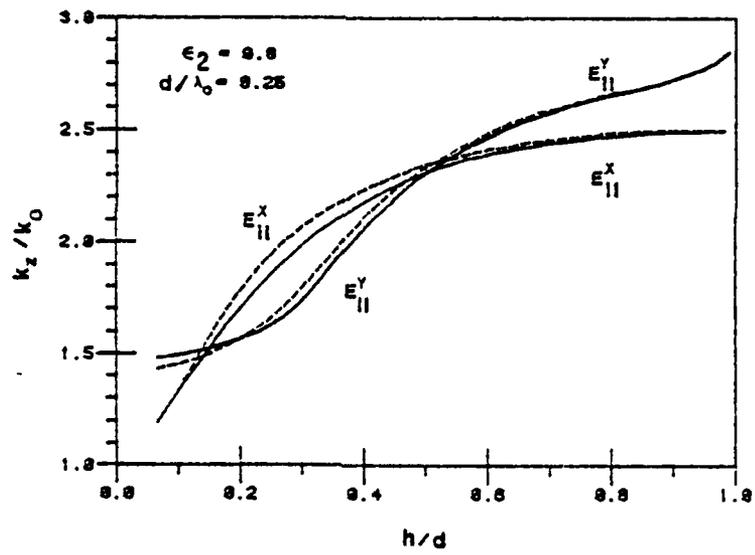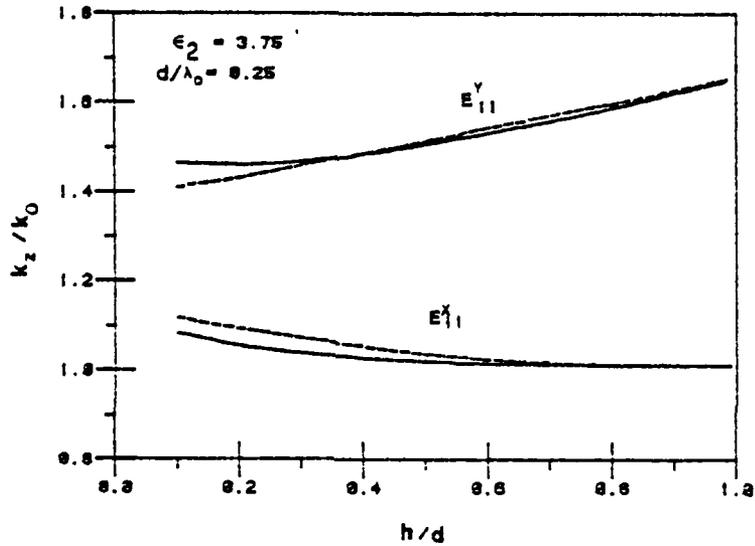
Figure 8. Normalized propagation constants of E_{11}^y and E_{11}^x modes
of a single suspended H-waveguide vs. h/d. $\varepsilon_1 = \varepsilon_3 = 2.3$,
$w/\lambda_o = 0.15$, $l = d$, $a = b$ ($-\infty$). Mode matching: solid
line; effective parameter: dashed line. (a) $\varepsilon_2 = 9.S$
(b) $\varepsilon_2 = 3.75$.
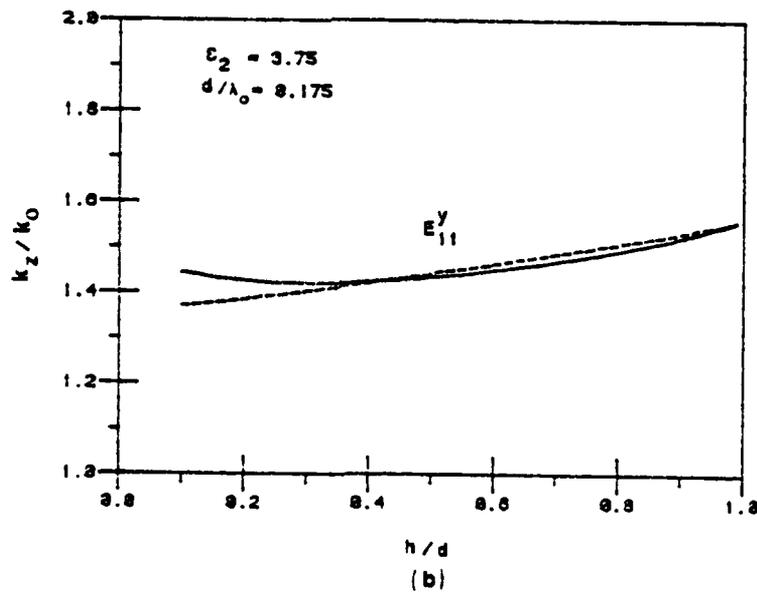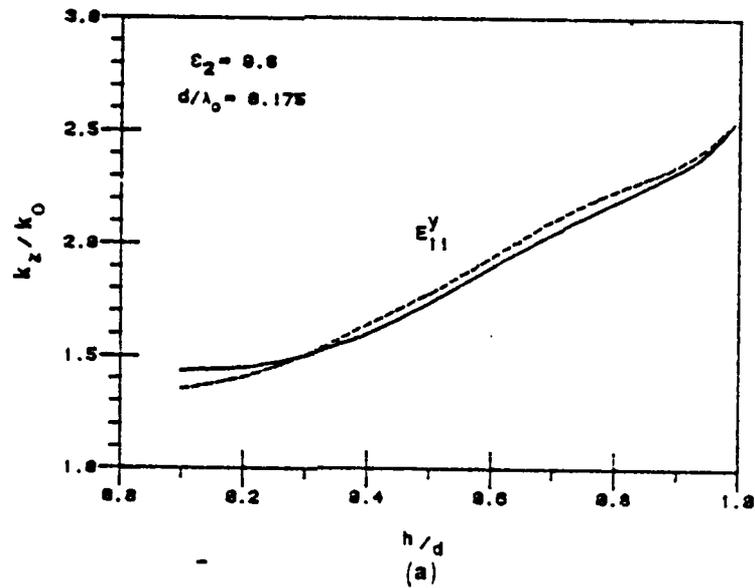
Figure 9. Normalized propagation constants of a single suspended
H-waveguide vs. h/d. $\varepsilon_1 = \varepsilon_3 = 2.3$, $1 = d$, $a = b$ ($-\infty$).

Mode-matching: solid line; effective parameter: dashed
line. (a) $2w/\lambda_o = 0.165$. (b) $2w/\lambda_o = 0.2255$.

The effect of the aspect ratio w/h of the dielectric core on the propagation characteristics of an uncoupled suspended H-waveguide is shown in Figs. 10 and 11 for different values of ε_2 and the normalized guide height. In these figures, the ratio of h/d is arbitrarily chosen to be 0.5. For a higher dielectric constant of the core, a crossover occurs for the propagation constants of the E_{11}^y and E_{11}^x modes. As w/h increases, k_z/k_o derived by the effective parameter approximation approaches the mode matching values. This is expected, since for large values of w/h, the waveguide structure closely resembles a dielectric-slab loaded parallel guide whose LSE and LSM modes do not couple. The complete separation of LSE- and LSM-modes is one of the basic assumptions in deriving the effective parameter technique and, therefore, the results obtained by this technique for large w/h should be closer to the actual values. The reverse is true when w/h becomes smaller. When w/h and ε_2 are small, less energy is concentrated in the dielectric core, and the omission of the "corner" regions in deriving the effective parameter technique is no longer valid. For the E_{11}^y mode, the normalized propagation constants derived by both the effective parameter and the mode matching methods agree well. For the E_{11}^x mode, particularly for the lower dielectric constant case and near cut-off, the effective parameter approximation becomes less reliable.

Figures 12 and 13 are the plots of the normalized propagation constant of a single suspended H-waveguide as a function of the ratio $\varepsilon_2/\varepsilon_1$ for different normalized guide heights. The top and bottom

38
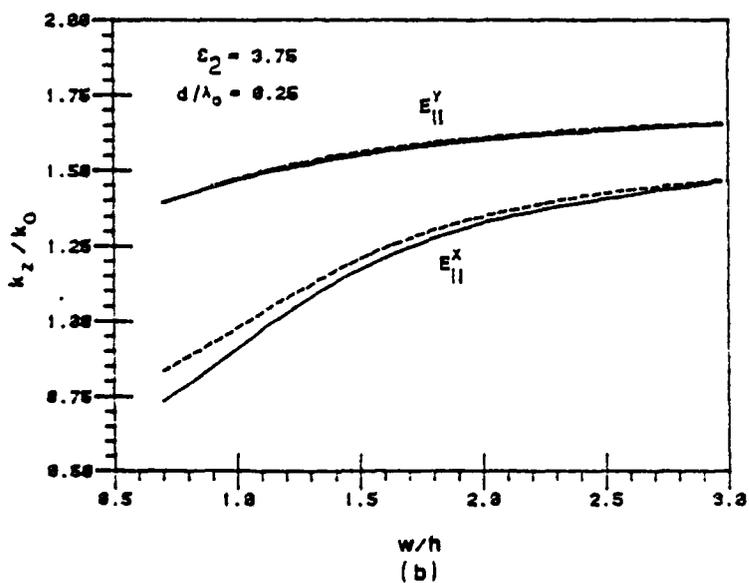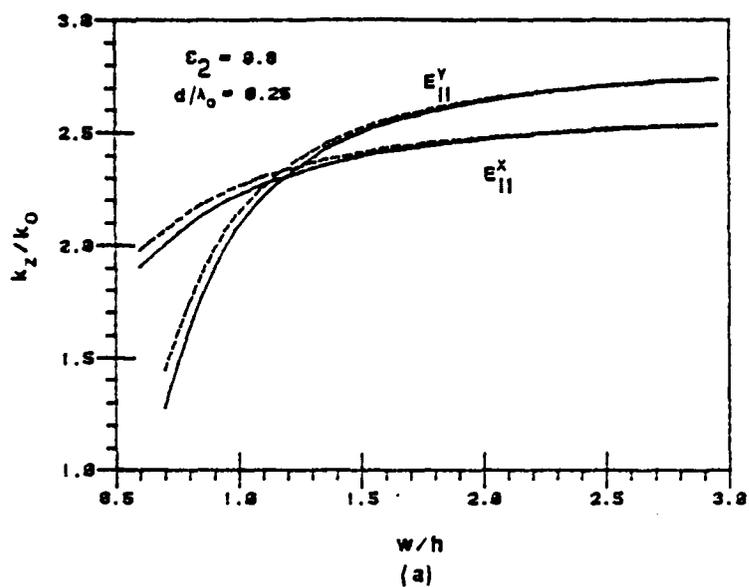
Figure 10. Normalized propagation constants of a single suspended H-waveguide vs. w/h. $\varepsilon_1 = \varepsilon_3 = 2.3$, $l = d$, $a = b$ ($-\infty$).

Mode matching: solid line; effective parameter: dashed-line. (a) $\varepsilon_2 = 9.8$; (b) $\varepsilon_2 = 3.75$.

39

(a)

(b)
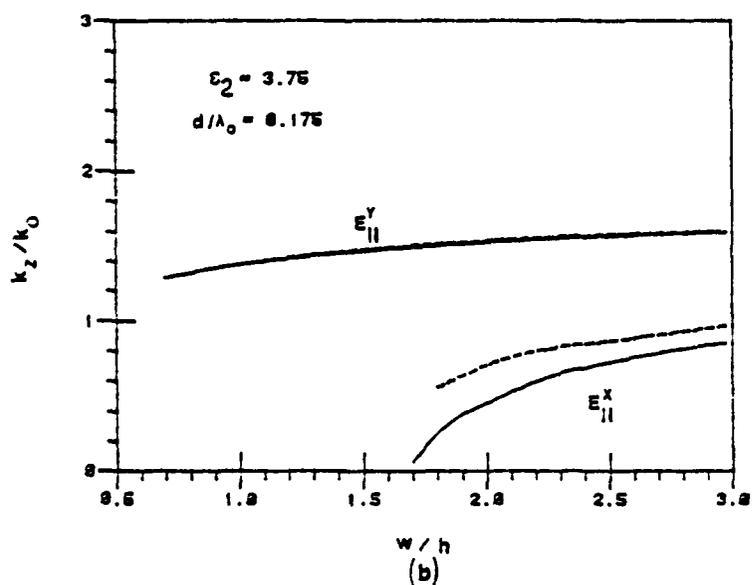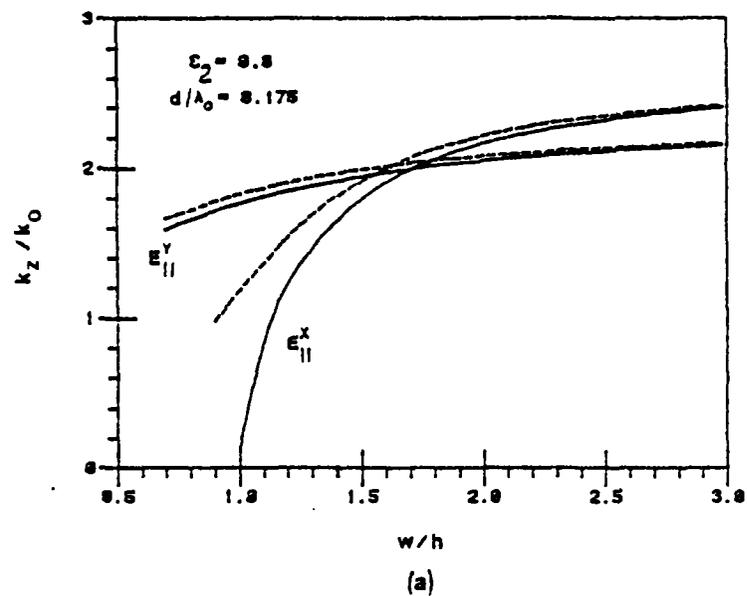
Figure 11. Normalized propagation constants of a single suspended
H-waveguide vs. w/h. $\varepsilon_1 = \varepsilon_3 = 2.3$, $1 = d$, $a = b$ ($\to \infty$).

Mode-matching: solid line; effective parameter:
dashed line. (a) $\varepsilon_2 = 9.8$; (b) $\varepsilon_2 = 3.75$.
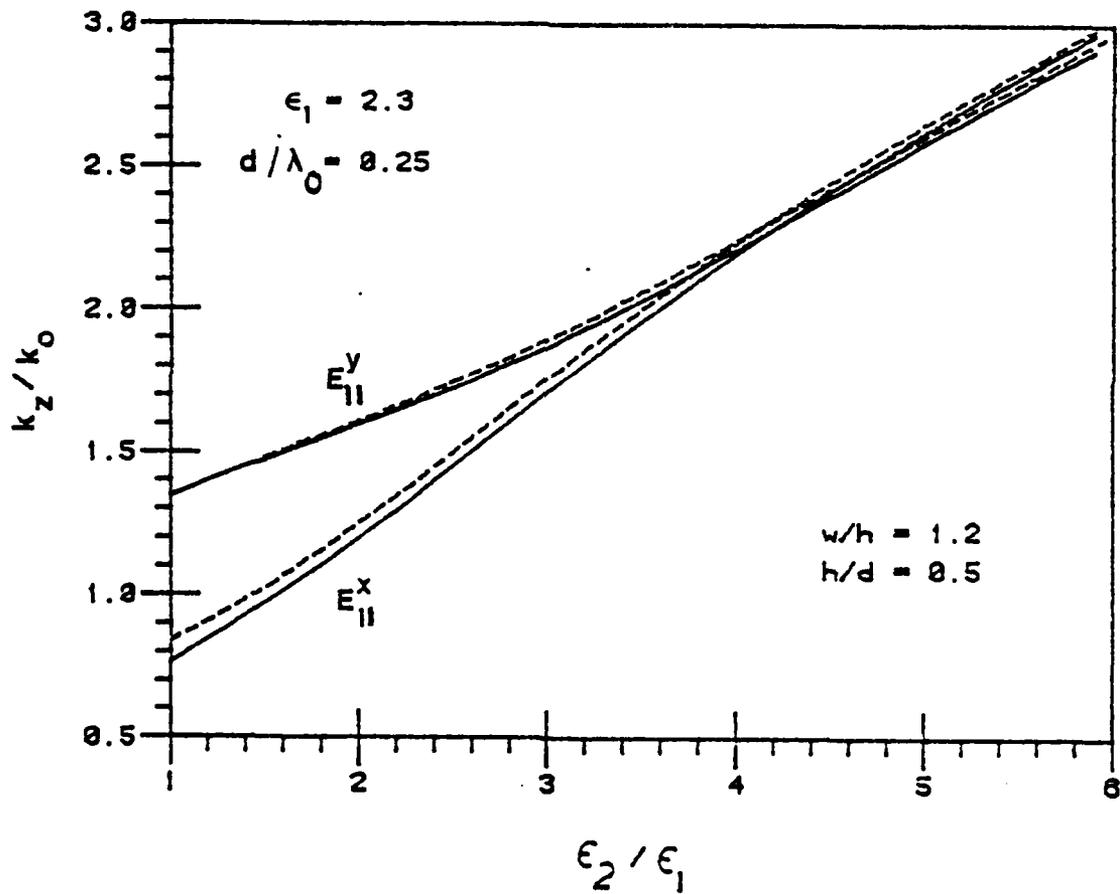
Figure 12. Normalized propagation constants of the fundamental E_{11}^y and E_{11}^x modes of a single suspended H-waveguide vs. $\varepsilon_2/\varepsilon_1 \cdot \varepsilon_1 = \varepsilon_3$, $l = d$, $a = b$ ($-\infty$). Mode-matching: solid line; effective parameter: dashed line.
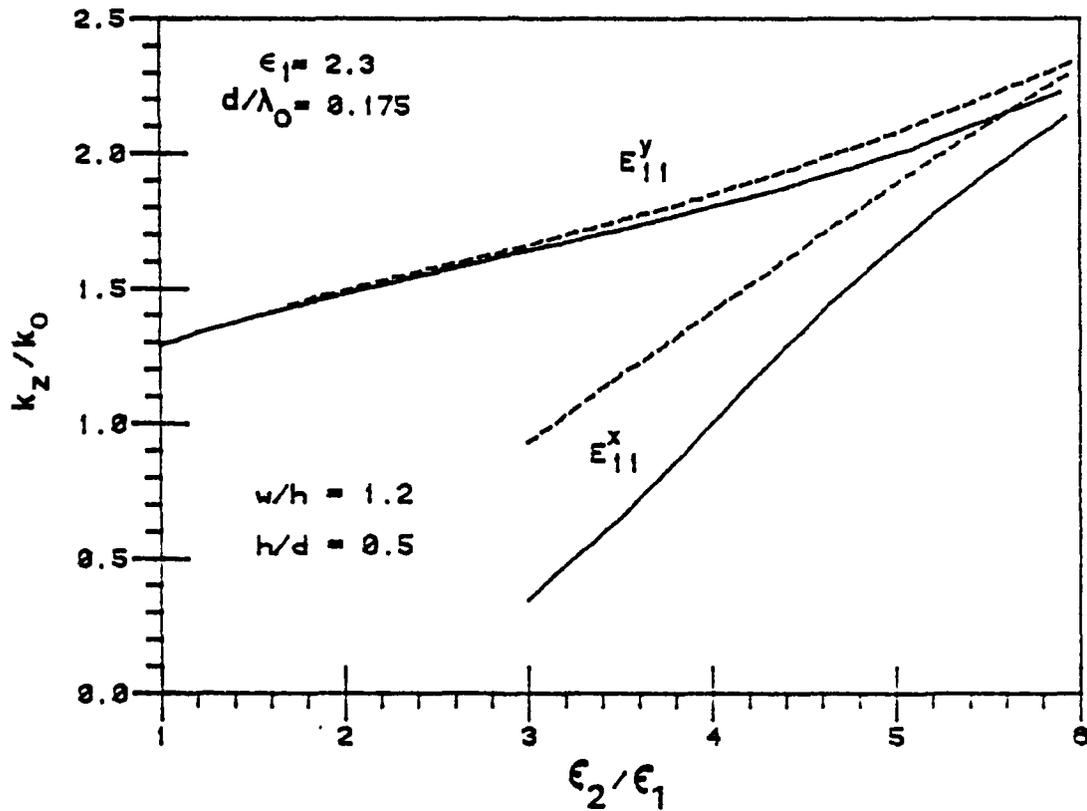
Figure 13. Normalized propagation constants of the fundamental E_{11}^y and E_{11}^x modes of a single suspended H-waveguide vs. $\varepsilon_2/\varepsilon_1 \cdot \varepsilon_1 = \varepsilon_3$, $1 = d$, $a = b$ ($\rightarrow \infty$). Mode matching: solid line; effective parameter: dashed line.

dielectric layers are identical in this case, i.e., $\varepsilon_1 = \varepsilon_3$ and

$1 = d$. The frequency in Figure 12 is approximately 1.4 times higher

than that in Figure 13. For large $\varepsilon_2/\varepsilon_1$, most electromagnetic energy

is tightly bound to the center of the dielectric core. The configura-

tion of the core becomes less important since the field strength at

the dielectric boundaries is small. For this reason, the propagation

constants of the E_{11}^y and E_{11}^x modes converge when ε_2 becomes large, as

shown in Figure 12. In this range, many higher-order modes also exist

in the guide. A somewhat similar behavior of the normalized constant

is obtained by increasing frequency. Figures 14 and 15 show the

dispersion characteristics of the dominant E_{11}^y and E_{11}^x modes as a

function of the normalized free-space wavenumber $k_o d$. In Figure 15,

only the results obtained from the effective permittivity approximation

are presented as the dotted lines since the effective permeability

method inaccurately predicts a high cut-off of the dominant E_{11}^y mode.

Experimental results are also presented in these figures. The agree-

ment between theoretical and experimental results of the E_{11}^y mode is

very good. A combination of a sliding short along the dielectric core

and a reverse coupler at the input of the suspended H-waveguide has

been used to record the standing wave pattern in the guide [21].

Energy was launched from a metal waveguide; the dielectric core is made

of alumina ($\varepsilon_r = 9.8$) and stycast ($\varepsilon_r = 3.75$). The insulating top and

bottom dielectric layers are copper clad RT/Duroid with an $\varepsilon_r = 2.3$.

The tapered transition from the suspended H-waveguide to the metal

waveguide is shown in Figure 16. All measurements were done in the

E-band.
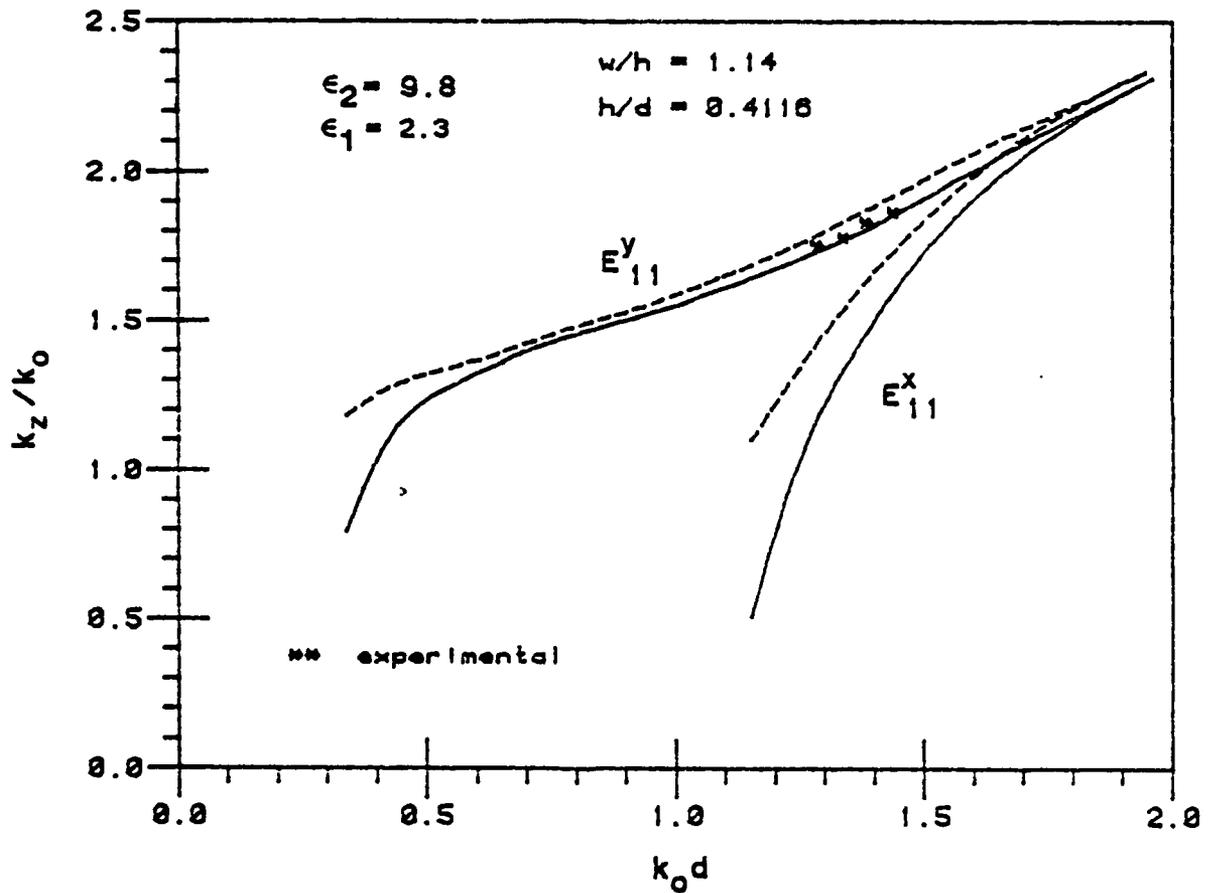
Figure 14. Normalized propagation constants of a single suspended
H-waveguide vs. the normalized free-space wavenumber.
$\epsilon_1 = \epsilon_3$, $1 = d$, $a = b$ ($\rightarrow\infty$). Mode matching: solid line;
effective parameter: dashed line.
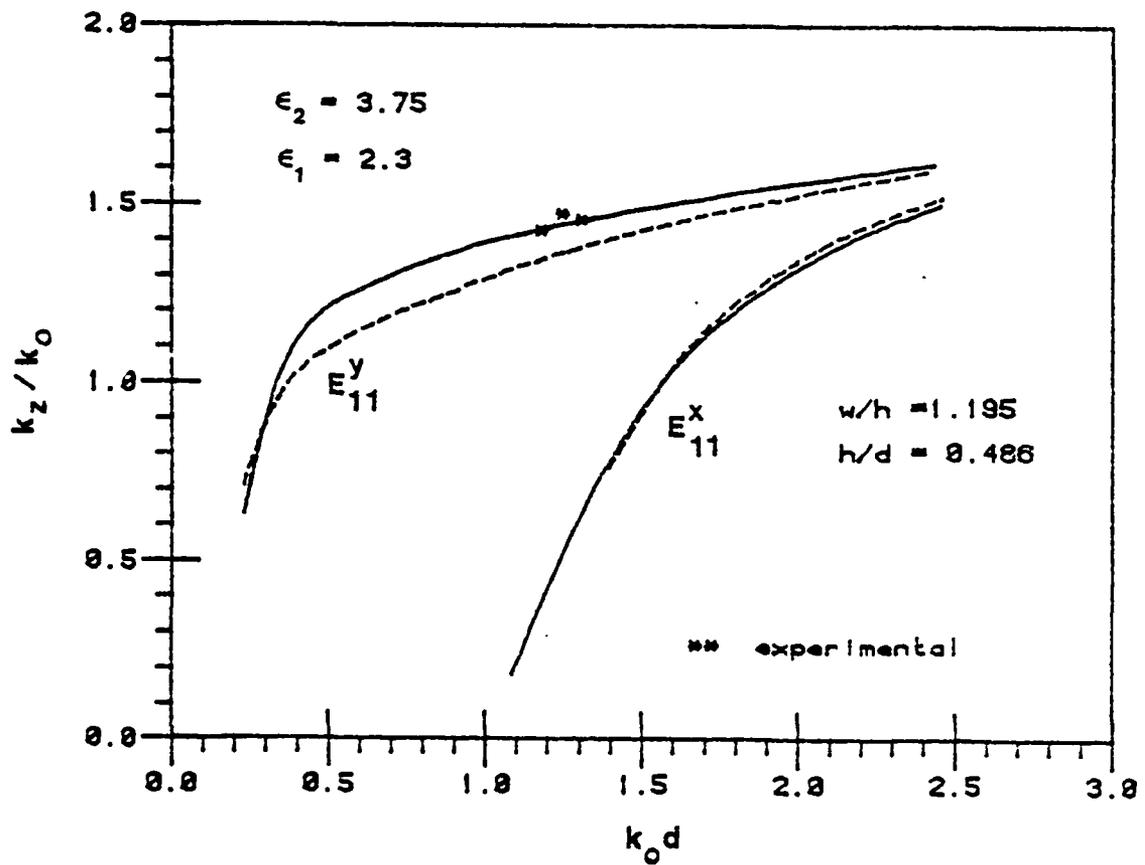
Figure 15. Normalized propagation constants of a single
suspended H-waveguide vs. the normalized free-
space wavenumber. $\varepsilon_1 = \varepsilon_3$, $1 = d$, $a = b$ $(\to\infty)$.

Mode matching: solid line; effective parameter:
dashed line.

Side View

Metal Waveguide

Copper Clad
Insular
Layers

Tapered
Dielectric
Core

Metal
Ground Plane

Top View

Tapered
Dielectric
Guide

Tapered
Insular
Layer

Dielectric
Guide

HP-297
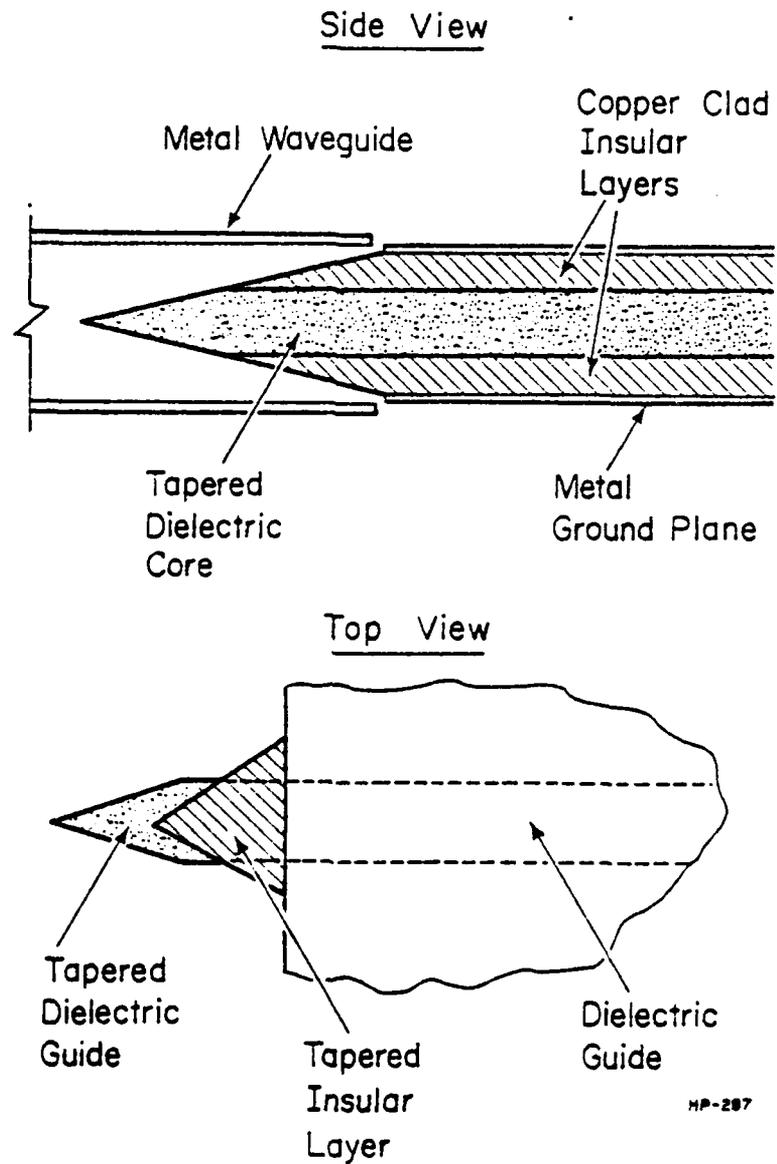
Figure 16. Dielectric tapered transition from the suspended
H-waveguide to the metal waveguide.

Thus far, only a single guide, which is symmetric both in the x- and y-directions, has been studied. Figure 17 shows the normalized propagation constant of the fundamental E_{11}^y and E_{11}^x modes of a single suspended H-waveguide whose top and bottom dielectric layers are not identical. In this case, the thickness of the top layer is varied while that of the lower dielectric layer remains constant. k_x/k_o is plotted as a function of h/d for different dielectric constants ε_1 ($\varepsilon_1 = 2.3$ in Fig. 17a and $\varepsilon_1 = 3.75$ in Fig. 17b). For small values of h/d (large separation), the top metal ground plane has virtually no influence on the propagation characteristics of the guide. In these figures, the effective parameter approximation accurately predicts the behavior of the normalized propagation constants and can always be used to check the existence of a particular mode before using the mode-matching method.

The dispersion characteristics of a couple suspended H-waveguide as a function of the normalized free-space wavenumber k_od are shown in Figs. 18 and 19 for different dielectric constants ε_2 of the core. As frequency increases, the field strength outside each dielectric core becomes smaller, and the propagation constants of even and odd modes approach the value of an uncoupled structure as the influence of one guide on the other becomes negligible. In these figures, subscripts e and o imply a pmc wall and a pec wall at x = -a, respectively. For example, E_{11e}^y represents the even E_{11}^y mode (pmc wall at x = -a) while E_{11o}^y represents the odd E_{11}^y mode (pec wall at x = -a). The same subscript designation applies to the E_{11}^x mode. In Fig. 18, where the
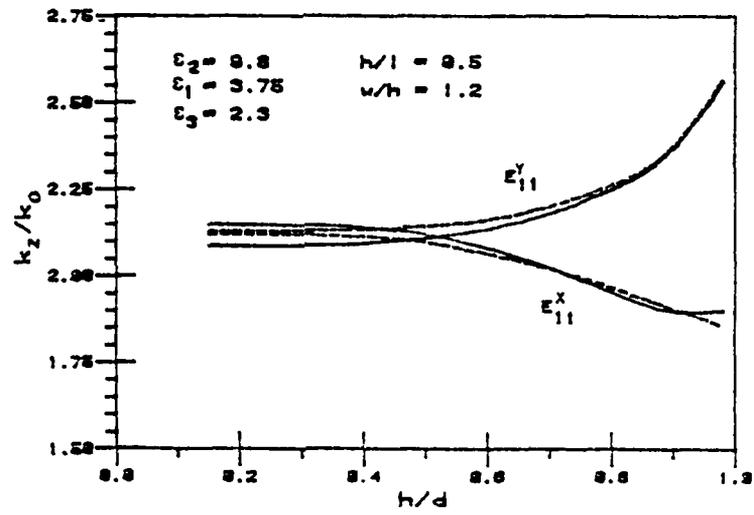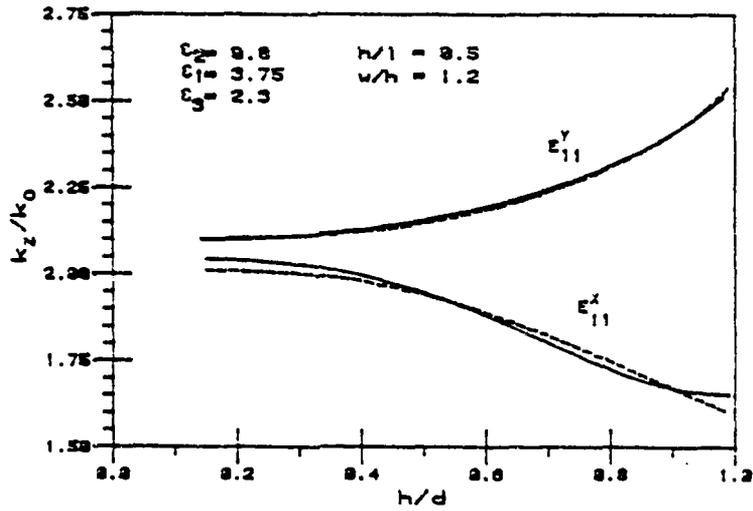
Figure 17. Normalized propagation constants of the fundamental E_{11}^{y} and E_{11}^{x} modes of a single suspended H-waveguide vs. h/d. (a) $1/\lambda_o = 2.166$. (b) $1/\lambda_o = 0.2$ Mode matching: solid line; effective parameter: dashed line.
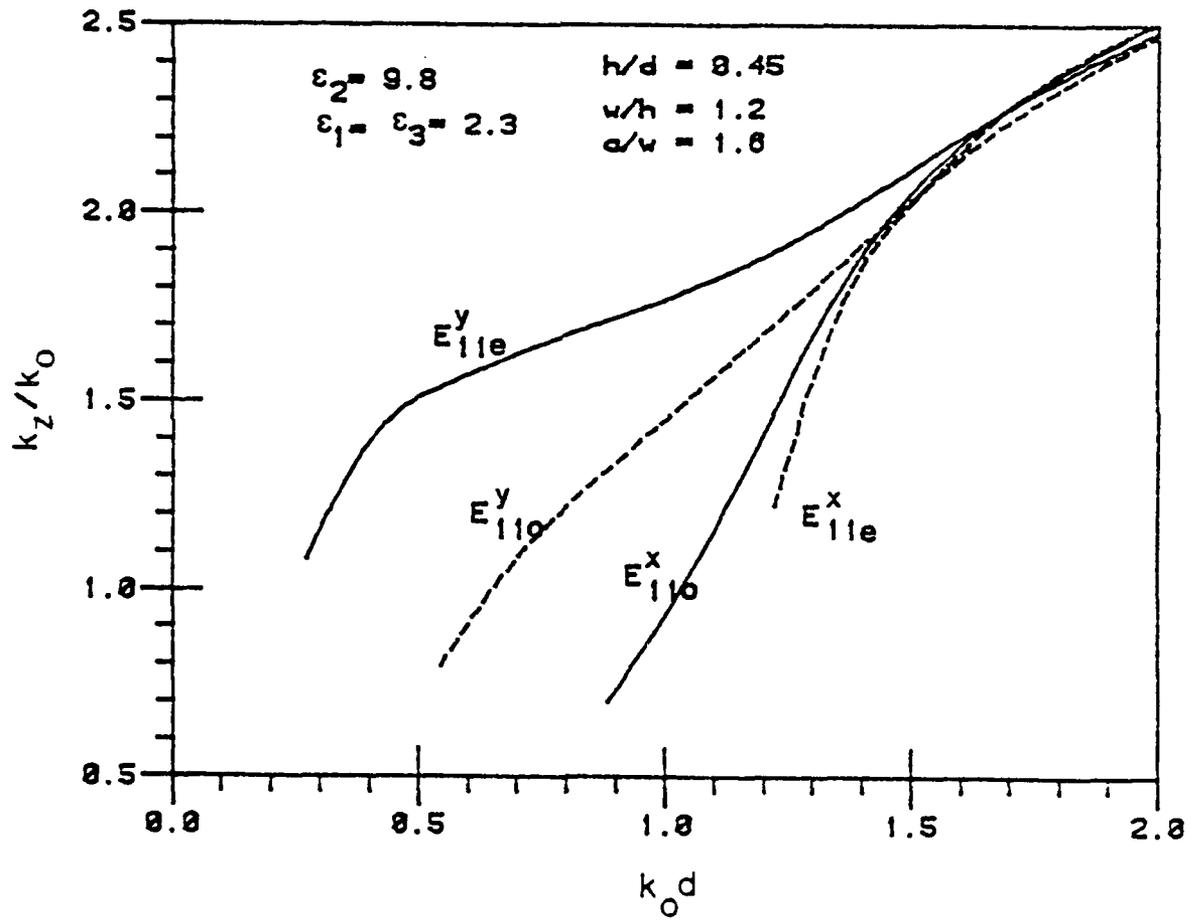
Figure 18. Normalized propagation constants of even and odd E_{11}^{y} and E_{11}^{x} modes of a coupled suspended H-waveguide vs. the normalized free-space wavenumber. $l = d$, $b/w \rightarrow \infty$.
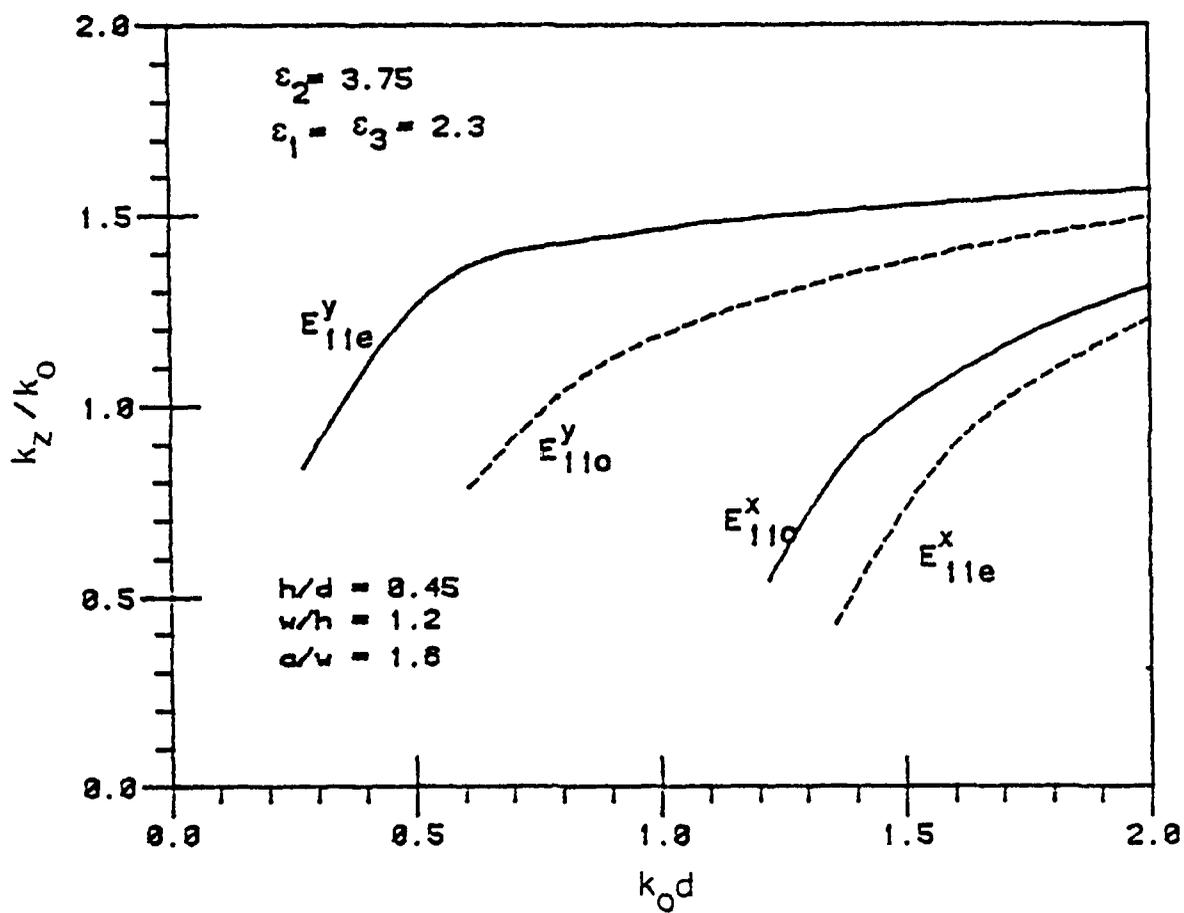
Figure 19. Normalized propagation constants of even and odd E_{11}^{y} and E_{11}^{x} modes of a coupled suspended H-waveguide vs. the normalized free-space wavenumber. $l = d$, $b/w \to \infty$.

dielectric constant of the core is much higher than that in the surrounding medium, the normalized propagation constants of even and odd modes of both E_{11}^{y} and E_{11}^{x} modes converge rapidly as frequency increases. For a lower dielectric constant of the core (see Fig. 19), the fields are weakly bound and, therefore, all modes converge at much higher frequencies. k_{z}/k_{o} obtained by the effective parameter approximation always approaches the mode matching's values at higher frequencies. However, in the normalized frequency range investigated here, the difference between the two techniques is substantial. Hence, for clarity, only the dispersion characteristics derived by the mode matching method are presented.

3.2 Normalized Propagation Constant of Other Dielectric Waveguide Structures

It was mentioned previously that the method of analysis for the suspended H-waveguide could also be used for other planar dielectric structures of rectangular cross-section. Information in Figs. 7 and 15 shows that the analysis of a totally shielded structure can be used for an open dielectric structure if the wall separation is large enough. Therefore, by using all or part of Eq. (21), the propagation character-istics of many open dielectric waveguide structures can be obtained. The dispersion curves of some lowest-order modes of an image guide (see Figure 3b) are shown in Figure 20. The range of k_{z}/k_{o} is between 1 and $\sqrt{\varepsilon_{r}}$ since, for an open structure, the propagation constant of any surface wave mode must be greater than the free-space wavenumber and less than the intrinsic phase constant of the dielectric. The
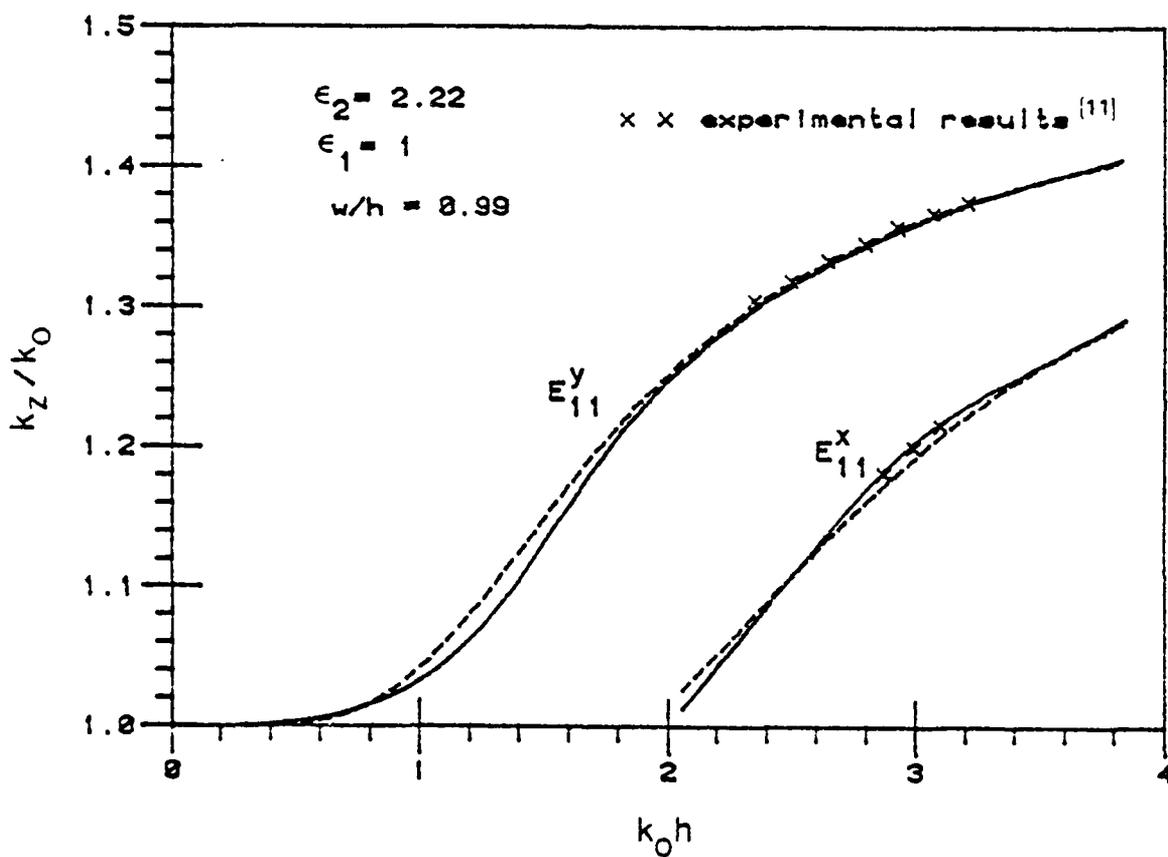
Figure 20. Normalized propagation constants of the fundamental E_{11}^y and E_{11}^x modes of an image guide vs. the normalized free-space wavenumber. $b/w \rightarrow \infty$, $d/h \rightarrow \infty$. Mode matching: solid line; effective parameter: dashed line.

theoretical results of both mode matching and of the effective parameter approximation are compared with the experimental results which were published by Solbach et al. [11]. The agreement between theoretical and experimental results is excellent throughout. The propagation constant of the image line derived from the mode-matching method is obtained by recording the zeros of the determinant of (22). The field mode descriptions of an image-guide are the same as those in a suspended H-waveguide. The image-guide has found many applications in millimeter-wave integrated circuits, such as resonators [22], leaky-wave antennas [23], isolators [24], and phase shifter [25].

The partially loaded trough guides (see Fig. 3d) find applications in dielectric leaky-wave antennas [26], and, in many cases, can be used to reduce the radiation loss at a bend in an image-guide transmission line [6],[27]. If the dielectric constant of the dielectric is high enough, backward propagating waves may exist in the structure which can be used for reverse coupling applications. Since this waveguide structure has been extensively studied elsewhere [10], only a typical dispersion curve is presented here (see Fig. 21). The dispersion characteristics of the E_{11}^{x} mode in the lower frequency range of this guide are similar to the characteristics of empty parallel metal plates whereas the E_{11}^{y} mode has a high cut-off. The dotted lines represent effective dielectric constant curves and the solid lines are the mode-matching values.

Another important waveguide structure is the rib dielectric wave-guide. This waveguide is very similar to an insular guide (see Fig. 3c)
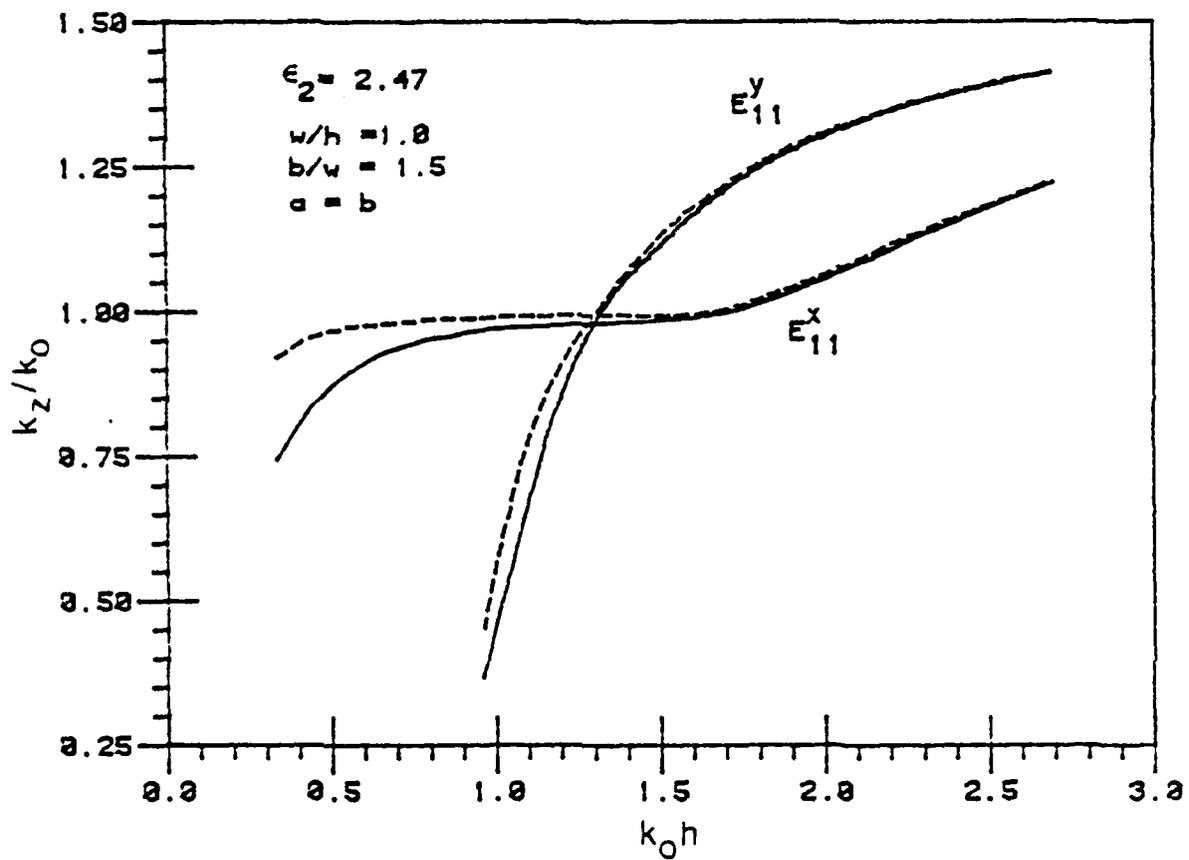
Figure 21. Dispersion curves of the fundamental E_{11}^{y} and E_{11}^{x} modes of a partially loaded trough waveguide. $d/h \rightarrow \infty$. Mode-matching: solid line; effective parameter: dashed line.

except that the dielectric guiding layer and the substrate are made from the same material. Most of the energy concentrates in the dielectric substrate layer. The strip merely acts as a guide to control the lateral expansion of the field. To analyze this structure using the same equations derived for the suspended H-waveguide, the top layer of the suspended H-waveguide is replaced by free space. The top metal ground plane and the side walls must be placed far from the dielectric core so that they have a negligible influence on the propagation of the field modes in the dielectric core region. The effect of the side-wall location on the propagation characteristics has been demon-strated in Figs. 7 and 17. The dispersion characteristics of a single dielectric strip are shown in Fig. 22. Again, only the effective permittivity values are presented since the effective permeability wrongly exhibits a very high cut-off for the fundamental mode. Even the effective permittivity is not accurate in this case as the curves of the E_{11}^y mode in Fig. 22 show a substantial difference between the effective permittivity and the mode matching techniques. In deriving the effective parameter approximation, we have assumed that most energy is concentrated in the dielectric core. The "corner" regions in the substrate could, therefore, be ignored. This assumption is not valid in a rib dielectric waveguide since most of the energy is actually confined to the substrate region. Consequently, the values of k_z/k_o derived by the effective parameter approximation do not represent the true dispersion characteristics of the field modes in a rib dielectric waveguide. If the dielectric constant of the core becomes higher,
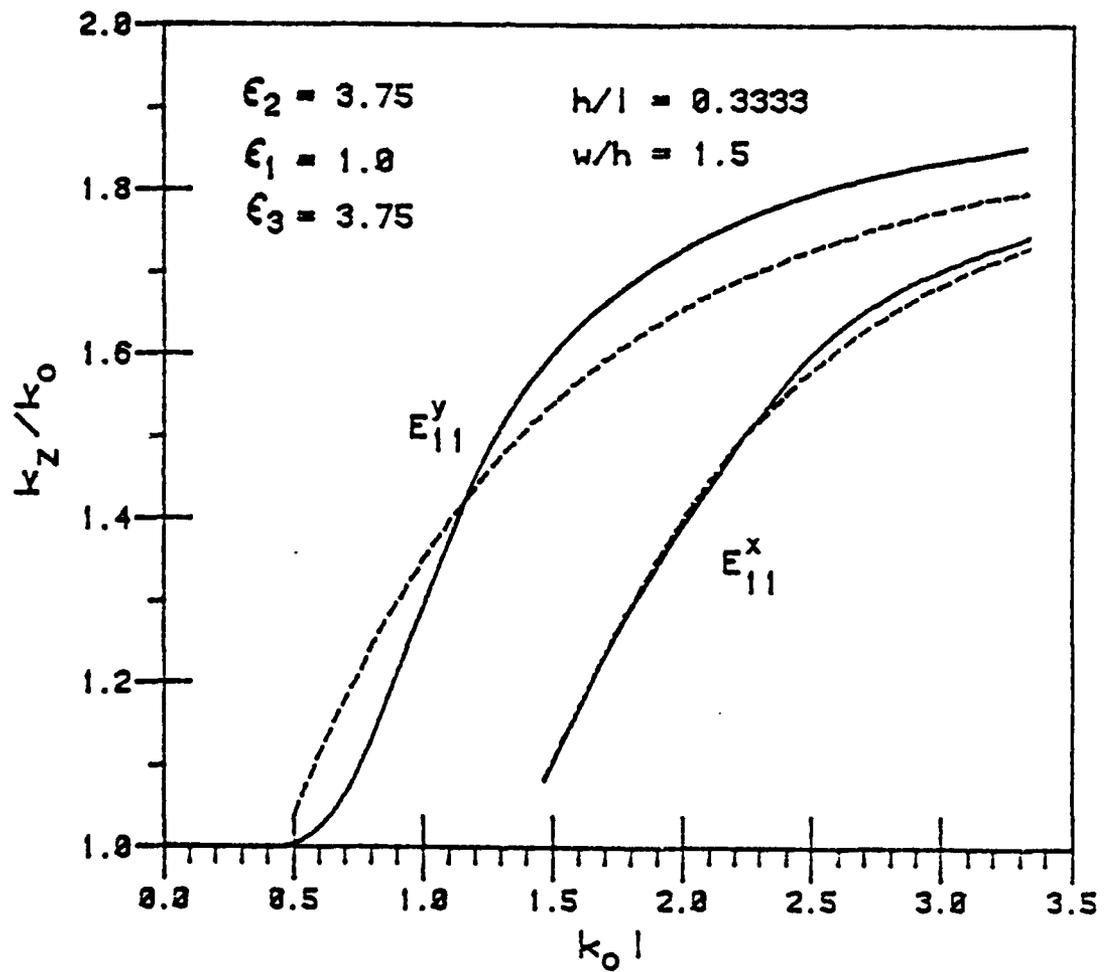
Figure 22. Dispersion curves of the fundamental E_{11}^{y} and E_{11}^{x} modes of a rib dielectric waveguide. Mode-matching: solid line; effective parameter: dashed line.

as in an insular guide, the effective parameter approximation values will approach the mode matching values as indicated in Figure 17.

3.3 Field Distribution of a Suspended H-Waveguide and Other Dielectric Structures of Rectangular Cross-Section

It is well-known that the effective parameter approximation is adequate for calculations of the propagation constant. It does not, however, provide accurate information on the field distribution of the waveguide structure since the fields in certain regions are totally ignored. The mode matching technique can theoretically provide exact field distributions in the dielectric waveguide if an infinite number of eigenmodes are taken into account. Due to the limitation of computation facilities, an infinite number of these eigenmodes (or terms) must be approximated by a finite series. Hence, the numerical accuracy can be limited by computer storage and computation time. In general, when the waveguide is operated near cut-off, the fields extend far away from the dielectric core. To accurately represent a true open dielectric guide, such as an image-guide or an insular guide, or a partially open structure such as the suspended H-waveguide when using the mode-matching technique, the theoretical metal enclosure must be enlarged to minimize its effect on the propagation and field characteristics of the guide. Consequently, a greater number of eigenmodes must be used to maintain the same degree of accuracy. More terms are necessary since a larger number of slowly varying eigenfunctions in the outer regions are required to satisfy the boundary conditions

across the dielectric interfaces with the rapidly varying fields in
the core region. On the other hand, when the dielectric waveguide
core has a higher dielectric constant or when the guide is operated far
beyond cut-off, the fields decay quickly away from the dielectric
core, necessitating smaller wall separation when applying the mode-
matching technique. In this case, fewer eigenmodes are necessary.
The effect of the total number of eigenmodes on the field character-
istics of a totally open or partially open dielectric waveguide will
be discussed in this section. Unless otherwise indicated, equal
numbers of the LSM and the LSE eigenmodes are used. Since the field
distribution of H_x is very similar to E_y and since E_x is similar to
H_y, only H_x and E_x are presented as the transverse fields. The plots
of H_x, E_x, H_z and E_z of the E_{11}^y mode versus y/h in a single suspended
H-waveguide for different x-locations in the guide are shown in
Figures 23 to 26. For these figures, the modal expansion for the fields
consists of ten modes. The top and the bottom dielectric layers are
identical, i.e., $1 = d$ and $\varepsilon_1 = \varepsilon_3$. All the electric field components
in the guide are normalized to the amplitude of the dominant electric
field and all the magnetic field components to the amplitude of the
dominant magnetic field. By comparing the amplitude of each field
component at different y-locations, one can visualize the lateral
distribution of that particular field. For an E_{11}^y mode, the $x = 0$
plane is equivalent to a pmc wall; therefore, H_z and E_x are equal
to zero at this plane. Far away from the dielectric core, e.g., at
$x = 2w$, more energy is concentrated in the top and the bottom
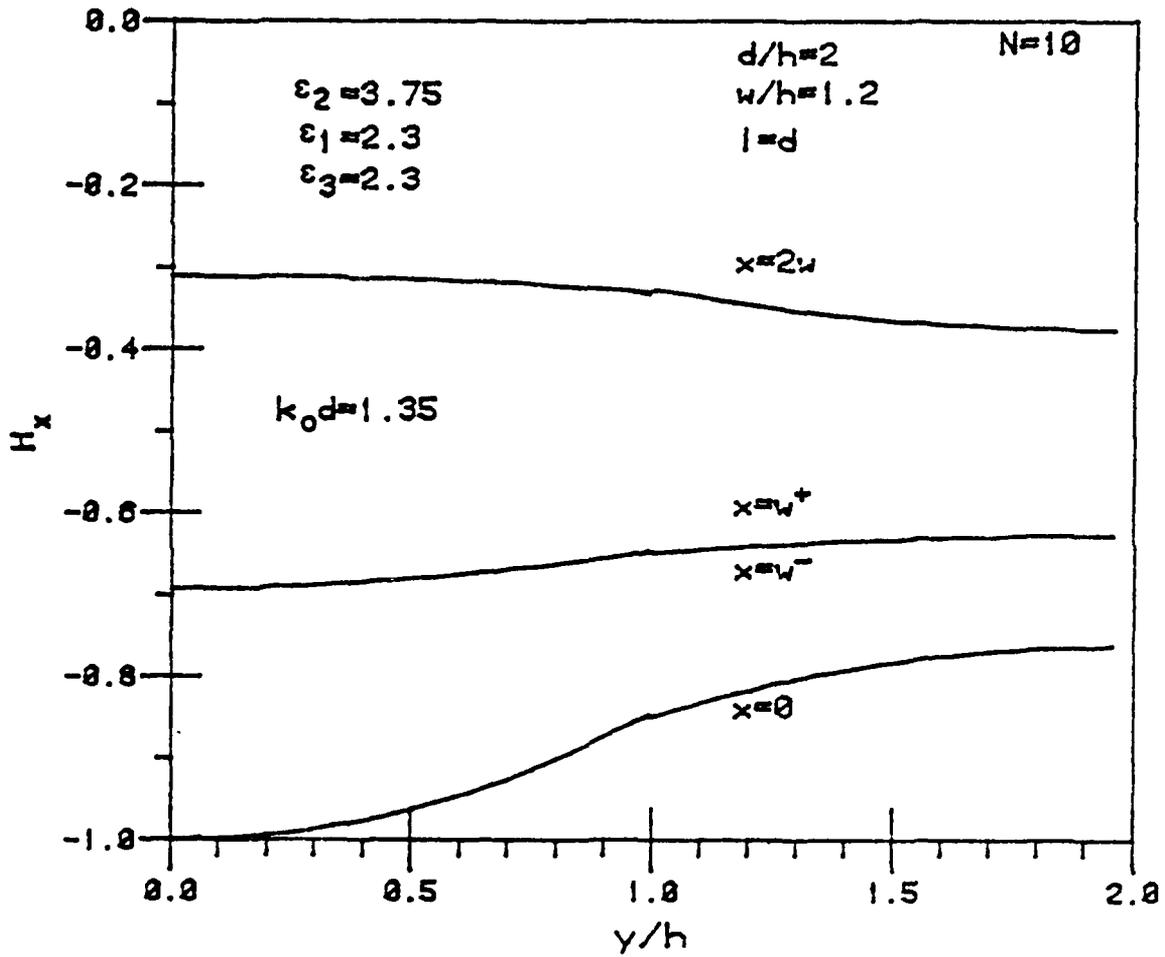
Figure 23. Normalized calculated field distribution of H_x of the E_{11}^y mode at different x-locations in a single suspended H-waveguide.

59
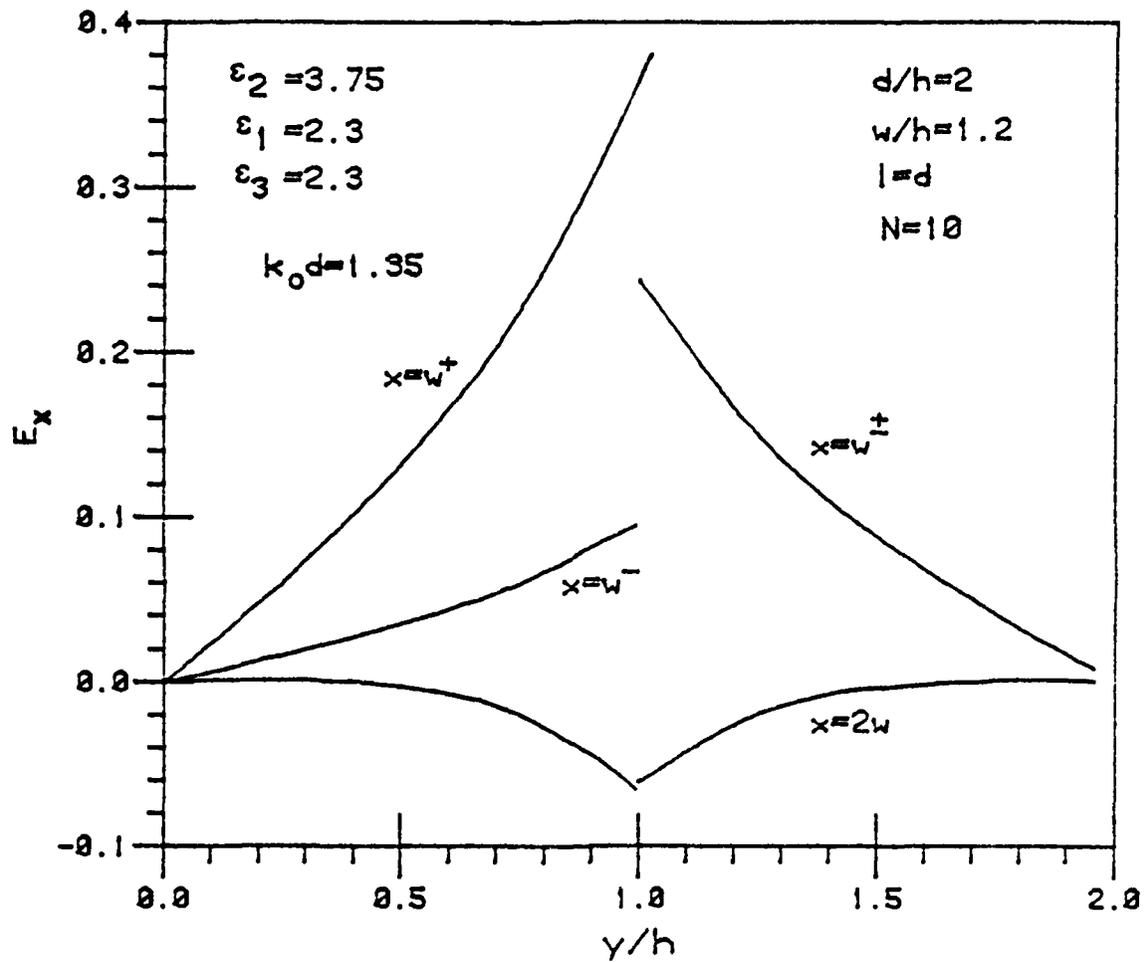
Figure 24. Normalized calculated field distribution of E_x of the E_{11}^y mode at different x-locations in a single suspended H-waveguide.

60
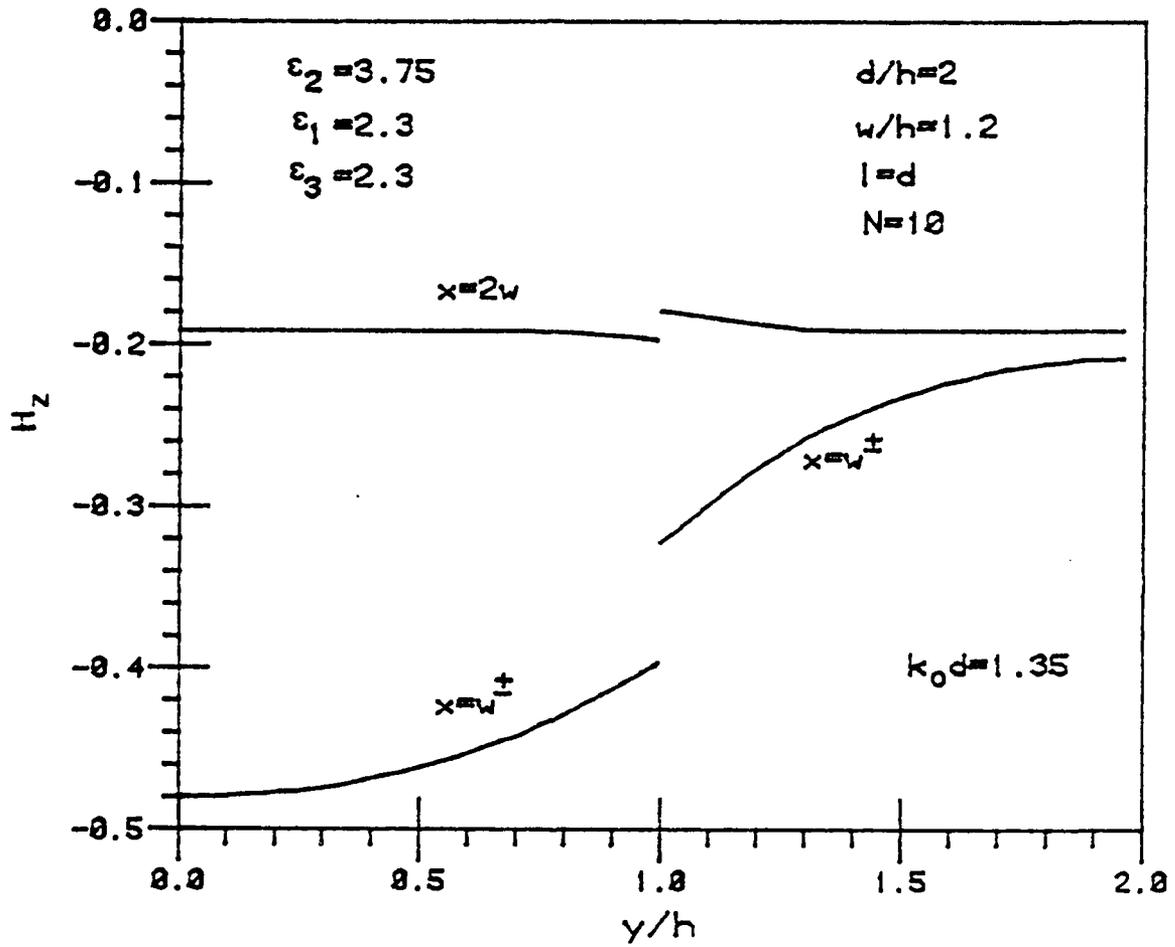
Figure 25. Normalized field distribution of H_z of the E_{11}^y mode at different x-locations in a single suspended H-waveguide.
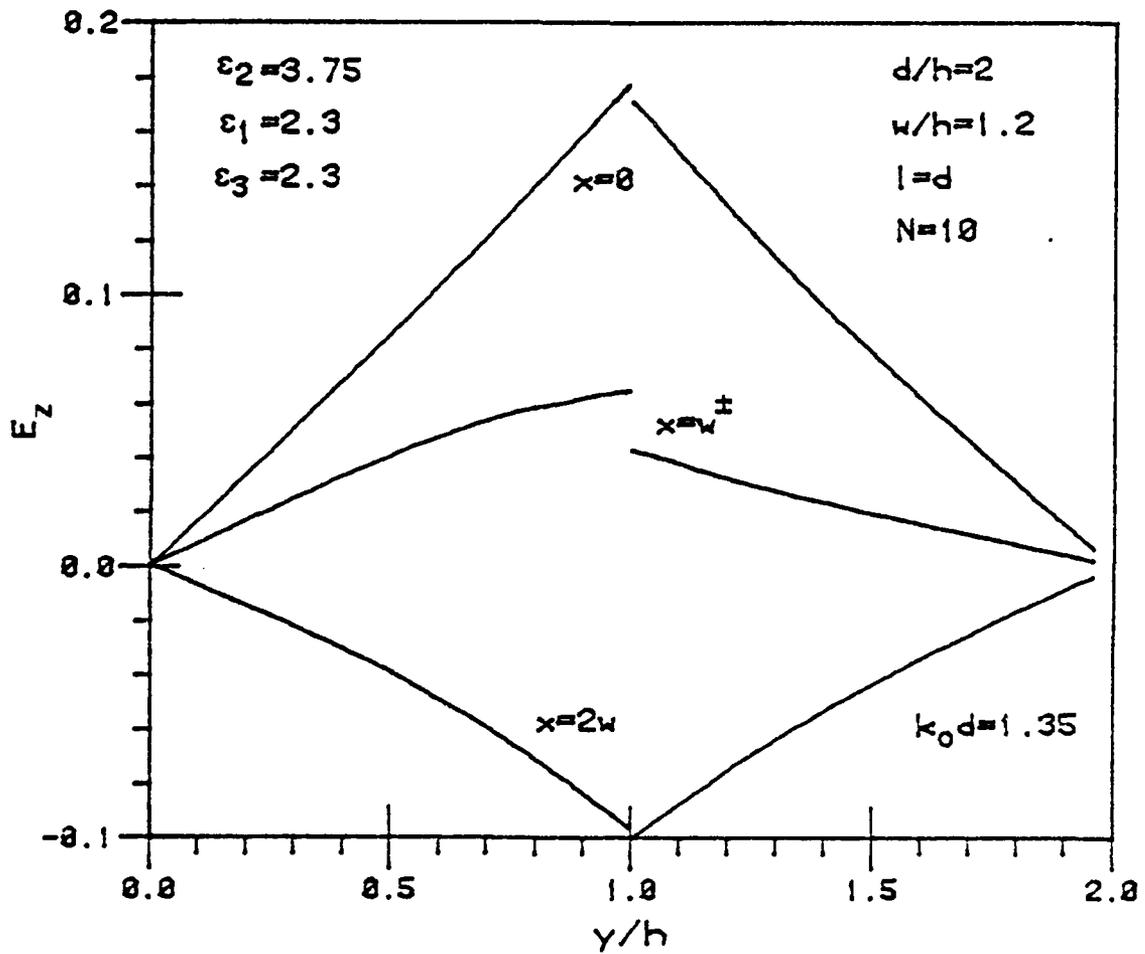
Figure 26. Normalized field distribution of E_z of the E_{11}^y mode at different x-locations in a single suspended H-waveguide.

dielectric insultating layers as indicated by an increasing amplitude of H_x for $y \geq h$ as indicated in Figure 23.

Inspection of Figures 23 to 26 indicates that with ten eigenmodes, the matching of the field components at the $x = \pm w$ interfaces is excellent except for the normal electric field component. (For a complete description of the waveguide parameters, see Figure 2.) Matching across the $y = \pm h$ interfaces is more difficult since E_x is a continuous function of x at $y = h^+$, but a discontinuous function of x at $y = h^-$. The matching of the dominant field component H_x, however, is excellent throughout.

The lateral field distributions at different y-locations and the tests of their convergences for different numbers of eigenmodes are shown in Figures 27 and 28. The general shapes of the distributions in the insulating layers, e.g., $y = 1.4 \, h$, and in the dielectric core region, e.g., $y = 0.5 \, h$, are very similar. This is a clear justification for the effective parameter technique in assuming the dielectric core as an infinite slab in deriving the transverse characteristic equation of k_x. The plots of the fields for $N = 7$ and $N = 12$ are almost indistinguishable. Except at $y = \pm h$, the matching of the H_z component at other locations is very good.

Figures 29 to 32 are plots of H_x, H_z, E_x and E_z at the $x = 0.5w$ plane in a single suspended H-waveguide whose top and bottom dielectric layers are not identical. The top layer has a dielectric constant $\varepsilon_1 = 3.75$ while the lower layer has $\varepsilon_3 = 2.3$ The field components in this structure are no longer symmetric in the y-direction. Since

63
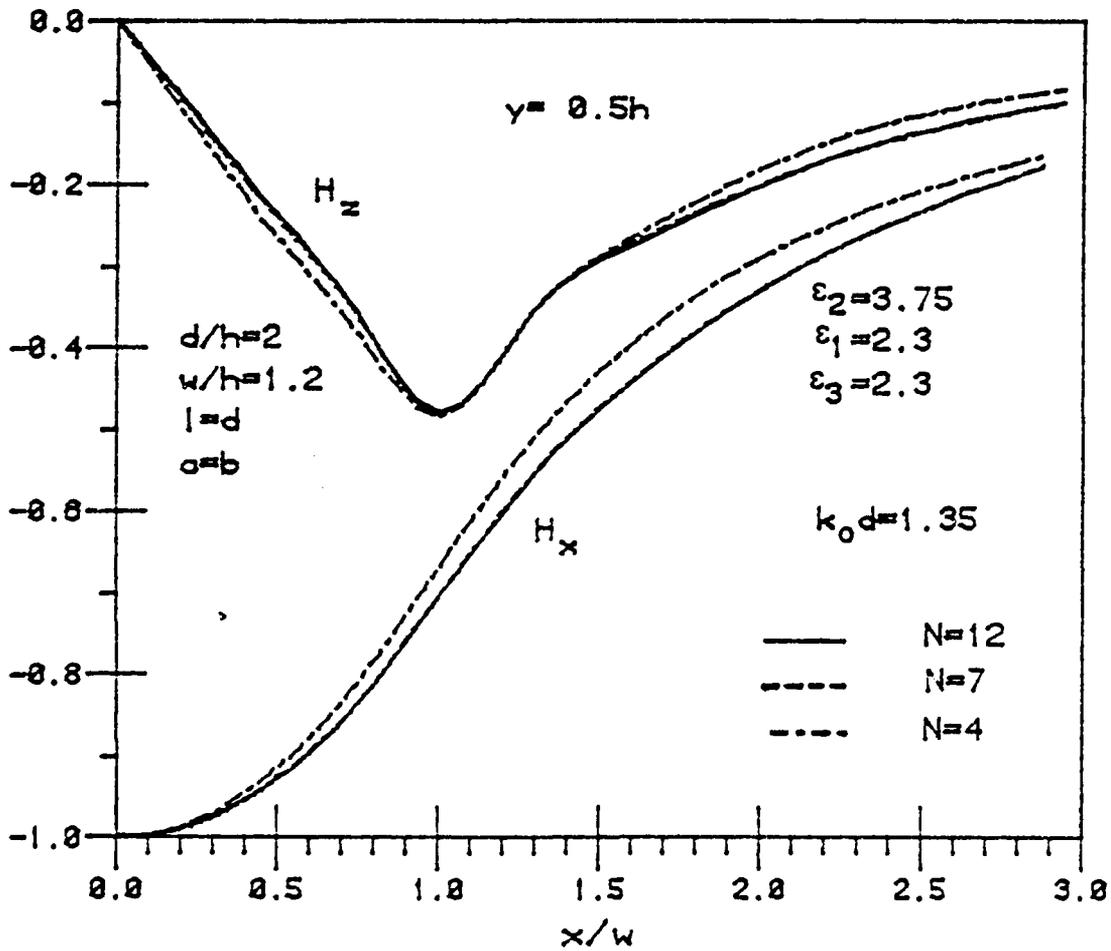
Figure 27. Normalized magnetic field distributions of the E^y_{11}
mode in the transverse direction at $y = 0.5\,h$ in
a single suspended H-waveguide.

64

Figure 28. Normalized magnetic field distributions of the E_{11}^y mode in the transverse direction at y = 0.5 h in a single suspended H-waveguide.
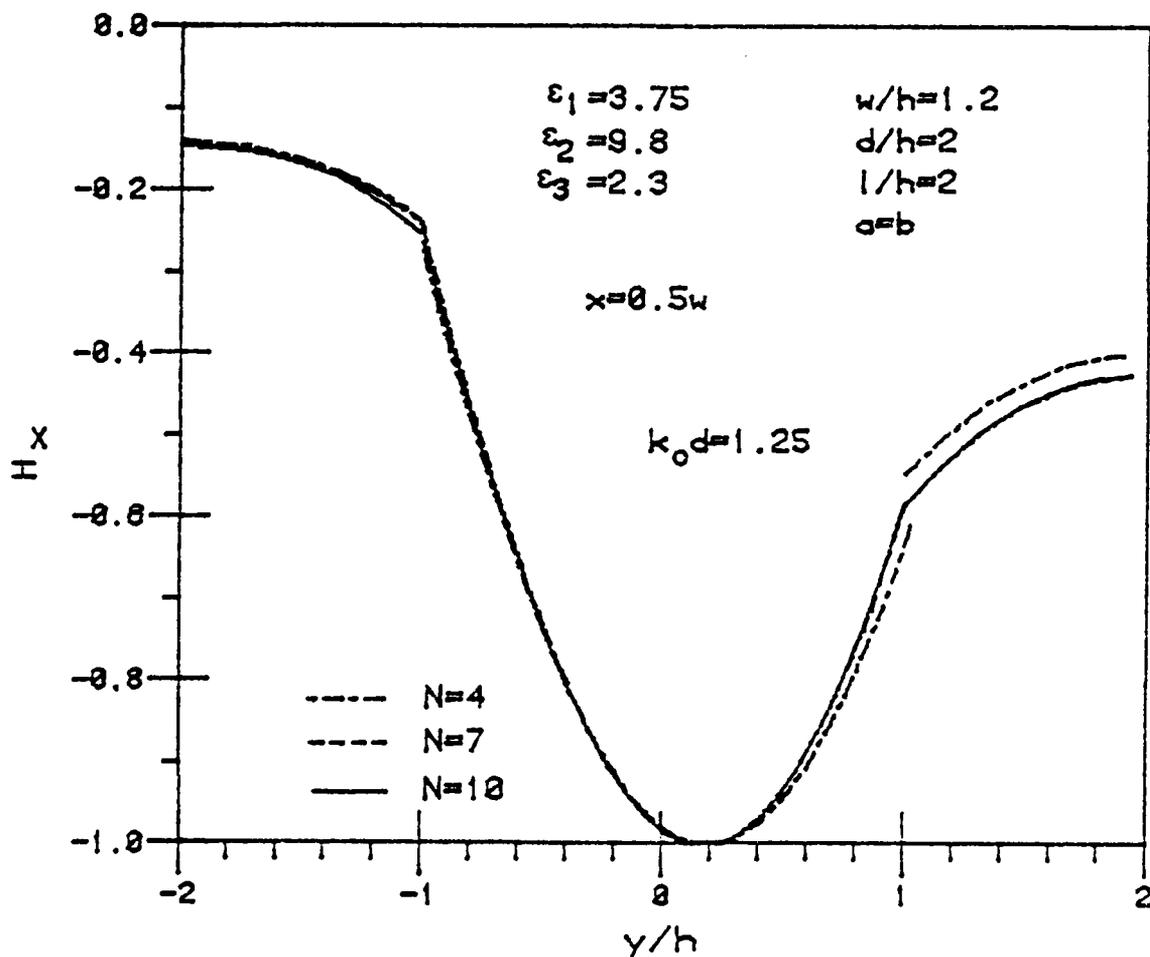
Figure 29. Normalized field distribution of H_x of the E_{11}^y mode in the vertical direction at x = 0.5w in a single suspended H-waveguide whose top and bottom dielectric layers are dissimilar.

66
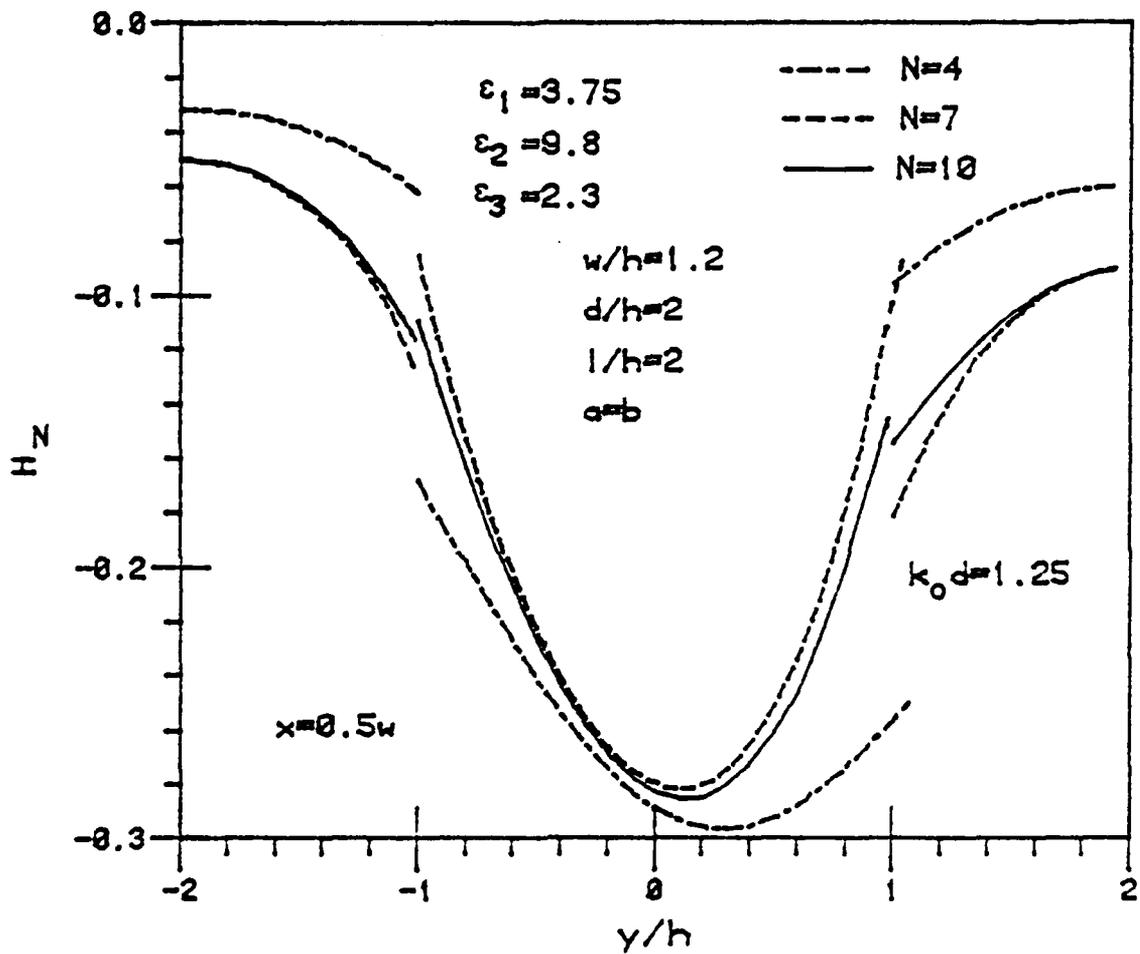
Figure 30. Normalized field distribution of H_z of the E_{11}^y mode in the vertical direction at $x = 0.5w$ in a single suspended H-waveguide whose top and bottom dielectric layers are dissimilar.
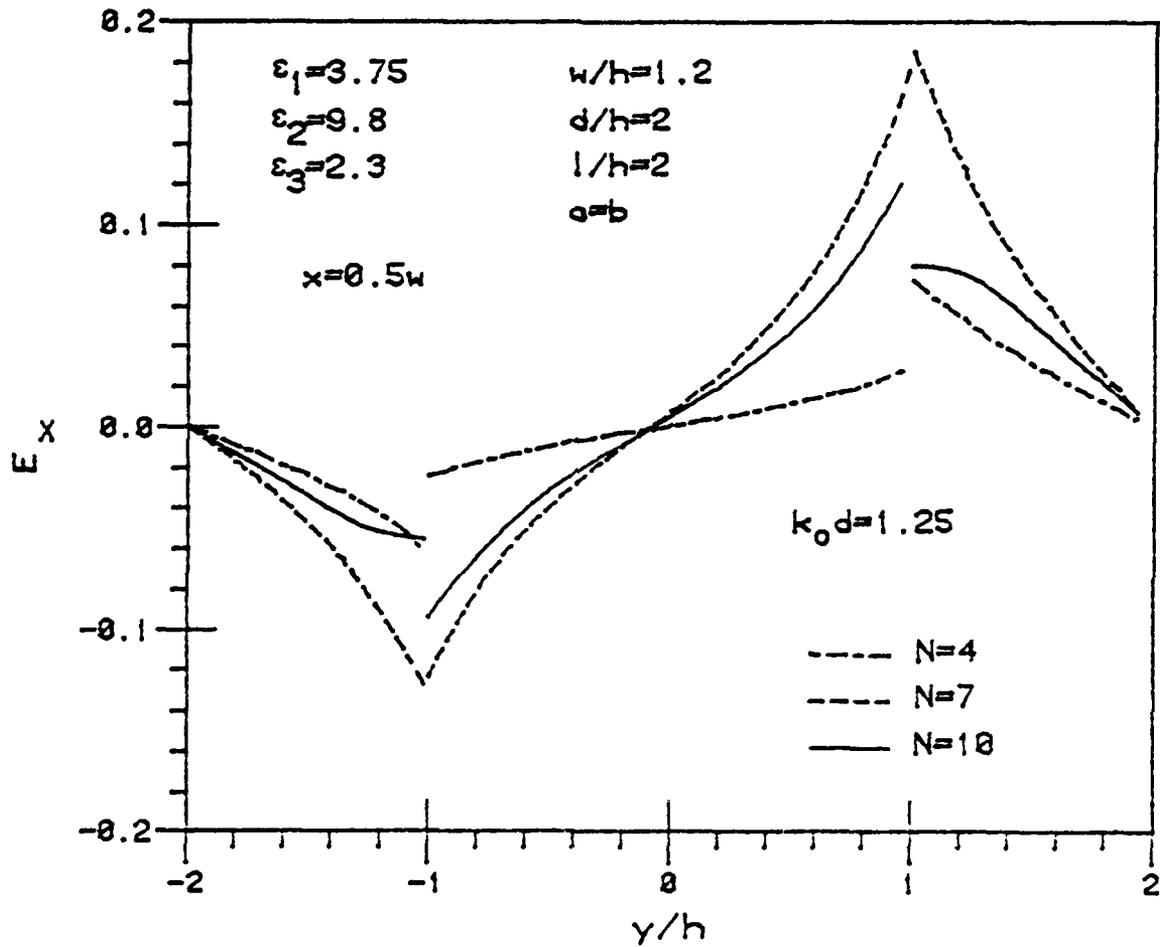
Figure 31. Normalized field distribution of E_x of the E_{11}^y mode in the vertical direction at $x = 0.5w$ in a single suspended H-waveguide whose top and bottom dielectric layers are dissimilar.
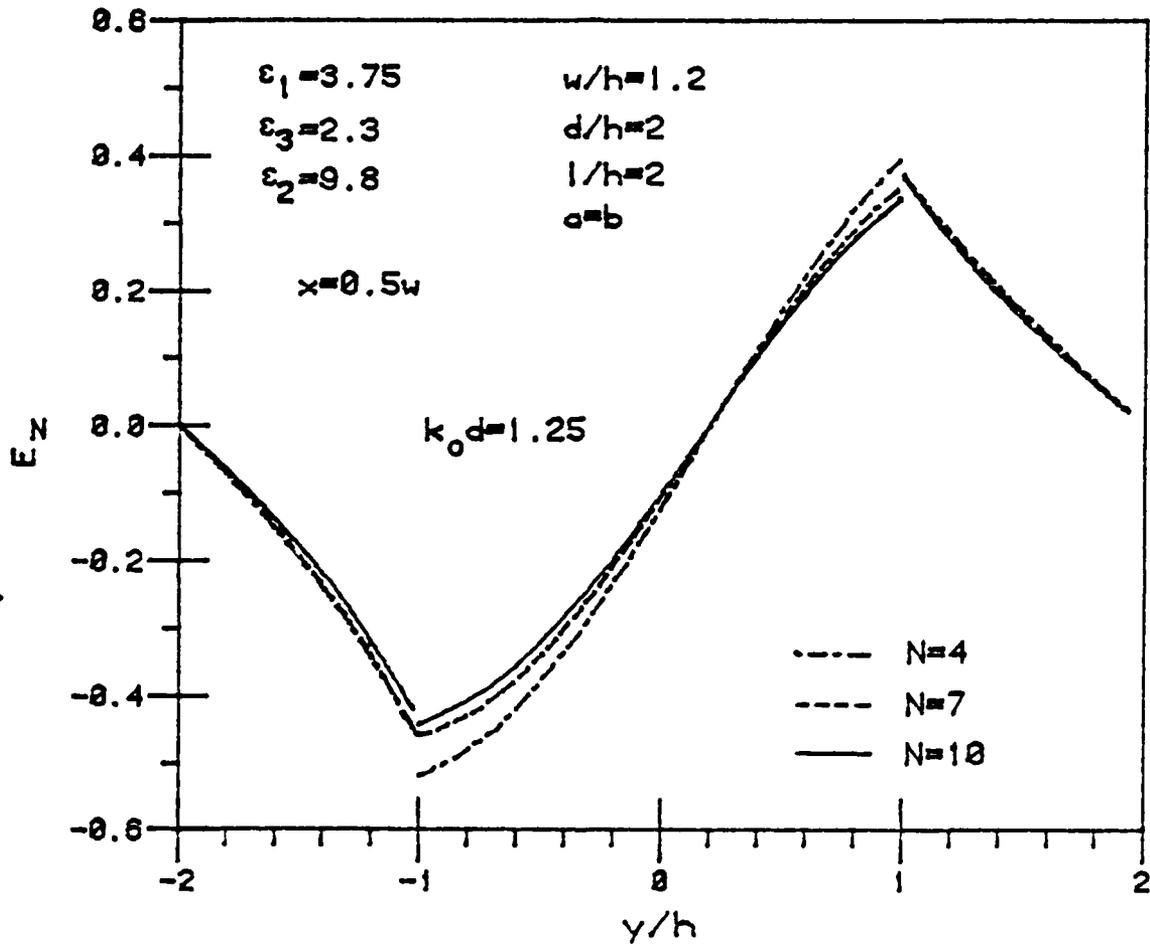
Figure 32. Normalized field distribution of E_z of the E_{11}^y mode in the vertical direction at $x = 0.5w$ in a single suspended H-waveguide whose top and bottom dielectric layers are dissimilar.

more energy is concentrated in the regions with higher dielectric

constants, the field maxima are shifted slightly toward the top

dielectric layer as clearly shown in Figures 29 and 30. As mentioned

earlier, E_y and H_y are not presented since their behaviors closely resemble

H_x and E_x, respectively. Except for the minor field component E_x, all

field components match very well at the $y = \pm h$ planes for $N = 10$.

Typical field distributions in the horizontal direction are shown in

Figures 33 and 34. It is interesting to note that, compared to Figure

27, the fields in Figure 33 decay much faster away from the dielectric

core since the dielectric constant of the core in the latter case is

much higher, and therefore, more energy is concentrated in the core

region. The plot of E_x at $y = 0.5h$ clearly shows that more than four

eigenmodes are necessary to satisfy the boundary conditions at the

$x = \pm w$ interfaces. However, when a few more terms are added, i.e.,

$N = 10$, the matching of this normal electric field component is very

good.

The field distributions of a coupled suspended H-waveguide are similar

to those for other coupled dielectric waveguide structures such as the

insular guides or the inverted strips. Because of the symmetry of

the waveguide structure at the $x = -a$ plane (see Figure 2), the

fields are either symmetric or antisymmetric about that plane. For

the symmetric mode (or even mode), the vertical plane at $x = -a$ is

replaced by an equivalent perfect magnetic conducting (pmc) wall,

whereas for the case of the antisymmetric mode (or odd mode), the

vertical plane is replaced by an equivalent perfect electric conducting
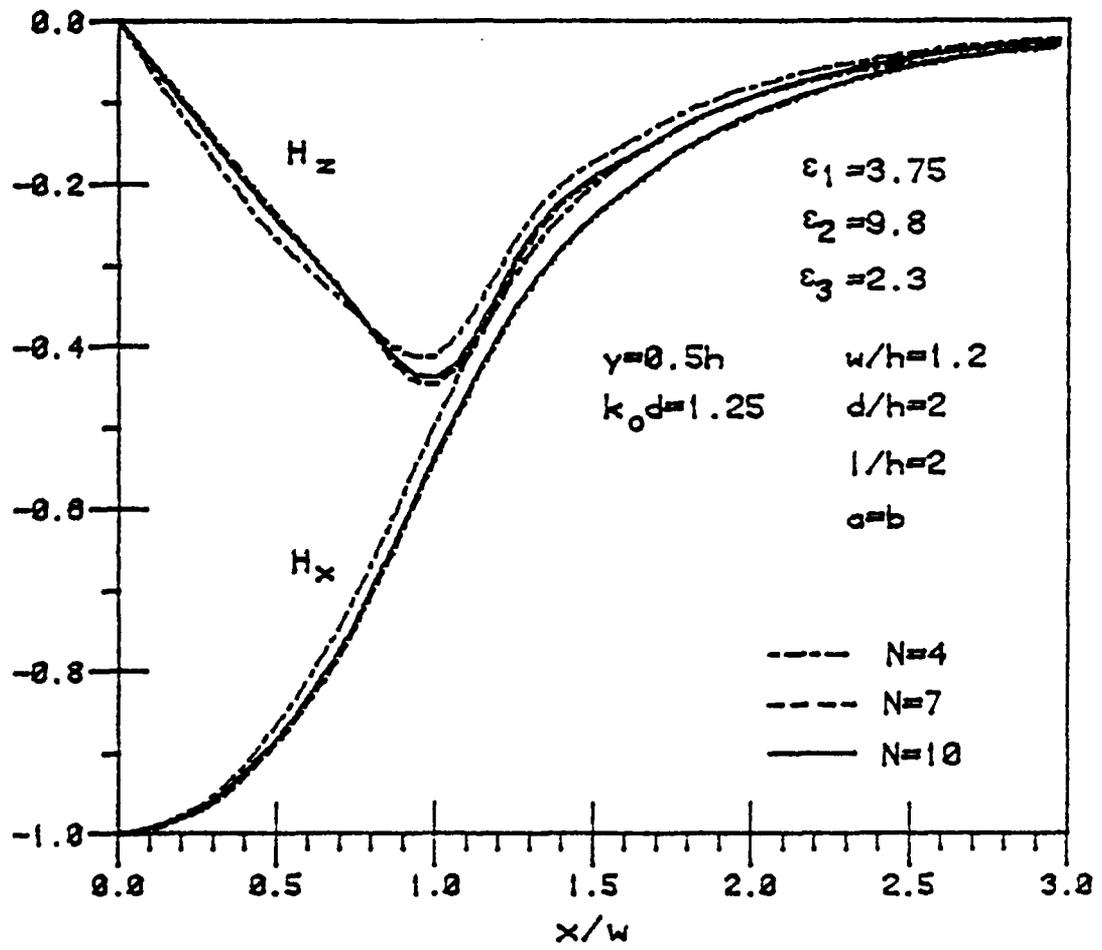
Figure 33. Normalized magnetic field distribution of the E_{11}^y mode in the horizontal direction at $y = 0.5h$ in a single suspended H-waveguide whose dielectric insulating layers are dissimilar.
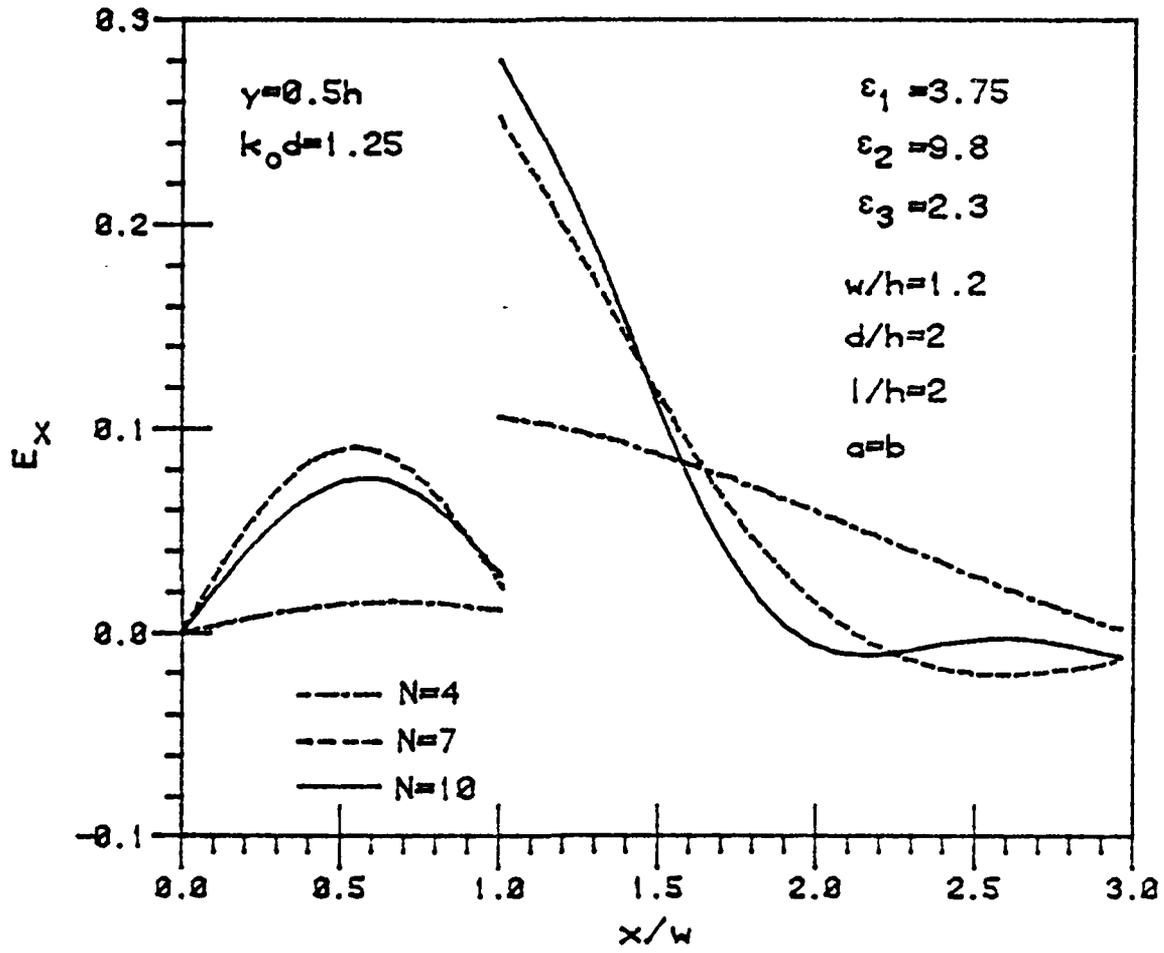
Figure 34. Normalized field distribution of E_x of the E_{11}^y mode in the horizontal direction at $y = 0.5h$ in a single suspended H-waveguide whose dielectric insulating layers are dissimilar.

(pec) wall. The analysis of the total waveguide structure is, therefore, reduced to that shown in Figure 2b. Since the general behavior of the fields in a coupled structure is well-known, only the symmetric mode E^y_{11e} is presented here. The dispersion characteristics of a coupled suspended H-waveguide have been shown in Figures 18 and 19. Figures 35 to 37 are the normalized distributions of four symbolic field components plotted at the y = 0.5h plane. The field strength of the major magnetic component H_x (or E_y) is substantial at the pmc wall as the maxima of the fields are shifted toward the center. As many as ten eigenmodes are necessary to satisfy the boundary condition of the normal electric field component E_x at the x = ±w interfaces. However, the matching process for H_x and H_z converges more quickly.

The transverse field distributions of a single insular guide (see Figure 3c), which is an open dielectric waveguide structure, are plotted for different vertical planes in Figures 38 and 39. In computing the propagation constants and the fields of an insular guide, the metal side walls must be placed far enough from the dielectric core so that their influence on the propagation constant and the field characteristics is negligible. The magnetic field plots in the horizontal direction at y = 0.5h are shown in Figure 40. The matching of these components is very good even for N = 3. However, to obtain an accurate field distribution eight or more eigenmodes must be used.

The investigation of the field distribution in many waveguide structures has been concentrated on the E^y_{11} mode only. The plots of
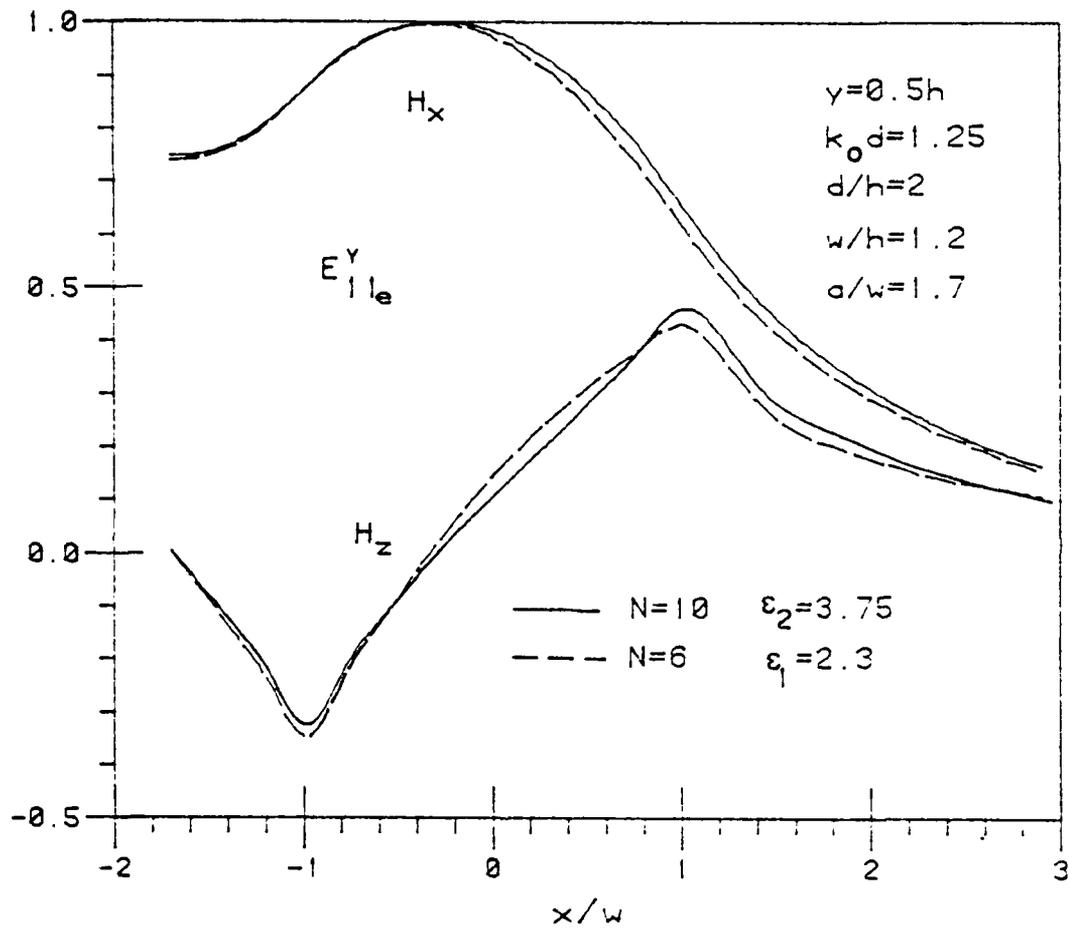
Figure 35. Normalized magnetic field distributions of the E_{11e}^y mode in a coupled suspended H-waveguide at $y = 0.5h$.
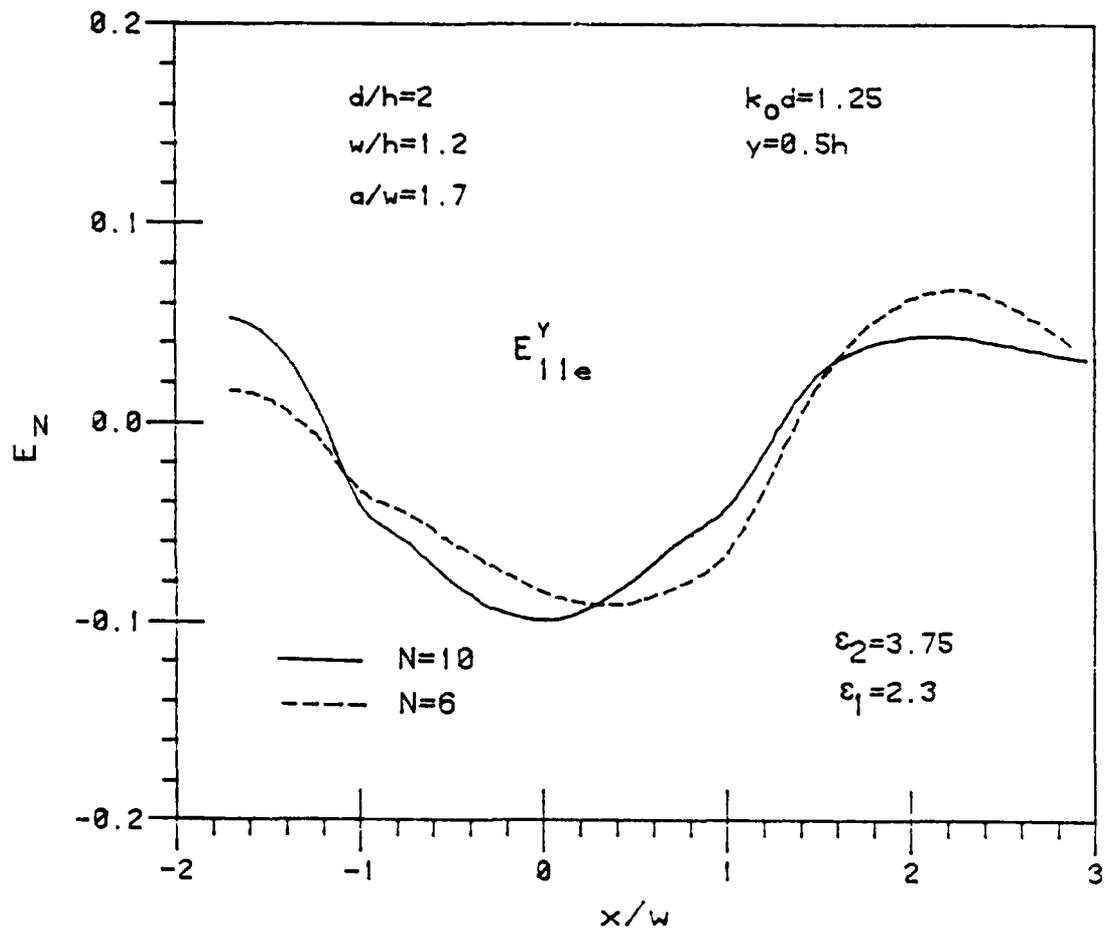
Figure 36. Normalized field distribution of E_z of the E_{11e}^y mode in a coupled suspended H-waveguide at $y = 0.5h$.
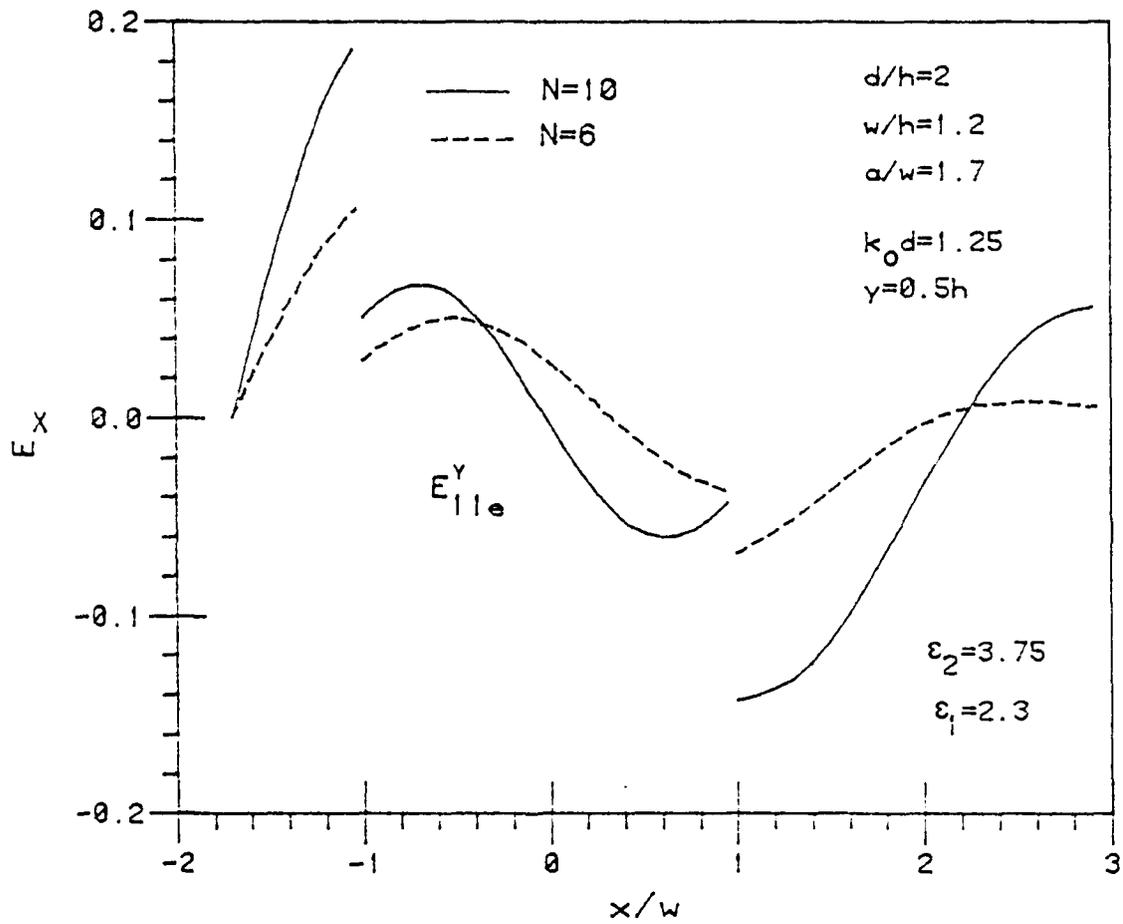
Figure 37. Normalized field distribution of E_x of the E^y_{11e} mode in a coupled suspended H-waveguide at $y = 0.5h$.

0.2

x=w⁻
x=w⁺
x=2w

N=8

E_x

0.0

$\varepsilon_1 = 1$

$\varepsilon_2 = 3.75$

$\varepsilon_3 = 2.3$

w/h=1.5

l/h=3

$k_0 l = 1.6755$

-0.2

-0.4

-3   -2   -1   0   1   2   3   4

y/h
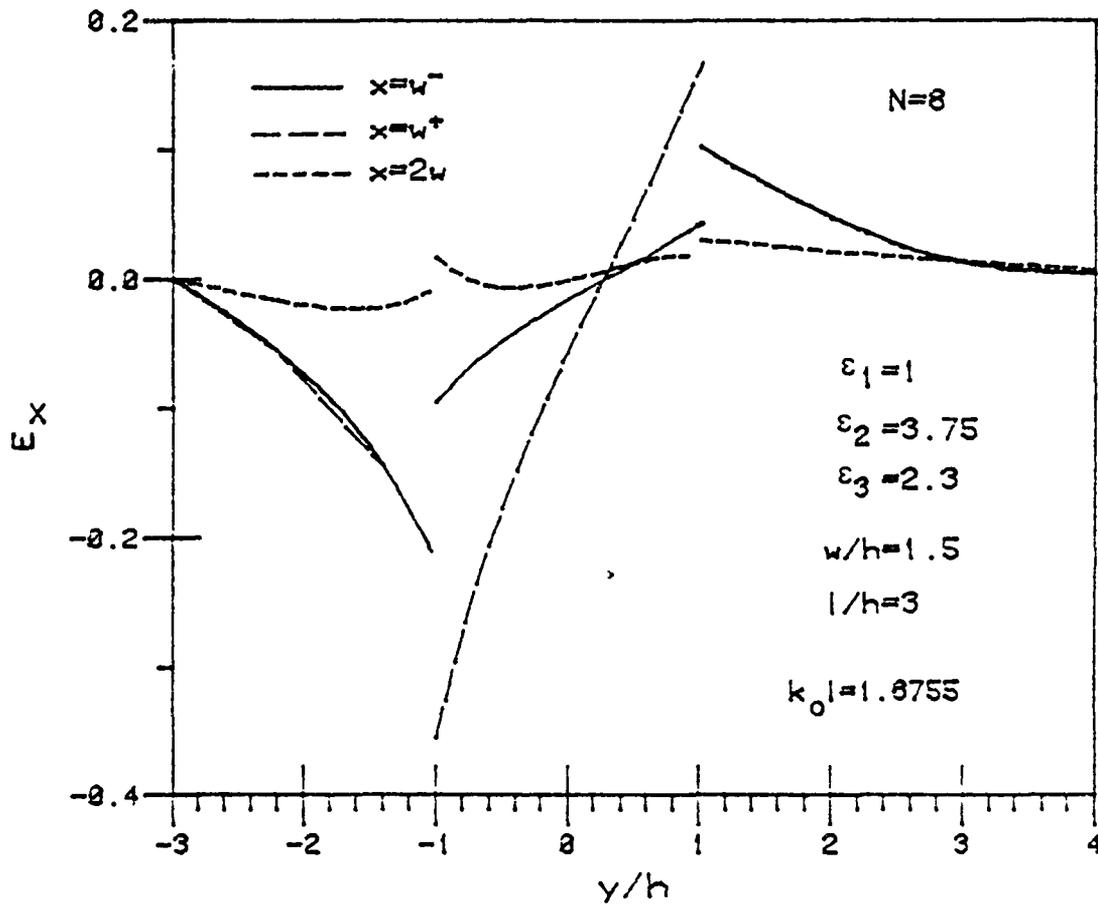
Figure 38. Normalized field distribution of E_x of the E_{11}^y
mode in the vertical direction for different
x-locations in a single insular guide.
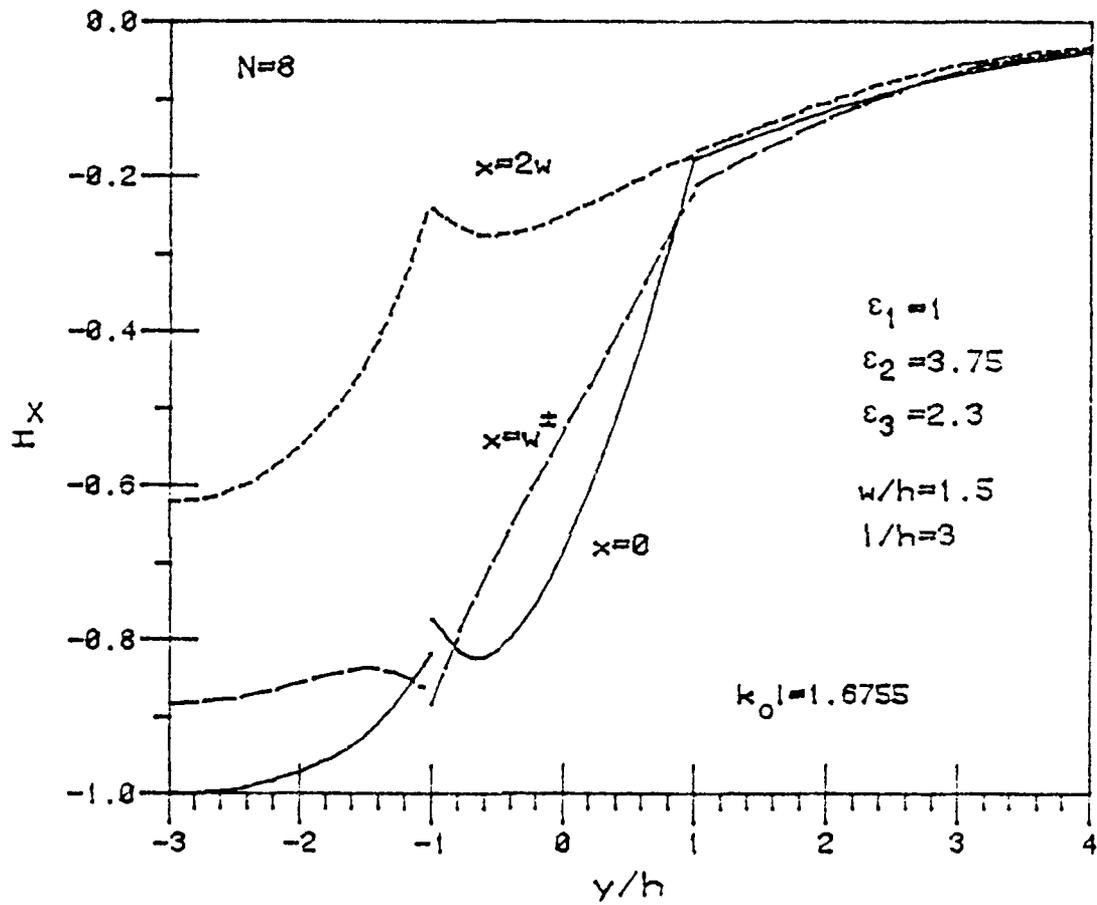
Figure 39. Normalized field distribution of H_x of the E_{11}^y mode in the vertical direction for different x-locations in a single insular guide.
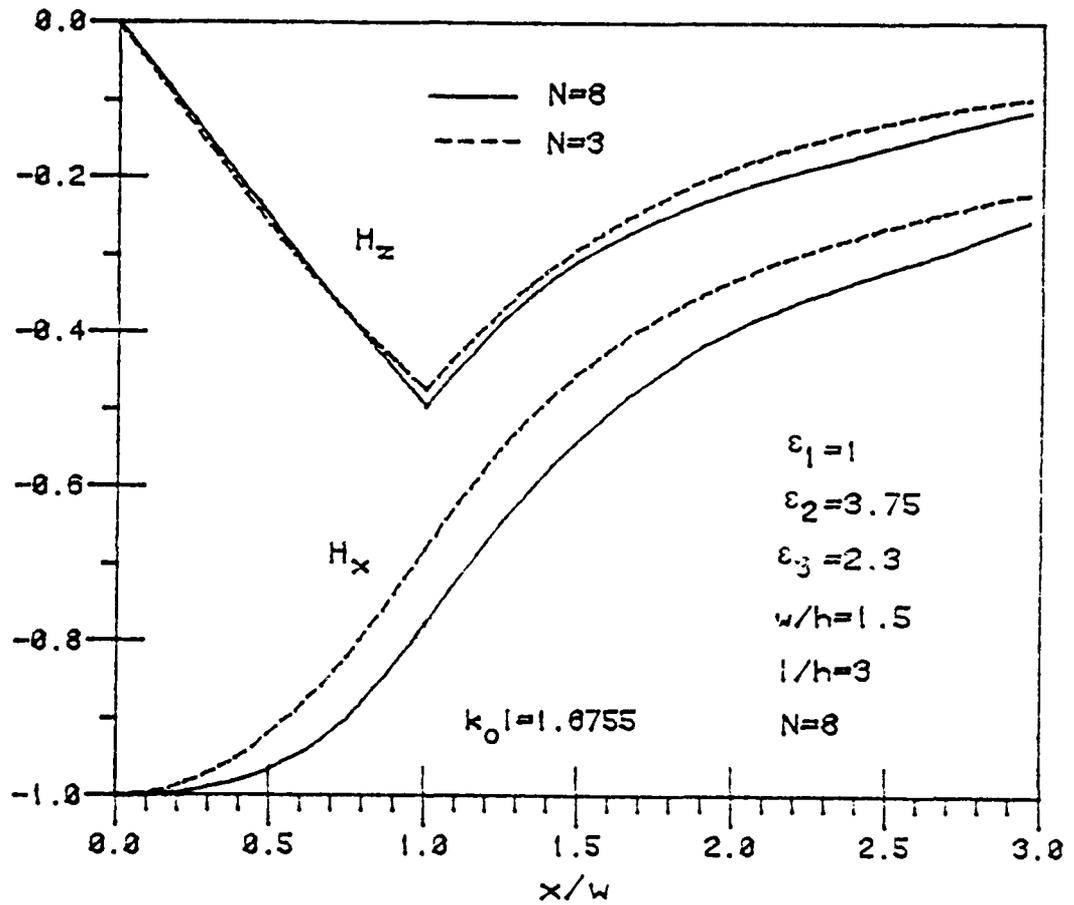
Figure 40. Magnetic field distributions of the E_{11}^y mode in a single insular guide in the horizontal direction at $y = 0.5h$.

E_x, H_x, E_z and H_z, respectively, of the E_{11}^x mode, which has E_x as the major transverse electric field component, in a single suspended H-waveguide are shown in Figures 41 to 44. E_y and H_y are similar to H_x and E_x in this guide and, therefore, are not plotted. Unlike the E_{11}^y mode, the longitudinal fields E_z and H_z of the E_{11}^x mode are very substantial and are comparable to the corresponding major transverse fields (see Figure 45 to 46). At the top and bottom metal ground planes ($y = d, -1$), the tangential H_z is still very significant. In fact, at these locations, H_z becomes the dominant magnetic field component as shown in Figure 47, which is the plot of the normalized magnetic field distributions at $y = d$. For this reason, the metal loss for the E_{11}^x mode is also significant and is primarily due to this magnetic field component. The matching at $x = w$ is very good since, except for the normal electric field component, the fields at $x = w^-$ and $x = w^+$ always coincide. As in the E_{11}^y mode, the matching at the horizontal interfaces $y = \pm h$ is more difficult. Figures 45 and 46 are the plots of the normalized electric and magnetic field components in the horizontal direction at $y = 0.5h$. The matching at the $y = 0.5h$ plane for $N = 8$ is excellent for all components.

3.4   Conclusions

The propagation and field characteristics for two fundamental modes that have polarizations orthogonal to each other in many dielectric waveguide structures have been studied. The method of analysis derived for the suspended H-waveguide is general and can be

80
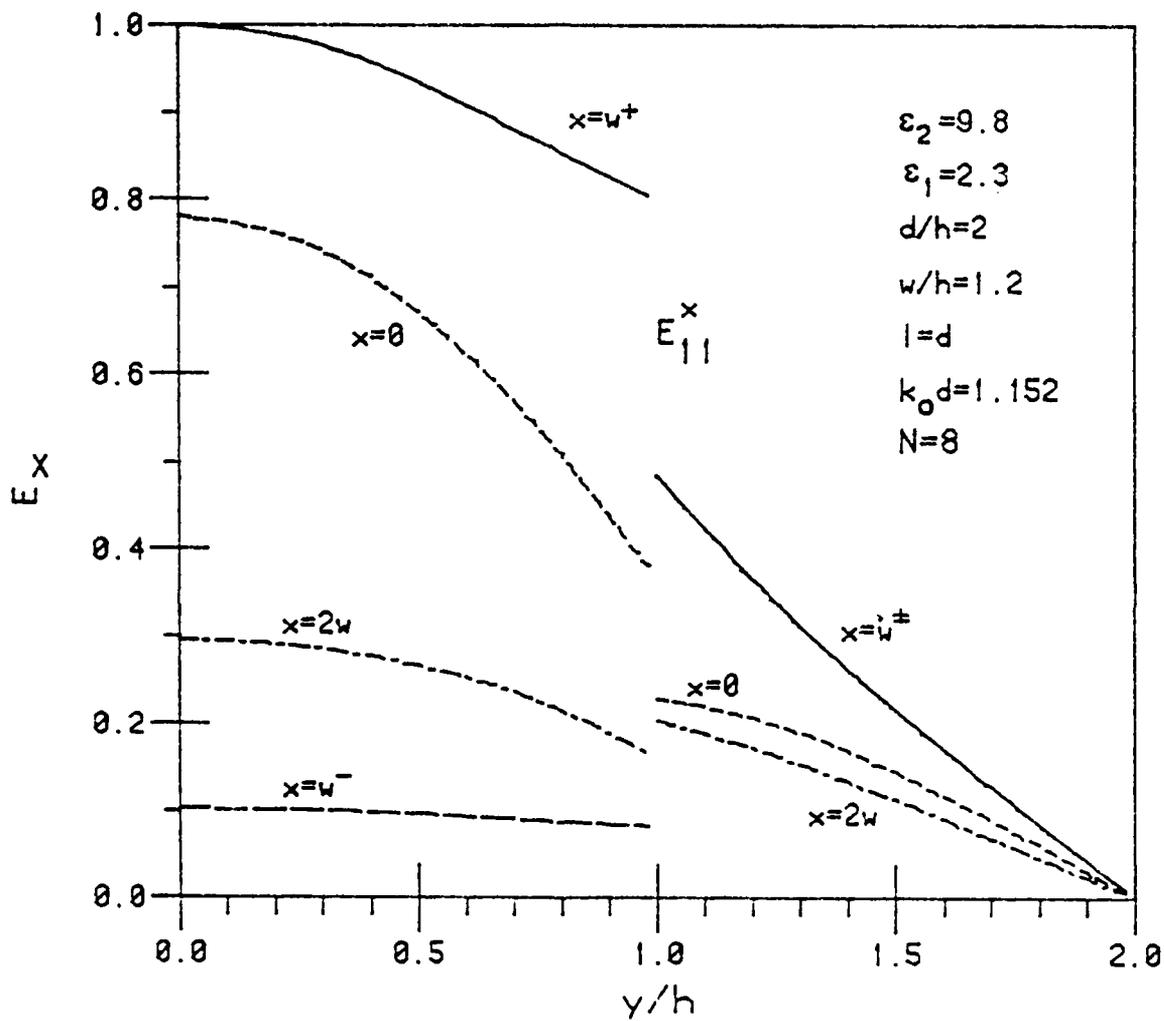
Figure 41. Normalized field distribution of E_x of the E_{11}^y mode in a single suspended H-waveguide. $\varepsilon_1 = \varepsilon_3$.

81
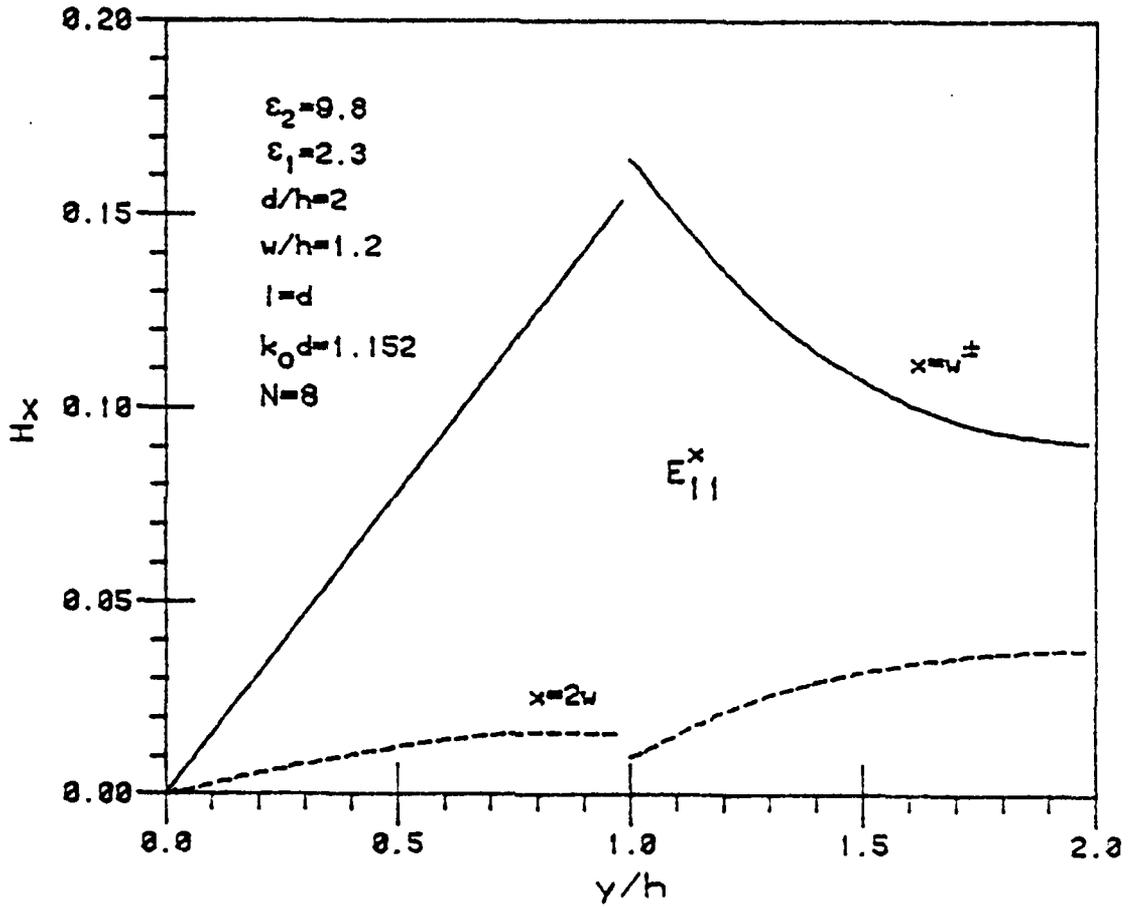
Figure 42. Normalized field distribution of H_x of the E_{11}^x
mode in a single suspended H-waveguide $\varepsilon_1 = \varepsilon_3$.

82
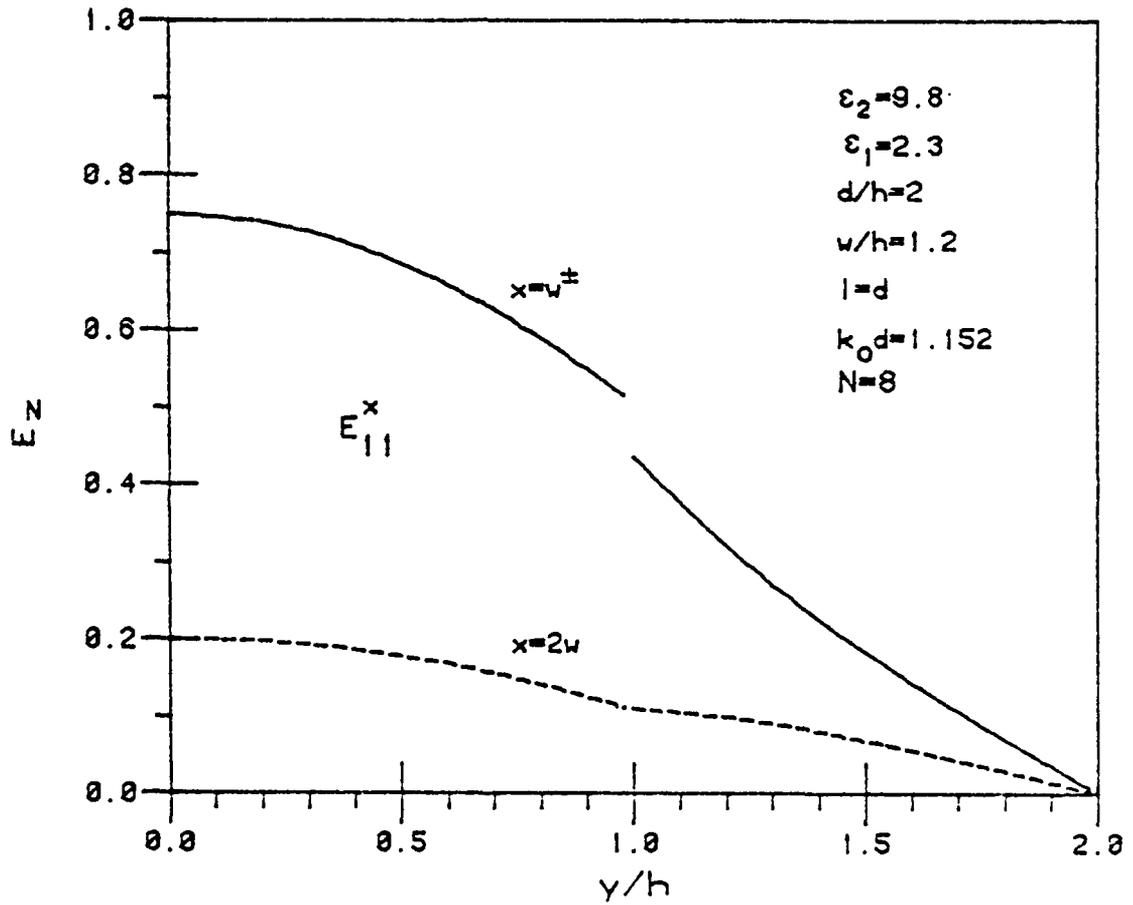
Figure 43. Normalized field distribution of E_z of the E_{11}^x mode in a single suspended H-waveguide. $\varepsilon_1 = \varepsilon_3$.
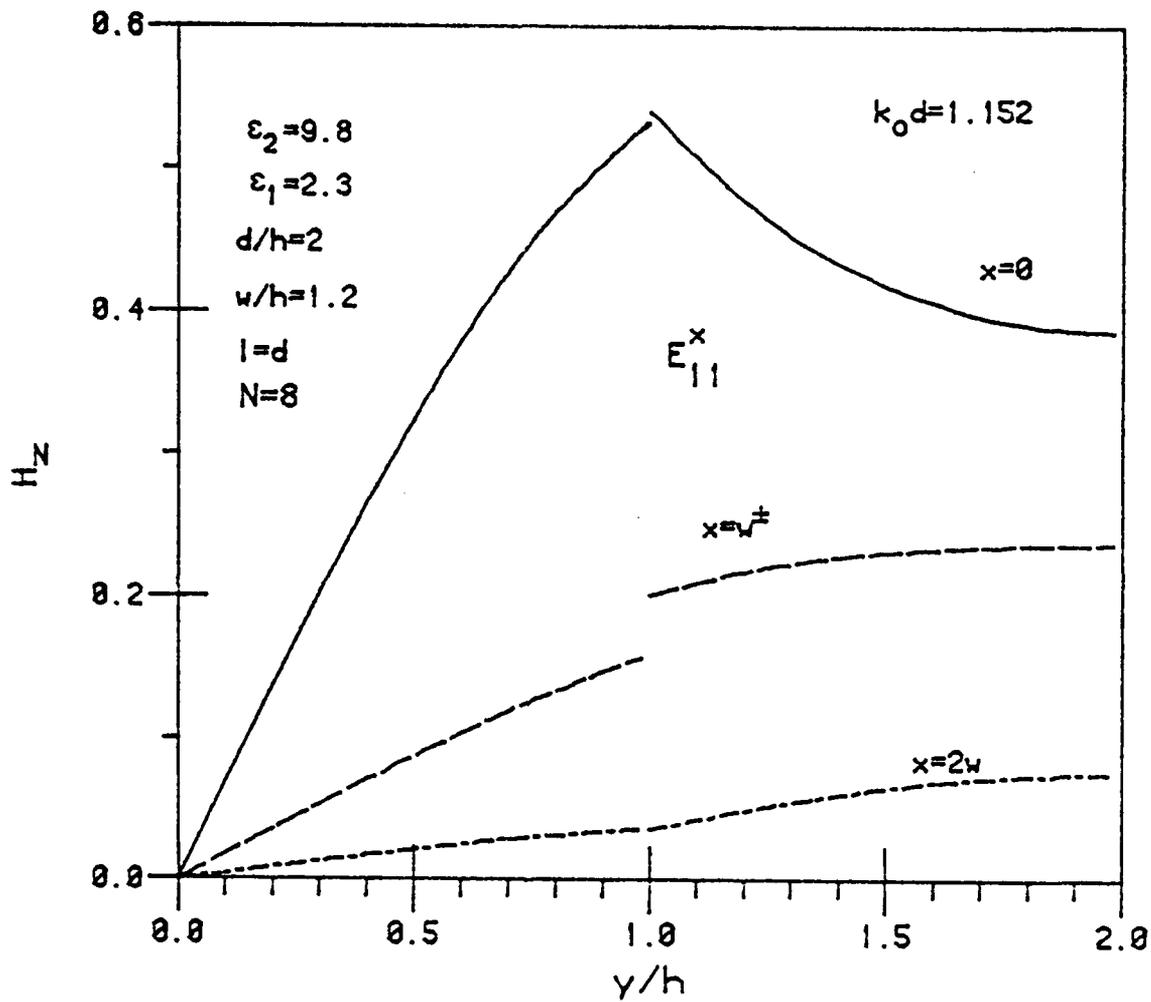
Figure 44. Normalized field distribution of H_z of E_{11}^x mode in a single suspended H-waveguide. $\varepsilon_1 = \varepsilon_3$.
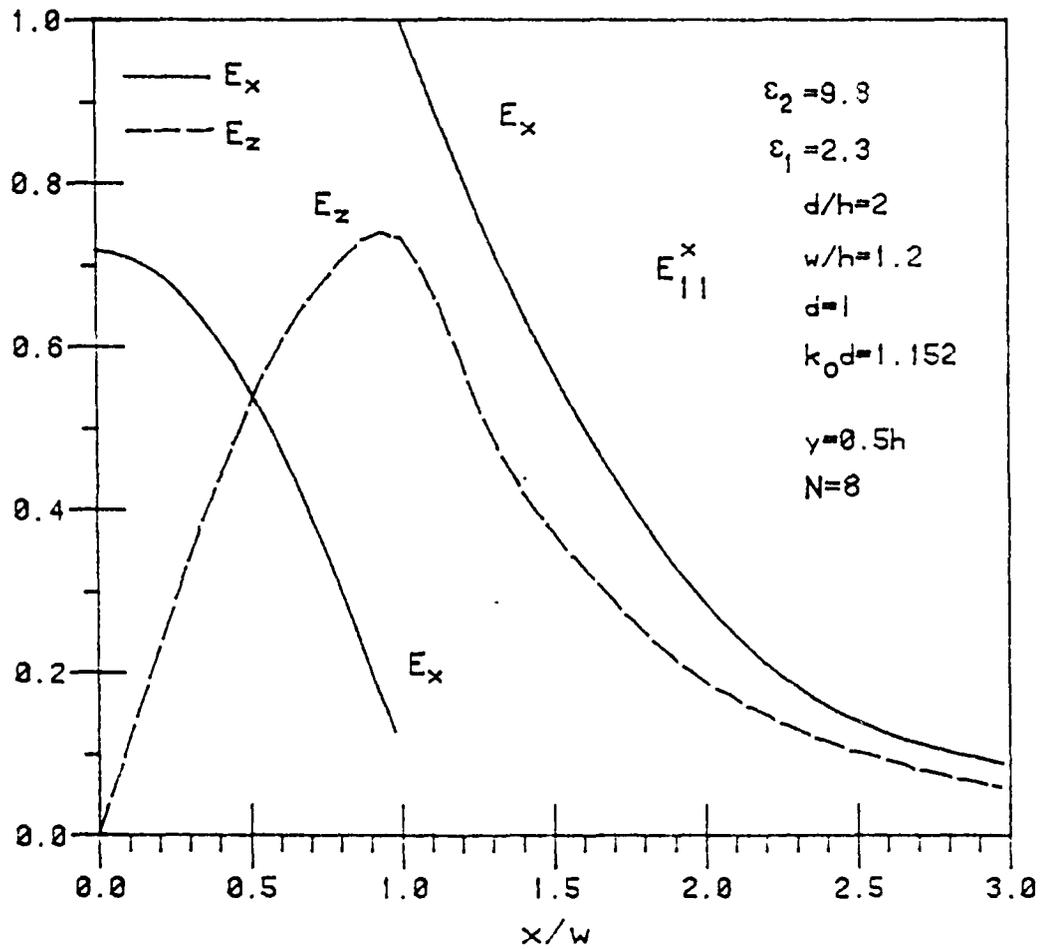
Figure 45. Normalized electric field components of the E_{11}^x mode in the horizontal direction at $y = 0.5h$. $\varepsilon_1 = \varepsilon_3$.
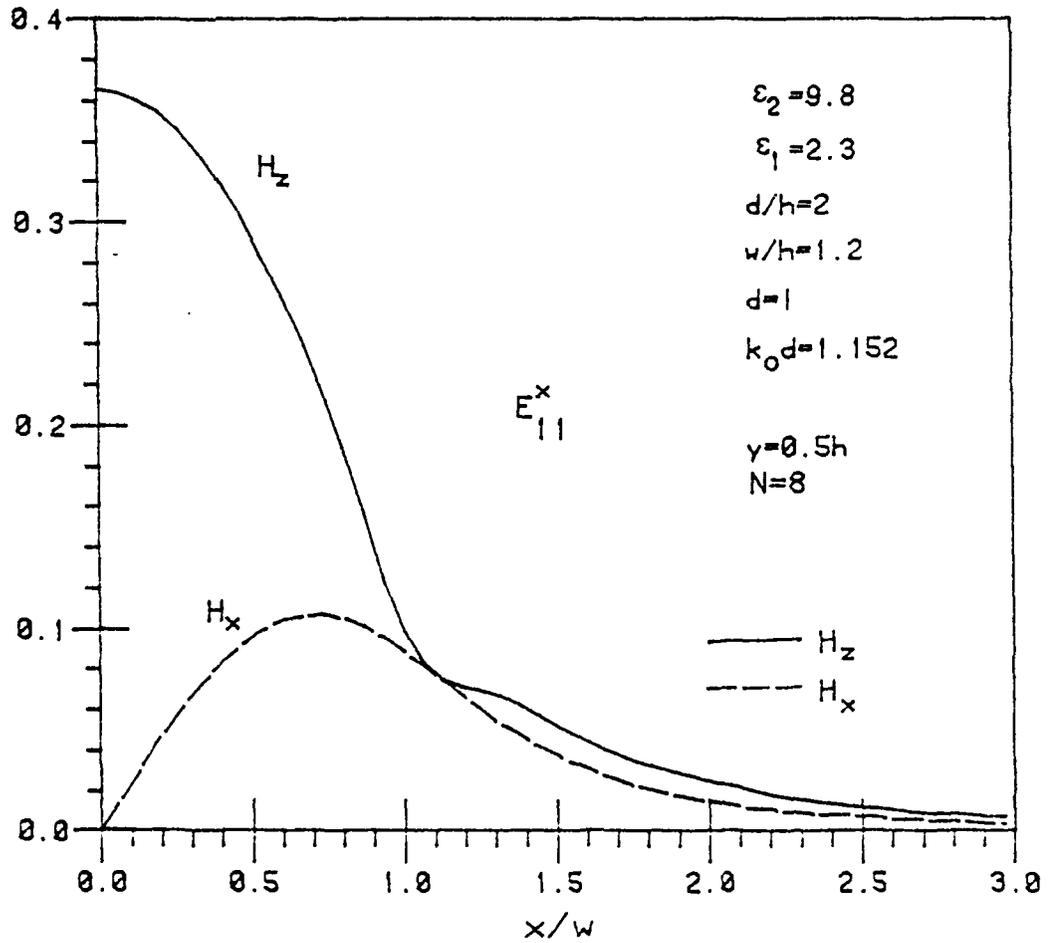
Figure 46. Normalized magnetic field components of the E_{11}^x mode in the horizontal direction at $y = 0.5h$. $\varepsilon_1 = \varepsilon_3$.
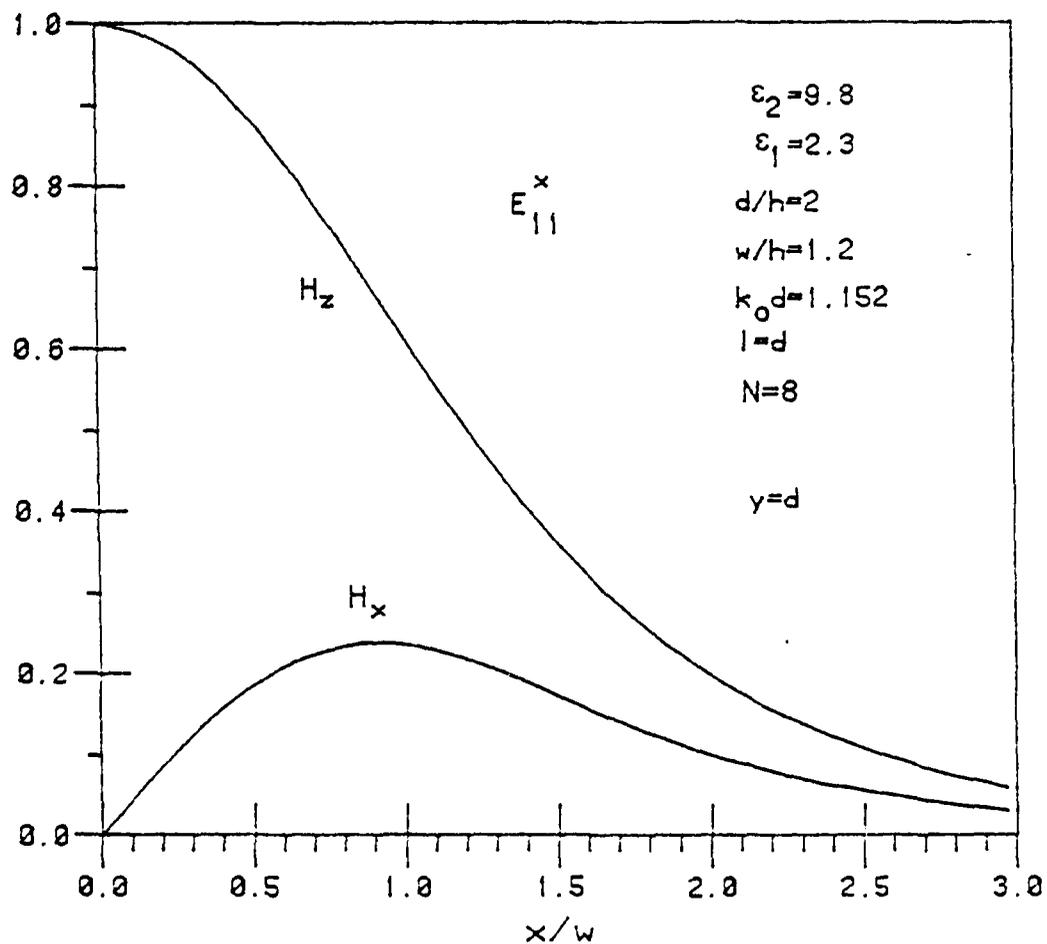
Figure 47. Normalized magnetic field distributions of the E_{11}^x mode at the top metal plane in a single suspended H-waveguide. $\varepsilon_1 = \varepsilon_3$.

applied directly to other single and coupled planar structures of
rectangular cross section. Even though the effective parameter
approximations do not provide very accurate results for the propagation
constants, in some cases they provide very useful information on the
whereabouts and the existences of certain modes which, in turn, can
be used as the initial values for iterating in the mode matching tech-
nique. By doing so, the computation time that could be wasted on a
random search by the mode-matching technique can be eliminated. For a
high dielectric constant or at high normalized frequency, both techniques
agree well. The theoretical and experimental results for many wave-
guide structures agree well throughout.

4. LOSS CHARACTERISTICS OF A SUSPENDED H-WAVEGUIDE

The major sources of loss in most dielectric-based waveguide structures for millimeter-wave applications operating at frequencies beyond cutoff are the dielectric loss, the metal loss of conducting walls and the radiation loss due to bending. If the radius of curvature is sufficiently large, a general technique for determining the radiation loss has been presented by several authors [28],[29] and, will not be discussed here. The dielectric and metal losses of many dielectric-based waveguide structures, such as the H-guide or the image guide, have been previously investigated [22],[30]-[32]. Therefore, only dielectric and metal loss characteristics of a suspended H-waveguide will be studied in this section.

4.1 Metal Loss

In general, the metal loss is proportional to the square root of the operating frequency and the intensities of the tangential magnetic fields at the metal surfaces. A conventional image guide that supports the E^y_{pq} modes has the dominant magnetic field H_x parallel to the ground plane. Metal losses are therefore dominant as there is no separation between the dielectric core and the metal ground plane. Recently, this metal loss has been reduced by adding a thin dielectric layer of lower dielectric constant between the dielectric core and the metal ground plane [4],[7], since the fields decay rapidly in the

dielectric layer. The proposed suspended H-waveguide utilizes
the same principle to minimize the metal loss. Two low-loss dielectric
layers are inserted between the dielectric core and the metal surfaces.
This principle also applies to the E_{11}^x mode since the parallel magnetic
field components also decay rapidly in the insulating layers (see
Figures 42 and 44). The increase of dielectric loss due to the addition
of the insulating dielectric layers will be discussed later.

The attenuation in nepers per unit length can be calculated by
the conventional power loss method, i.e.,

$$\alpha_m = \frac{P_L}{2P_T} \tag{32}$$

where P_L is the metal loss per unit length and P_T is the transmitted
power in the guide. P_L and P_T are given by

$$P_L = \frac{1}{2} R_s \oint |H_{tan}|^2 \, dl \tag{33}$$

$$P_T = \frac{1}{2} R_e \iint (E \times H^*) \cdot \hat{z} \, da \tag{34}$$

where $|H_{tan}|^2 = |H_x|^2 + |H_y|^2 + |H_z|^2$ at the metal surfaces $\tag{35}$

$$R_s = \left(\frac{\omega \mu_0}{2\sigma_m}\right)^{\frac{1}{2}} = \text{surface resistance, and} \tag{36}$$

σ_m is the surface conductivity of metal. Here, it is assumed that the
field configurations in the guide are not affected by the wall conduc-
tivity. The field components in all regions are given in Eqs. (1)-(6).

Figures 48 and 49 are the plots of the attenuation in decibels per meter of the E_{11}^{y} mode in a single suspended H-waveguide whose top and bottom dielectric layers are identical. In Figure 48, the dielectric constant of the core is 9.8 whereas ε_r = 3.75 in Figure 49. It is evident from these figures that the metal loss is much lower when two dielectric insulating layers are inserted. As explained previously, the tangential magnetic fields decay rapidly toward the metal ground plane in the dielectric layers whose dielectric constants are lower than that of the core. The surface current on the metal plane is therefore small. In the absence of the dielectric layers, i.e., h/d = 1, the attenuation increases sharply. This is due to the fact that the dominant tangential magnetic field H_x is constant in the vertical direction throughout the guide.

It is also important that the ratio h/d should not be too small. For small h/d, e.g., h/d=0.2, the fields are weakly bound. Consequently, the tangential magnetic fields at the metal planes are significant and higher metal losses occur. Except for h/d = 1, the attenuation curves for all other cases in Figure 48 decrease as frequency increases. This feature can be beneficial when the guide is operated at the milli- meter-wave frequency range. In Figure 49, where ε_2 is much lower, the attenuation curves first increase then start to turn downward sharply as frequency increases. At lower frequencies, the fields are weakly bound, and the waveguide resembles an empty parallel plate waveguide. The attenuation is roughly proportional to the square root of the frequency. At higher frequencies (or higher dielectric constant of the

MICROCOPY RESOLUTION TEST CHART
NATIONAL BUREAU OF STANDARDS-1963-A

91
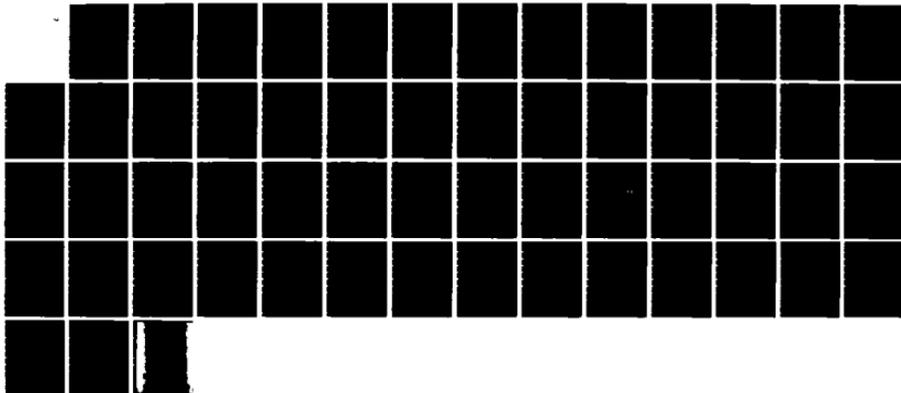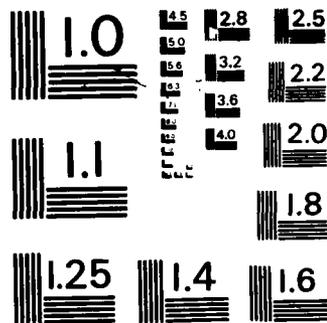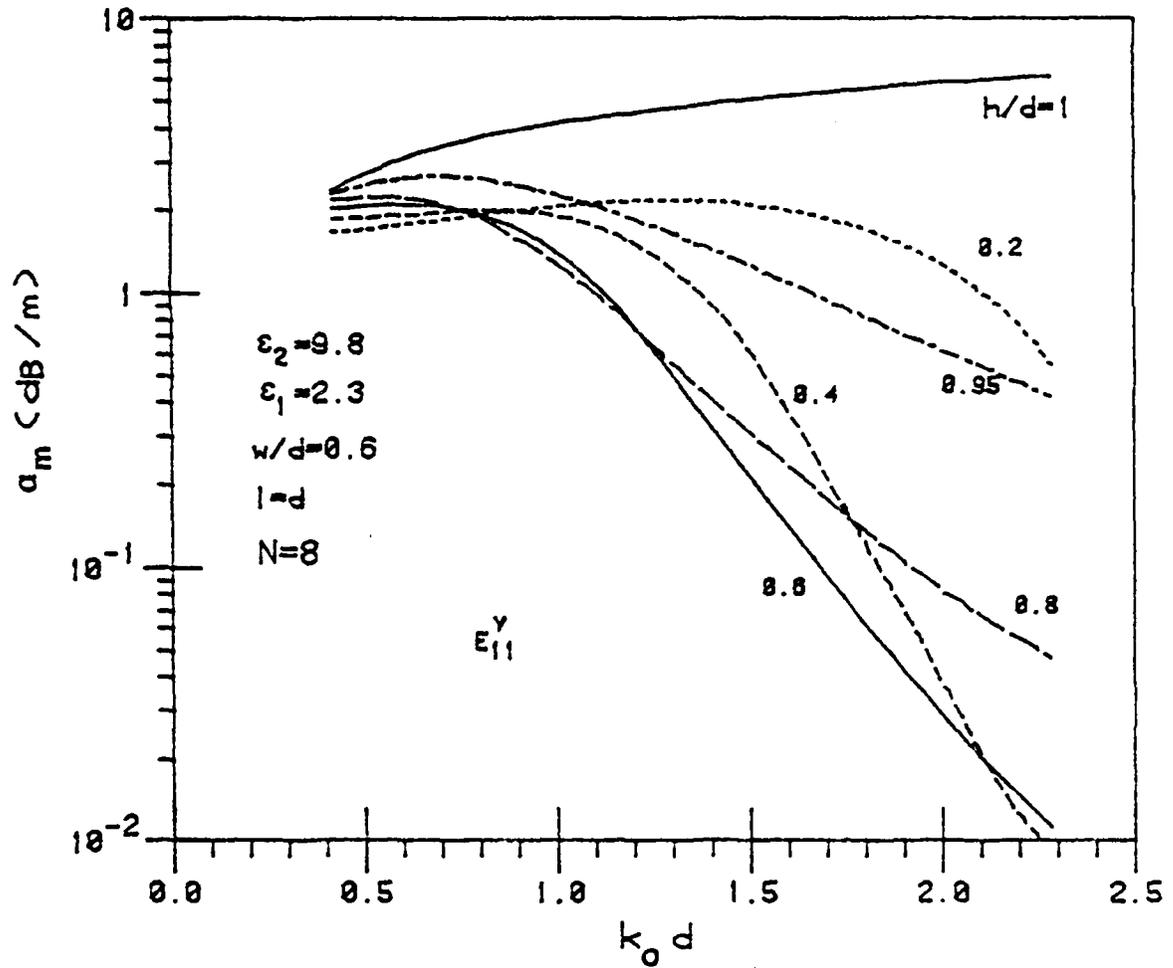
Figure 48. Attenuation of the E_{11}^{y} mode in decibels per meter due to the metal loss in a single suspended H-waveguide. $\sigma_m = 6.17 \times 10^7$.

92
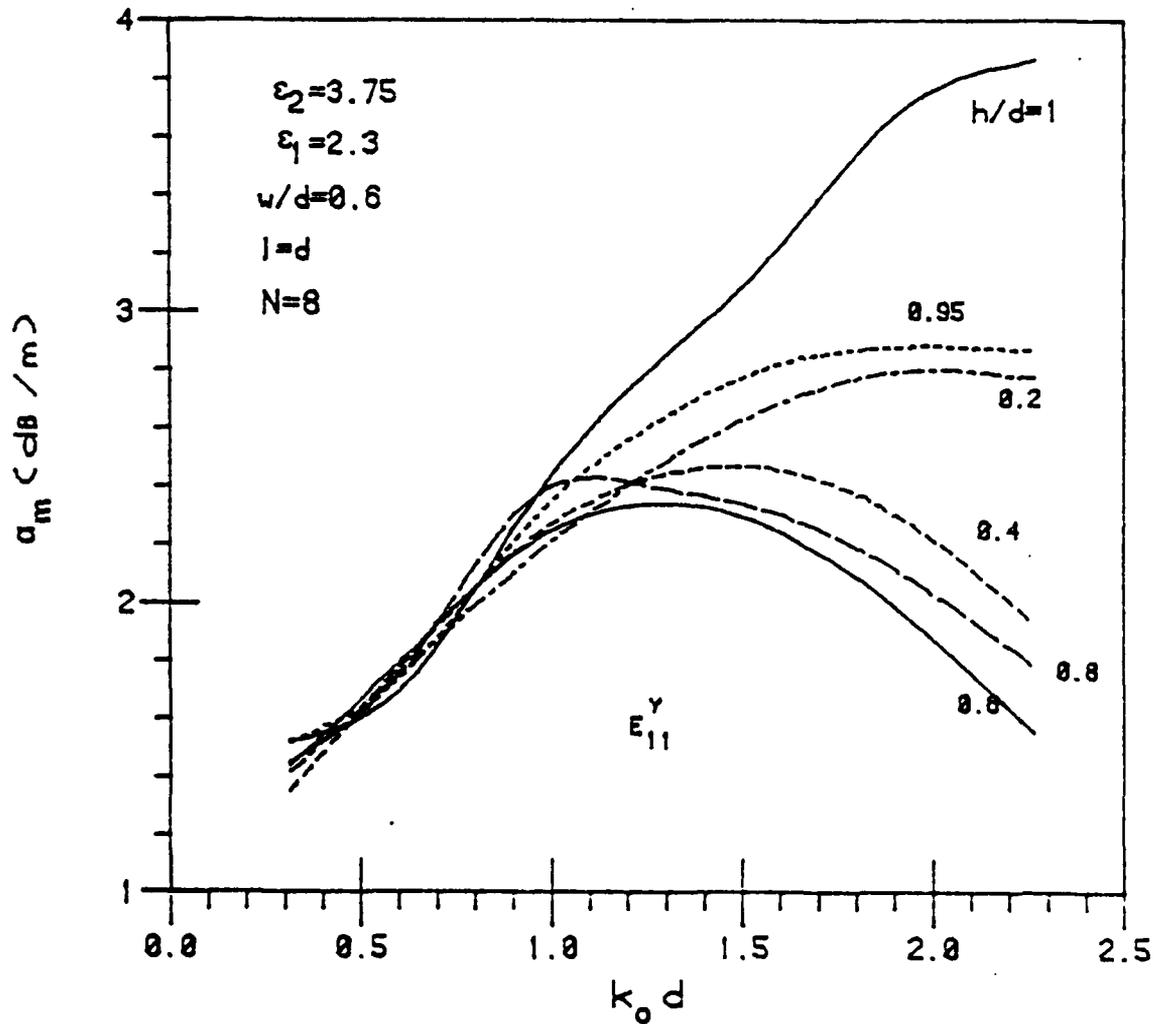
Figure 49. Attenuation of the E_{11}^y mode in decibels per meter due to the metal loss in a single suspended H-waveguide. $\sigma_m = 6.17 \times 10^7$.

core), the fields become tightly bound to the dielectric core. The intensities of the tangential magnetic fields at the metal planes are small resulting in smaller metal loss as indicated in Figure 49.

The attenuation curves in decibels per unit length of the E_{11}^{x} mode in a single suspended H-waveguide are plotted in Figure 50. With the addition of the two dielectric insulating layers, the metal loss is significantly reduced as clearly indicated by the $h/d = 0.2$, 0.4 and 0.6 curves. Near cutoff, the metal loss of the E_{11}^{x} mode is very high but decreases sharply as frequency increases. In general, with the exception that the loss in the E_{11}^{y} mode is primarily due to the transverse magnetic field component H_x whereas the loss in the E_{11}^{x} mode is mostly due to the longitudinal field component H_z, the metal loss characteristics of the E_{11}^{y} mode and the E_{11}^{x} mode are very similar.

4.2 Dielectric Loss

The introduction of the dielectric insulating layers in a suspended H-waveguide significantly reduces the metal loss due to finite conductivity of the walls. However, the addition of a large volume of lossy dielectric materials may cause a higher dielectric loss. Therefore, it is necessary to study the dielectric loss characteristics of the guide to obtain a complete overall loss figure for a new waveguide structure.

The power loss technique can also be used to calculate the dielectric loss. However, field computation derived from the mode-matching technique for the power loss approach is very time-consuming.

94
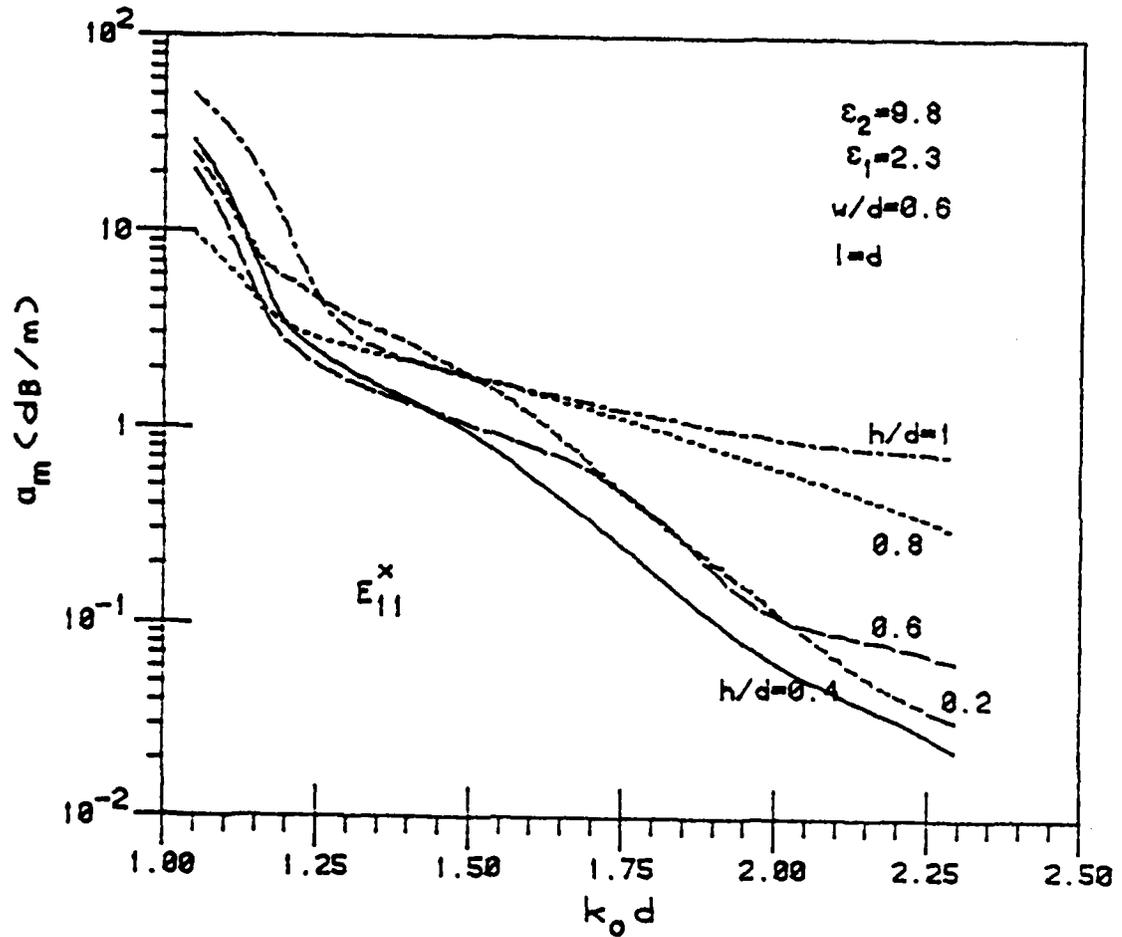
Figure 50. Attenuation of the E_{11}^x mode in decibels per meter due
to the metal loss in a single suspended H-waveguide.
$\sigma_m = 6.17 \times 10^7$.

By introducing a complex dielectric constant to allow for a small loss in the dielectrics, the attenuation constant α_d associated with lossy dielectrics can be obtained directly by a perturbation technique which is based on the solution of the lossless structure.

The characteristic equation for the propagation constant of a lossless suspended H-waveguide can be symbolically written as

$$D(\varepsilon_1, \varepsilon_2, \varepsilon_3, k_z, \omega) = 0 \qquad (37)$$

where D is the determinant of the system of linear and homogeneous equations shown in Eq. (21).

In order to calculate α_d, the parameters in (37) are replaced by their complex counterparts. The characteristic equation for the complex propagation constant $\bar{k}_z = k_z - j\alpha_d$ becomes

$$D(\bar{\varepsilon}_1, \bar{\varepsilon}_2, \bar{\varepsilon}_3, k_z - j\alpha_d, \omega) = 0 \qquad (38)$$

where

$$\bar{\varepsilon}_1 = \varepsilon_1 (1 - j \tan \delta_1)$$

$$\bar{\varepsilon}_2 = \varepsilon_2 (1 - j \tan \delta_2) \qquad (39)$$

$$\bar{\varepsilon}_3 = \varepsilon_3 (1 - j \tan \delta_3)$$

Tan δ_i, $i = 1,2,3$, is the dielectric loss tangent in the respective region.

Assuming that $\varepsilon_i \tan \delta_i$ and α_d are small, the left-hand side of (38) can be approximated by a Taylor's series in powers of $j\alpha_i \tan \delta_i$

and $j\alpha_d$ about the solution of a lossless structure [33]. Retaining only the first-ordered terms, Eq. (38) becomes

$$D(\epsilon_1,\epsilon_2,\epsilon_3,k_z,\omega) + j \sum_{i=1}^{3} \epsilon_i \tan \delta_i \frac{\partial}{\partial \epsilon_i} D(\epsilon_1,\epsilon_2,\epsilon_3,k_z,\omega)$$

$$+ j\alpha_d \frac{\partial}{\partial k_z} D(\epsilon_1,\epsilon_2,\epsilon_3,k_z,\omega) = 0 \qquad (40)$$

The first term of (40) is zero by virtue of (38); consequently,

$$\alpha_d = - \frac{\sum_{i=1}^{3} \epsilon_i \tan\delta_i \frac{\partial D}{\partial \epsilon_i}}{\frac{\partial D}{\partial k_z}} \qquad (41)$$

All the partial derivatives in (41) are evaluated numerically by the finite-difference technique [34] once the longitudinal propagation constant k_z of the lossless structure has been determined using the mode-matching method. In the calculations of the partial derivatives, it was observed that the solutions converged quickly after a few iterations then began to oscillate. The computations should be terminated before this oscillation occurs.

Figure 51 shows the attenuation constants due to lossy dielectrics of the E_{11}^y mode in a single, suspended H-waveguide as a function of the normalized free-space wavenumber. It is clear that the dielectric insulating layers cause higher dielectric losses. At lower frequencies, the fields are weakly bound to the low-loss dielectric core. More energy is stored in the substrate regions which have a much higher
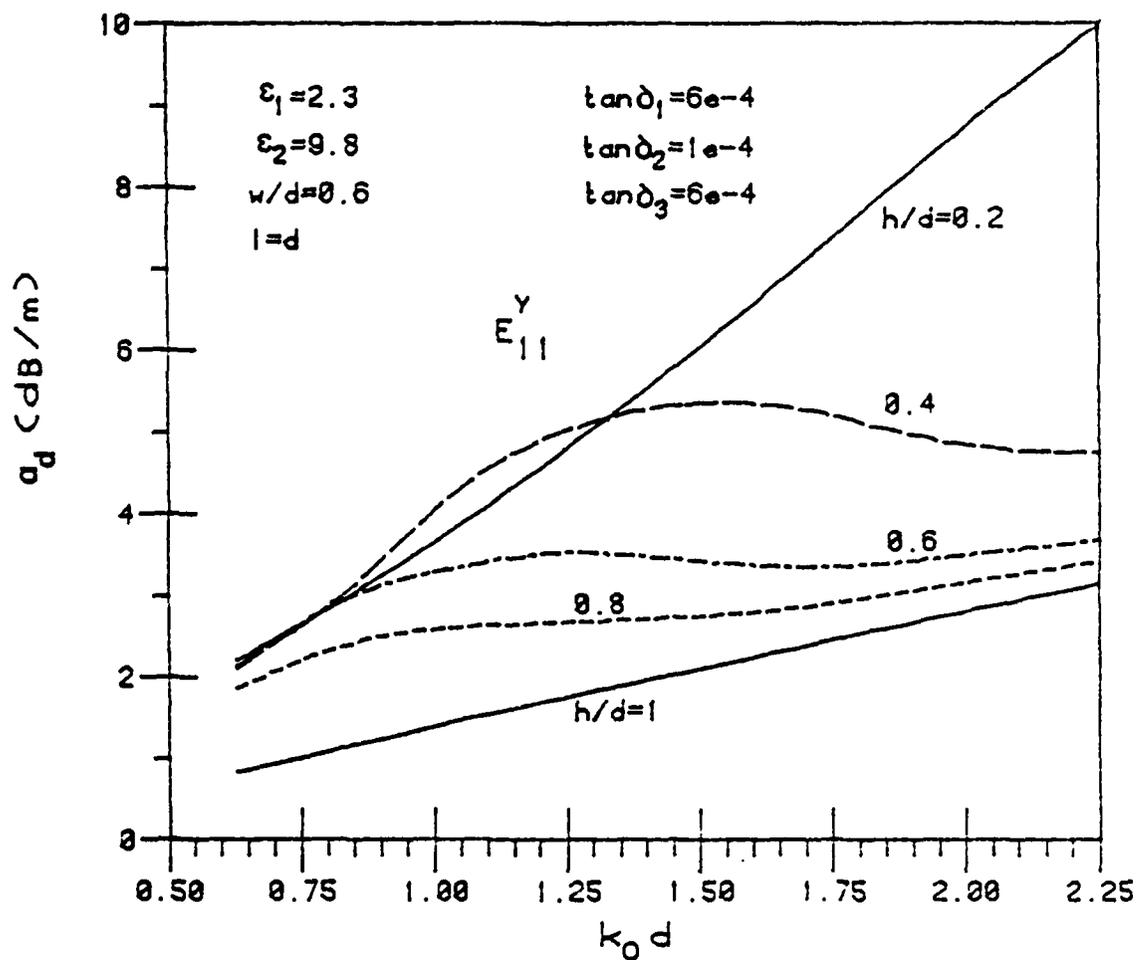
Figure 51. Attenuation constant in decibels per meter of the E_{11}^y mode in a single, suspended H-waveguide.

dielectric loss tangent and, therefore, higher dielectric loss. As frequency increases, most of the electromagnetic energy is stored in the core, which results in lower dielectric loss. Since the loss tangents of the substrates are much higher than the loss tangent of the dielectric core in this case, e.g., $\tan \delta_1 / \tan \delta_2 = 6$, most of the dielectric loss is due to the substrates. If a lower-loss copper-cladded dielectric sheet is available, the dielectric loss of the suspended H-waveguide should be much lower. However, for given waveguide parameters, the total (dielectric and metal) loss of the suspended H-waveguide (h/d = 0.6 and 0.8) is still lower than the total loss of a conventional H-guide (h/d = 1) as Figures 48 and 51 indicated. For h/d = 0.2 and 1 in Figure 51, the dielectric loss increases monotonically as a function of frequency.

Figure 52 shows the attenuation constant due to lossy dielectrics in decibels per meter of the E_{11}^x mode in a single, suspended H-waveguide as a function of the normalized free-space wavenumber. Near cutoff, the dielectric loss is extremely high but decreases sharply as frequency increases. For h/d = 0.6 and 0.8, the dielectric loss curves of the E_{11}^x mode in a suspended H-waveguide are very close to the curve of a conventional H-guide (h/d = 1). The combined total loss, which consists of the dielectric loss and the metal loss, is, therefore, much less if two dielectric layers are inserted since the metal loss of a suspended H-waveguide is very low as compared to that for a conventional H-waveguide. In Figures 50 and 52, the total loss of the E_{11}^x mode is lowest when the ratio h/d is about 0.6.
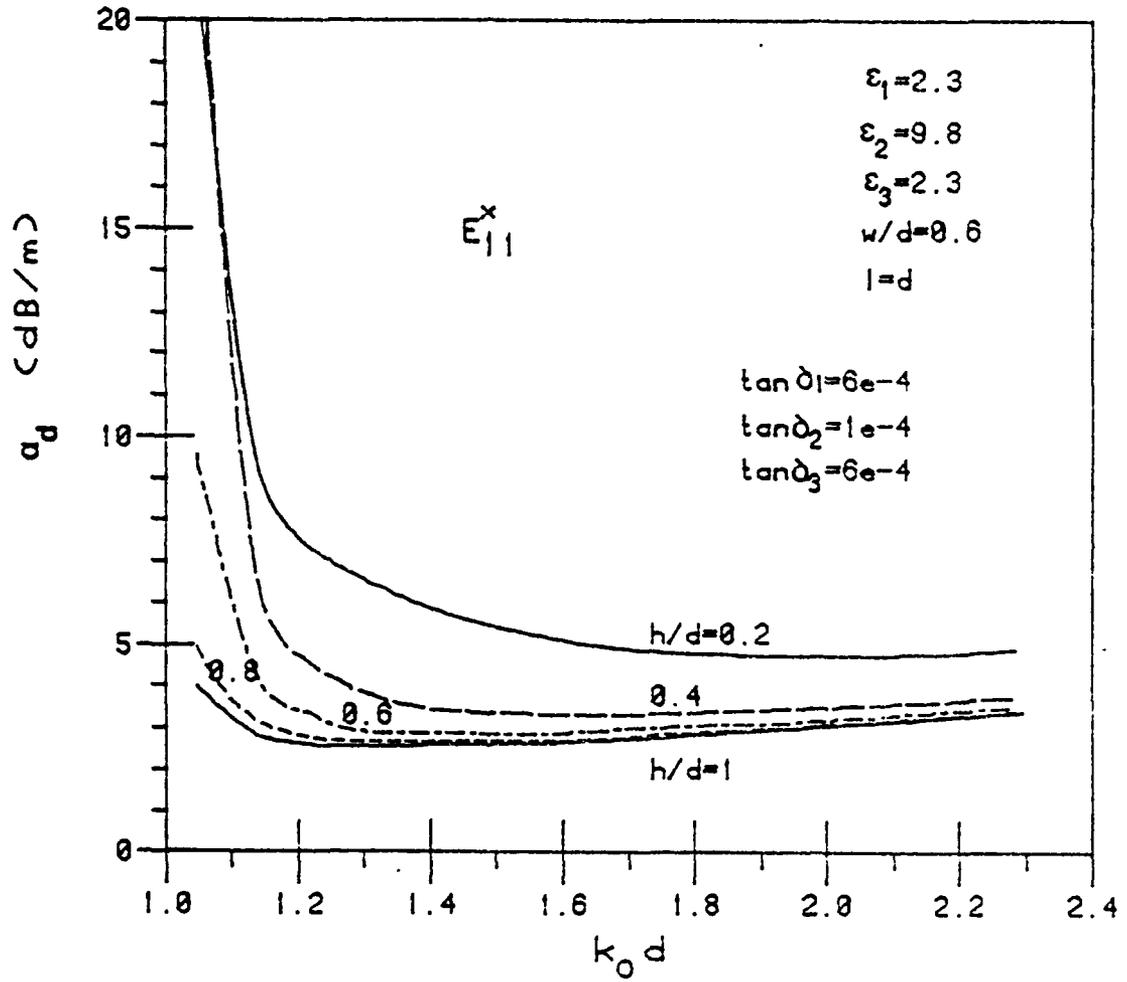
Figure 52. Attenuation constant in decibels per meter of the E_{11}^x
mode in a single, suspended H-waveguide.

In Figures 48 to 52, it appears that the dielectric losses dominate the total loss figure. However, in practice, the surface conductivity at the millimeter wavelength becomes lower [35], and the metal losses become higher. The impact of the suspended H-waveguide should be more profound since the control of the metal losses becomes very important at the millimeter wavelengths.

5. APPLICATIONS

The emergence of the dielectric-based millimeter-wave integrated
circuits requires the development of a totally new class of dielectric
components. In a conventional microwave circuit, discrete components
are connected together by many types of connectors to form a complete
system. At the millimeter-wave frequency, a circuit involving many
discrete components is usually very expensive and cumbersome. Also,
losses due to connectors are usually high.

A dielectric-based millimeter-wave integrated circuit, on the
other hand, usually consists of a common ground plane or a common
substrate on which the guiding structure and associated components
are located. The use of connectors in the circuit is strongly dis-
suaded. A prime consideration from the structrual viewpoint in a
millimeter-wave circuit is the adaptability of the guiding structure
for other circuit components. By appropriate manipulations of the
basic guiding structure, many components can be constructed cheaply and
efficiently. For the image guide, insular guide and inverted strip
guide, many of those components have been introduced. Applications,
such as dielectric resonators [36], directional couplers [37],[38],
ferrite isolators [39],[40], phase shifters [41], and leaky-wave
antennas [42],[48], have been published in the literature. Other
components in which the basic guiding structure has been modified
to perform a particular function are described in this section.

5.1   Cylindrical Dielectric Disc Resonators

Because of the unique arrangement of the dielectrics in a sus-
pended H-waveguide, a cylindrical disc resonator can be constructed as
described in Figure 53a. A circular dielectric disc of the same
height as of the dielectric core is sandwiched between two dielectric
insulating layers. Because of the metal enclosure, the dielectric
disc is locked securely in place and no bonding material is needed.
The dielectric constant of the disc can be different from that of the
guiding dielectric core allowing the use of high-permittivity materials
for high-Q applications.

The traditional techniques for analyzing the cylindrical dielec-
tric resonators have been based on the open-circuit boundary (magnetic
wall) model [44]. Simultaneous applications of the perfect and im-
perfect magnetic walls resulted in a better prediction of the resonant
frequency [45]. Konishi et al. [46] introduced a more complicated
method based on the variational procedure and predicted the resonant
frequencies within a 1 percent accuracy of the experimental data. Itoh
[47] applied the technique originally developed by Marcatili [18] for
analyzing the propagation constants of a rectangular dielectric wave-
guide to accurately predict the resonant frequencies of the $TE_{01\delta}^o$ mode.

The simple analytical technique described by Itoh is used here
to analyze the resonant structure shown in Figure 53a. To conform
to the waveguide parameters used in previous sections, the structure
adopted for analysis with familiar dimensional parameters is depicted
as Figure 53b. The dielectric constant of the disc is much higher

103

Ground Plane

Substrate ϵ_1

Substrate ϵ_3

Ground Plane

Dielectric Resonator ϵ_2

(a)

(b)

HP-284
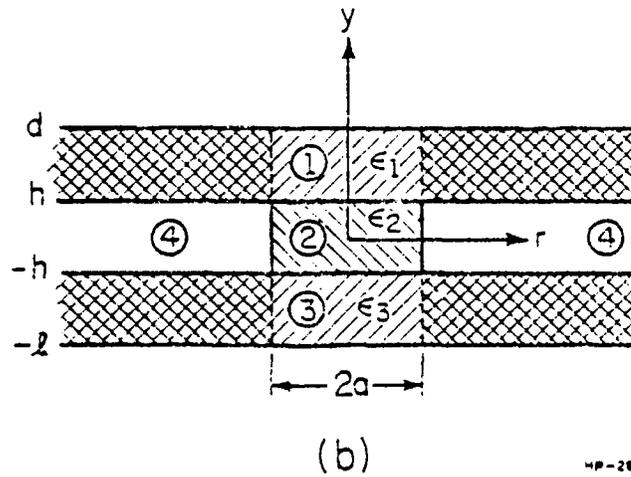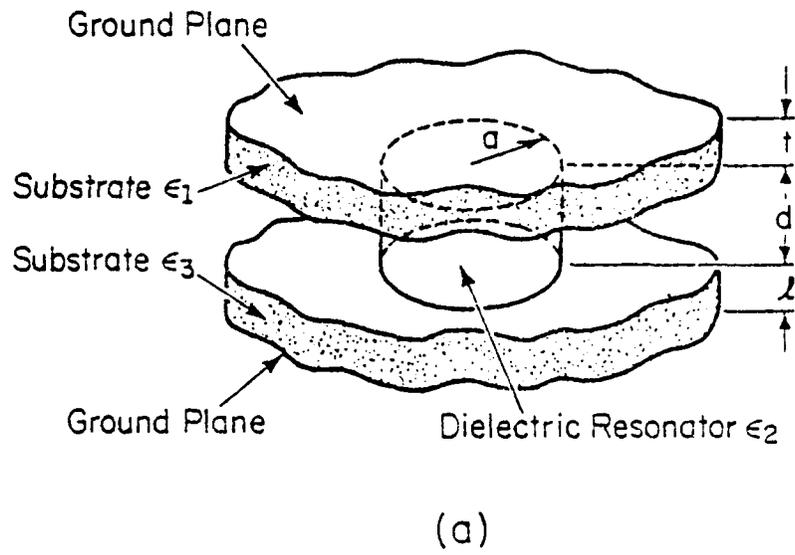
Figure 53. (a) Cylindrical dielectric disc resonator.
(b) Structure adopted for analysis.

than that of the dielectric insulating layers. When ε_1 and $\varepsilon_3 = 1$ and the substrate thicknesses t and l app ʳch infinity, the structure to be analyzed becomes the resonator in free-space in [44]-[46].

In a high Q resonator, most of the electromagnetic energy is stored in the disc (region 2) and decays exponentially in regions 1, 3 and 4. Much less energy is concentrated in the corner (or the shaded) regions. Consequently, only a very small error is introduced if the matching of the tangential fields is applied to the boundaries of region 2 only. The corner regions will be ignored entirely. Assuming no circumferential variation, the vector potential that has a single component in the y-direction can be written as

$$
\phi = \begin{cases}
A_1 \begin{cases} \sin\left[k_y^{(1)}(y-d)\right] \\ \cos\left[k_y^{(1)}(y-d)\right] \end{cases} J_0(k_{\rho i}r) & \text{region 1} & (42a) \\[2em]
\left(A_2 \sin\left[k_y^{(2)}y\right] + A_3 \cos\left[k_y^{(3)}y\right]\right) \begin{cases} J_0(k_{\rho i}r) & \text{region 2} & (42b) \\ K_0(k_{\rho o}r) & \text{region 4} & (42c) \end{cases} \\[2em]
A_4 \begin{cases} \sin\left[k_y^{(3)}(y+1)\right] \\ \cos\left[k_y^{(3)}(y+1)\right] \end{cases} J_0(k_{\rho i}r) & \text{region 3} & (42d)
\end{cases}
$$

where

$$\varepsilon_1 k_o^2 = k_y^{(1)2} + k_{\rho i}^2$$

$$\varepsilon_2 k_o^2 = k_y^{(2)} + k_{\rho i}^2$$

$$\tag{43}$$

$$\varepsilon_3 k_o^2 = k_y^{(3)} + k_{\rho i}^2$$

$$k_o^2 = k_y^{(2)} - k_{\rho o}^2$$

ϵ_1, i = 1,2,3, are the relative dielectric constants of the respective regions: $k_o = \omega_o\sqrt{\epsilon_o\mu_o}$ = free-space wavenumber; A_1, A_2, A_3 and A_4 are the unknown amplitude coefficients; and J_o and k_o are the Bessel and the modified Hankel function of the second kind of order zero, respectively. The upper line in the brackets in Eqs. (42a) and (42d) is for the TE^y mode while the lower line is for the TM^y mode. All field components can be derived from (42) [48]. With no circumferential variation, $E_y = E_\rho = H_\phi = 0$ for the TE mode, whereas $H_y = H_\rho = E_\phi = 0$ for the TM mode. By matching the tangential fields at r = a, $-h \le y \le h$ and at $y = \pm h$, $0 \le r \le a$, the following coupled characteristic equations are obtained.

TE^y mode:

$$k_{oo}K_o(k_{\rho o}a)\ J_1(k_{\rho i}a) + k_{\rho i}K_1(k_{\rho o}a)\ J_o(k_{\rho i}a) = 0 \qquad (44)$$

and

Equation (31)

TM^y mode:

$$\epsilon_2 k_{\rho o}K_o(k_{\rho o}a)\ J_1(k_{\rho i}a) + k_{\rho i}K_1(k_{oo}a)\ J_o(k_{\rho i}a) = 0 \qquad (45)$$

and

Equation (27)

The resonant frequencies of each mode are obtained by solving the respective set of two characteristic equations simultaneously. The mode designation for the TE and the TM modes are TE_{omn} and TM_{omn}, respectively. The first index is zero since there is no circumferential variation; the second index represents the order of the roots in

the radial direction; and the third index indicates the number of field maxima of the dominant electric field in the y-direction. For example, TE_{011} is the dominant mode instead of $TE_{01\delta}^o$ as described in Reference [46].

The resonant frequencies of the TE_{011} mode plotted as a function of the geometrical dimensions are shown in Figure 54. Figure 55 is a special case when the substrate's thickness approaches infinity and $\varepsilon_1, \varepsilon_3 = 1$. The numerical results predicted by the present method agree well with the experimental results published by Konishi et al. [46]. By comparing the resonant frequency curves in Figures 54 and 55, it is obvious that the removal of the dielectric substrates and the ground planes only causes a small change in the resonant frequencies of the structure. Since the dielectric constant of the dielectric cylindrical disc is much higher than that of the substrate, most of the energy is concentrated in the disc. In the substrate regions, the fields decay extremely fast. Consequently, the removal of the dielectric substrates has a minimal effect on the resonant frequences of the structure.

Figure 56 shows the curves of the resonant frequencies of the TM_{011} mode in a cylindrical disc resonator as a function of the geometrical dimensions for two different values of the dielectric constants of the disc (ε_2 = 35 and 88).

5.2 Dielectric Ring Resonators

This section describes two novel dielectric ring resonators that can be efficiently integrated into a dielectric-based MMW-IC to provide
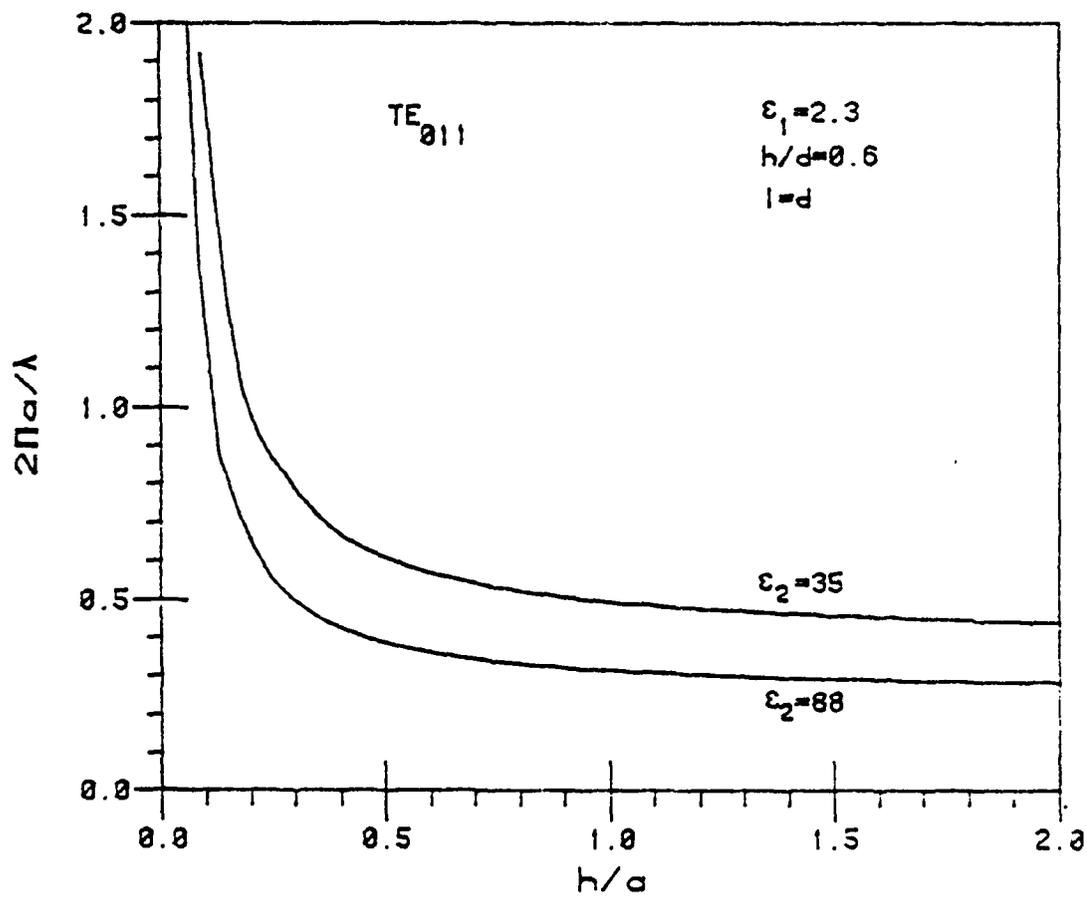
Figure 54. Resonant frequencies of the TE_{011} mode.

108
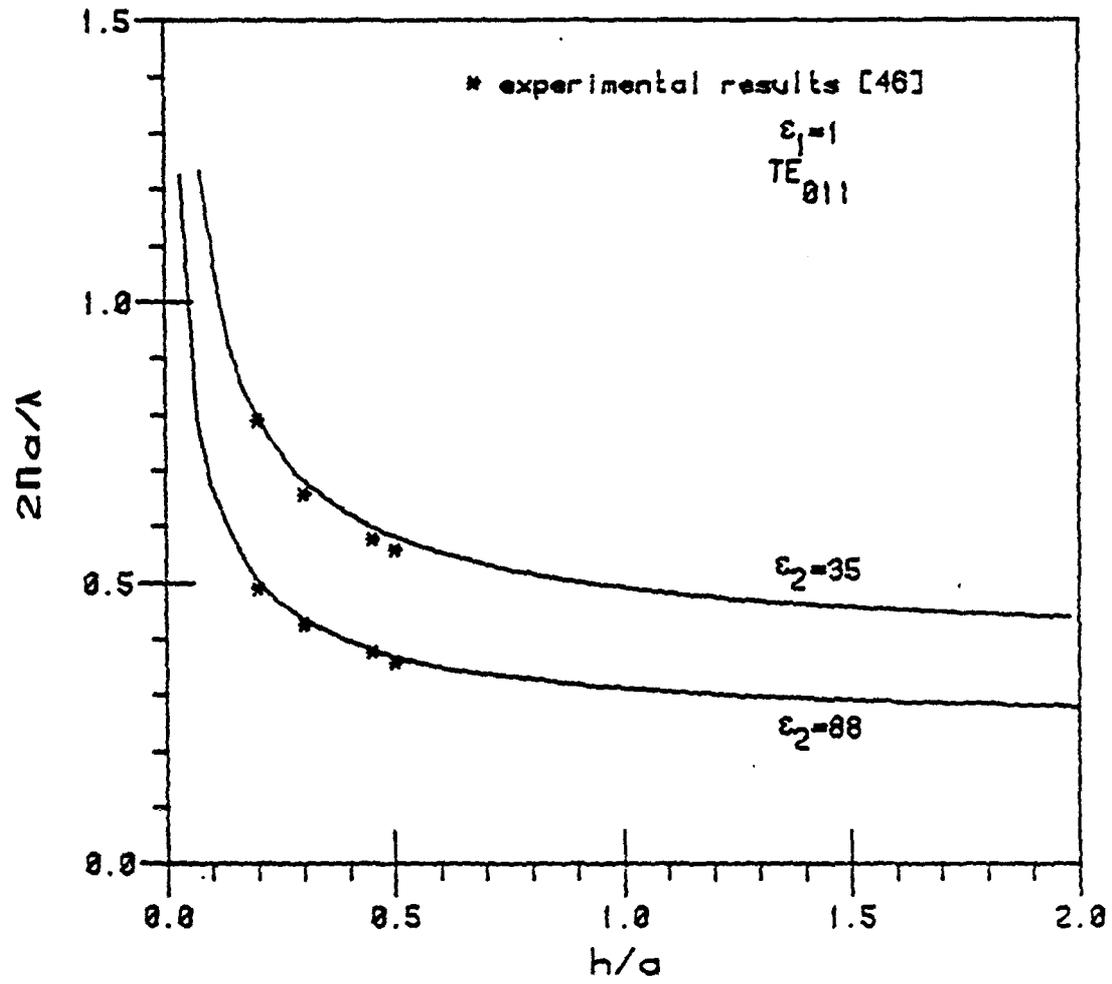
Figure 55. Resonant frequencies of the TE_{011} mode.

109
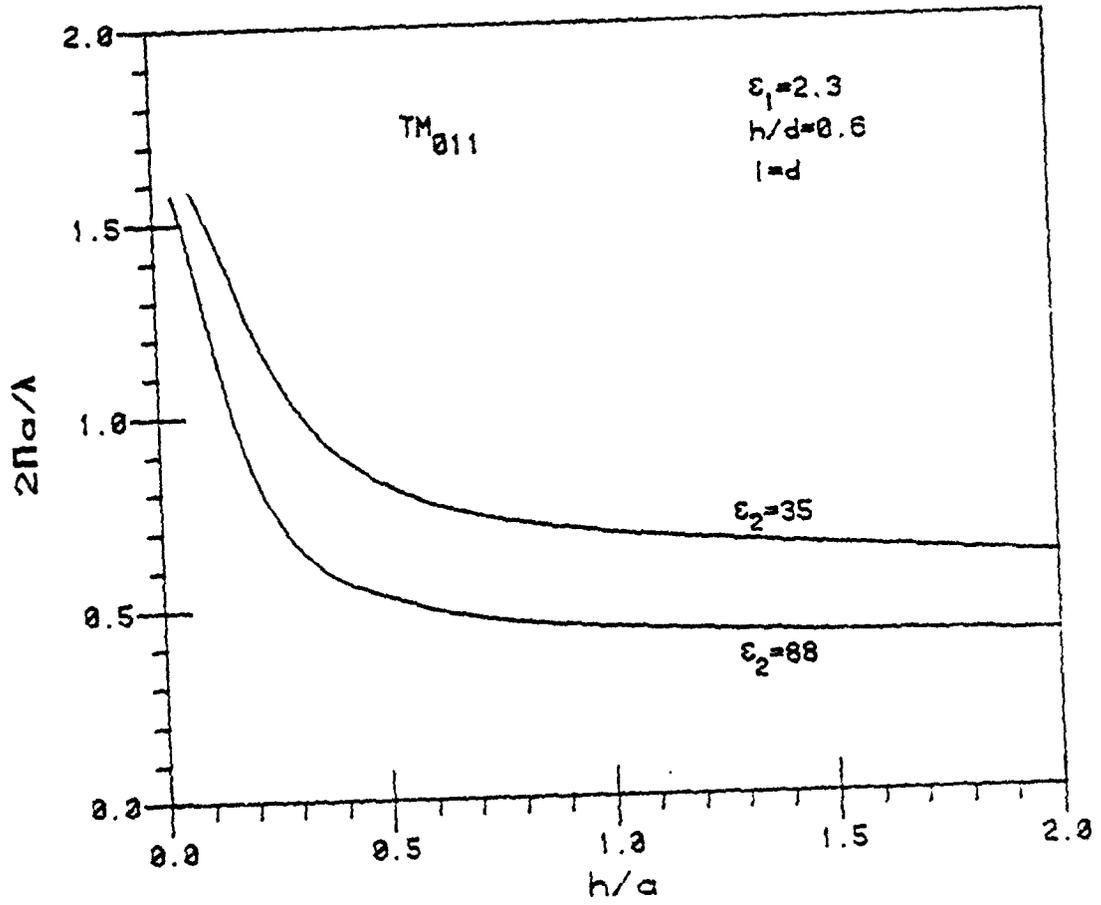
Figure 56. Resonant frequencies of the TM_{011} mode.

filtering effects. They are particularly useful in a system that employs the suspended H-waveguide as the guiding medium. Figures 57 and 58 show the top views of these resonators and the equivalent signal flow-graph schematics. The shaded regions in Figures 57a and 58a are the waveguide media, such as the dielectric core of a suspended H-waveguide. The metal side walls at ports 3 and 4 are short-circuit terminations. The resonant effect is due to the standing wave created by these terminations. The signal flow graph analysis [49] will be applied to the scattering equations to predict the frequency response of these resonators. The following assumptions are made in our formulations: (a) all guides have identical characteristic impedances, (b) the directional couplers have infinite directivity, and (c) the resonators are perfectly matched.

With these assumptions, the frequency responses of the resonator structure shown in Figure 57 can be approximated by the flow graph analysis as follows:

$$\left| S_{21} \right| = \left| \frac{t(1 - e^{-2\gamma \ell})}{1 - t^2 e^{-2\gamma \ell}} \right| \tag{46}$$

and

$$\left| S_{1'1} \right| = \left| \frac{c^2 e^{-\gamma \ell}}{1 - t^2 e^{-2\gamma \ell}} \right| \tag{47}$$

where t,c = transmission and coupling coefficients of the directional coupler

$\gamma = \alpha + jk_z$, complex propagation constant in the half-ring

ℓ = mean length of the half-ring (see Figure 57a).
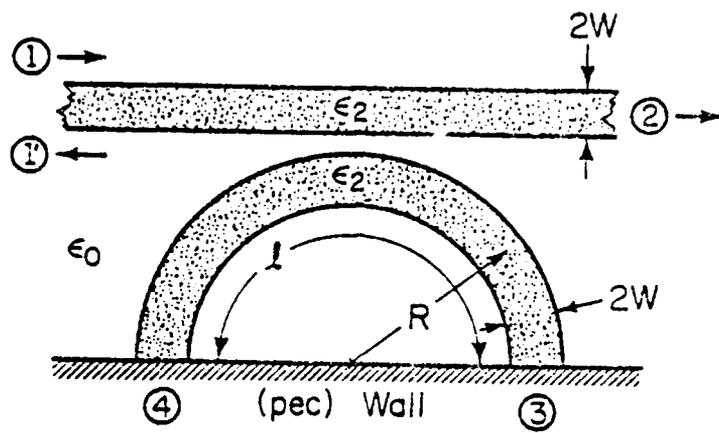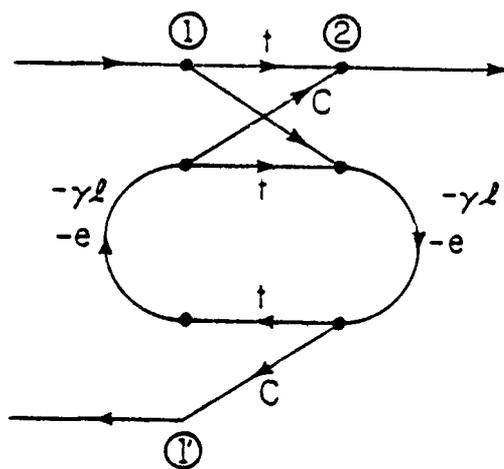
Figure 57. (a) Dielectric ring resonator.
           (b) Equivalent signal flow graph schematic.

112

(a)

(b)
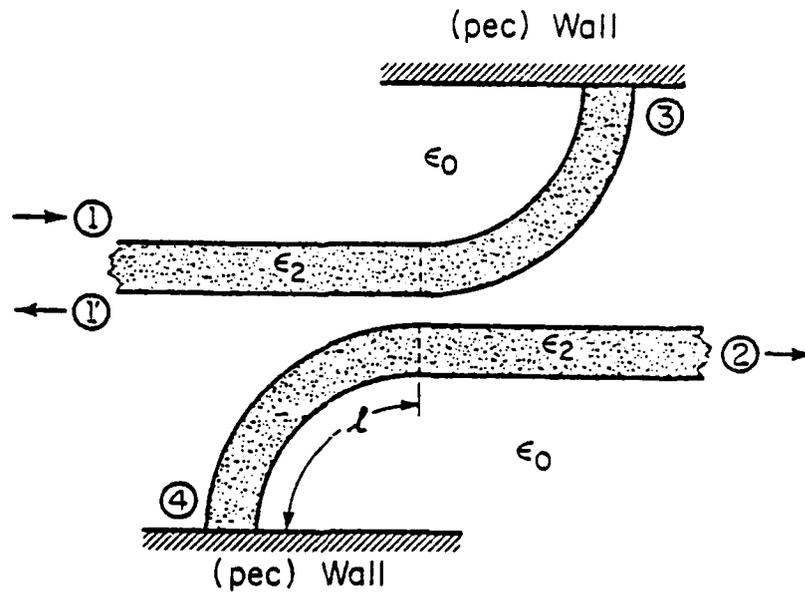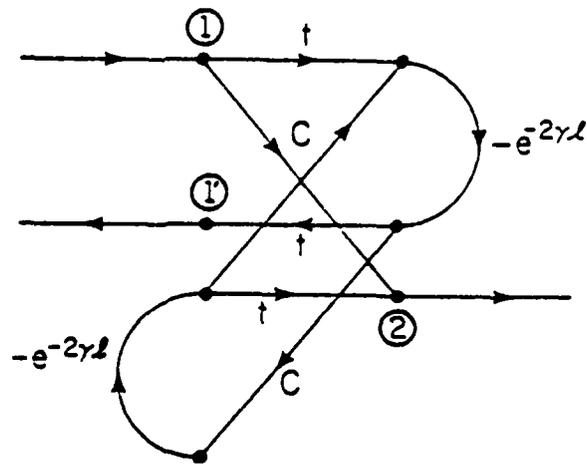
HP-280

Figure 58. (a) Dielectric ring resonator.
(b) Equivalent signal flow graph schematic.

k_z is approximated by the propagation constant of an uncoupled straight guide. α, which is the attenuation constant in the ring, is comprised of the dielectric loss, metal loss and radiation loss. These losses were discussed in Chapter 4. For a symmetric coupler, the transmission and coupling coefficients are given as [50],[51]

$$t = \cos\phi \; e^{-j\phi/2} \qquad\qquad\qquad (48)$$

$$c = j\sin\phi \; e^{-j\phi/2} \qquad\qquad\qquad (49)$$

where

$$\phi = \left(\frac{k_{z,even} - k_{z,odd}}{2}\right) \ell_c \qquad\qquad\qquad (50)$$

and ℓ_c is the effective coupling length. t and c can be calculated either by the mode-matching or the effective parameter techniques. For a nonsymmetric coupler, it is usually impossible to predict t and c. In this case, an effective coupling factor must be experimentally determined before the frequency response can be calculated. The resonant conditions of this filter occur when $|S_{21}| = 0$. From Eq. (46), this corresponds to

$$\ell \approx n \frac{\lambda_g}{2} \qquad , \qquad n = 1,2,\ldots \qquad\qquad\qquad (51)$$

where λ_g is the waveguide wavelength at the resonant frequency.

The filter shown in Figure 58a is also analyzed by the signal flow graph technique. From Figure 58b, the scattering parameters for this structure can be derived as

$$|S_{21}| = \left| \frac{c(1+e^{-4\gamma\ell})}{1 - c^2 e^{-4\gamma\ell}} \right| \tag{52}$$

$$|S_{1'1}| = \left| \frac{t^2 e^{-2\gamma\ell}}{1 - c^2 e^{-4\gamma\ell}} \right| \tag{53}$$

where ℓ is the length of the curved section on each arm of the resonator (see Figure 58a). At resonance, $|S_{21}| = 0$, which corresponds to

$$\ell \approx \frac{1}{4}\left(n + \frac{1}{2}\right)\lambda_g \quad , \quad n = 1,2,\dots \tag{54}$$

For both resonator configurations, a quick glance at the frequency response expressions reveals that S_{21} has the characteristics of a band-reject filter, while $S_{1'1}$ behaves like a band-pass filter. With an additional directional coupler at the input port, these resonators can be used either as a band-pass or as a band-reject filter.

5.3 Suspended H-Waveguide Leaky-Wave Antennas

Another possible application of the suspended H-waveguide is the leaky-wave antenna. The waveguide structure can be converted into a leaky-wave antenna (or a periodic band-reject filter) by edging periodic narrow slots on the top metal surface along the propagation direction. The geometry of the leaky-wave antenna is shown in Figure 59a. This antenna is frequency scannable simply by varying the operating frequency, and can be flush-mounted. Since a complete investigation of this antenna is beyond the scope of this thesis,

115

(a)

(b)
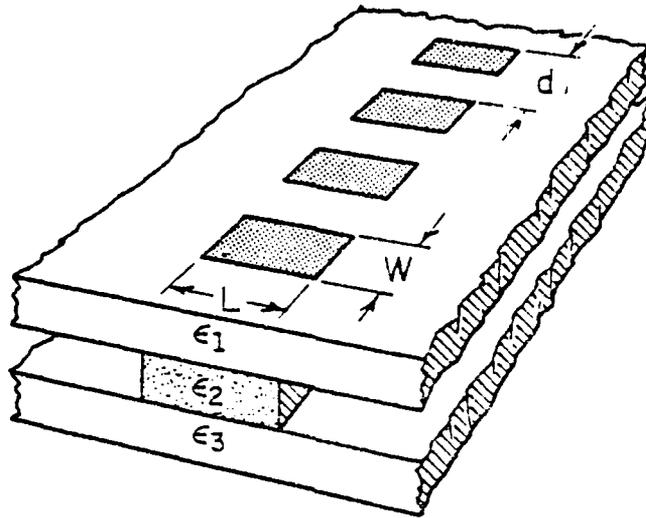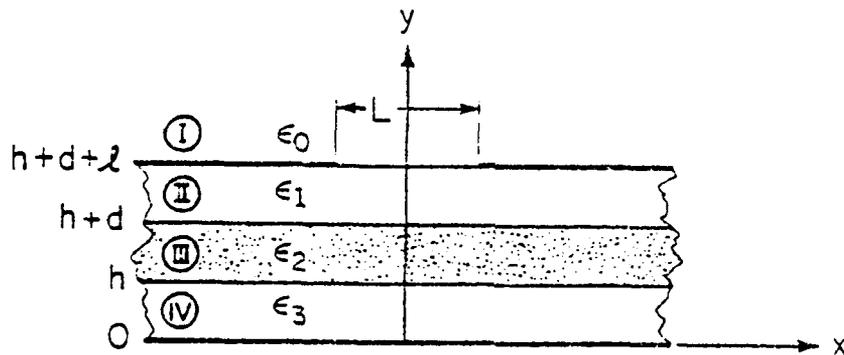
HP-282

Figure 59. (a) Leaky-wave antenna.
(b) Structure adopted for analysis.

116

only the formulation of the eigenvalue problem for finding the complex propagation constants in the structure is presented.

The analysis is based on the spectral domain approach in which the Galerkin's procedure is applied in the Fourier transform domain. A dual formulation for an image guide leaky-wave antenna and a band-reject filter has been published recently [52],[53].

As a first step to solve this problem, the dielectric core is transformed into an infinite slab in the x-direction via the effective parameter technique described in detail in Section 2.2. The cross section to be analyzed is shown in Figure 59b. Only the LSM^y mode will be considered here even though the same procedure can be applied to the LSE^y mode.

Because of the periodicity of the structure, the vector potential and all field components must consist of all space harmonic terms. For the LSM^y mode, the Hertzian potential and the field components of interest are

$$\bar{\pi}^e = \hat{y} \sum_{n=-\infty}^{\infty} \phi_n(x,y) \exp(-jk_{zn}z) \tag{55}$$

$$E_z \sim \frac{\partial}{\partial z}\frac{\partial}{\partial y} \sum_{n=-\infty}^{\infty} \phi_n(x,y) \exp(-jk_{zn}z) \tag{56}$$

$$H_x \sim \varepsilon_i \sum_{n=-\infty}^{\infty} \phi_n(x,y) \exp(-jk_{zn}z) \tag{57}$$

where k_{zn} is the propagation constant of the n-th space harmonic and is related to that of the fundamental mode by

$$k_{zn} = k_z - j\alpha + \frac{2\pi n}{d} , \quad n = 0,\pm1,\pm2\cdots \tag{58}$$

where k_z is the propagation constant of the fundamental mode, α is the attenuation constant of the structure, and d is the periodic slot spacing. It should be mentioned that the propagation constant of the n-th harmonic is different from other harmonics, but the attenuation constant is the same for all harmonics.

In the spectral domain, the potential as well as the field components are Fourier transformed via

$$\tilde{\phi}_n(k_x,y) = \int_{-\infty}^{\infty} \phi_n(x,y) \, \exp(jk_x x) \, dx \tag{59}$$

where $\tilde{\phi}_n$ satisfied

$$\left\{ \frac{d^2}{dy^2} - \eta^{(i)^2} \right\} \tilde{\phi}_n(k_{x,y}) = 0 \quad , \quad i = 1,2,3,4 \tag{60}$$

From now on, the symbol $\sim$ will be understood as being the Fourier transform of the quantity without it.

The appropriate solutions for the above differential equation are:

$$\phi_n^{(1)} = \tilde{A}_n \, \exp(\eta^{(1)}(y-h-d-1)) \qquad , \; y \geq h+d+1 \tag{61a}$$

$$\phi_n^{(2)} = \tilde{B}_n \, \sinh(\eta^{(2)}(y-h-d)) + \tilde{C}_n \, \cosh(\eta^{(2)}(y-h-d-)), \; h+d \leq y \leq h+d-1 \tag{61b}$$

$$\phi_n^{(3)} = \tilde{D}_n \, \sinh(\eta^{(3)}(y-h)) + \tilde{E}_n \, \cosh(\eta^{(3)}(y-h)) \qquad , \; h \leq y \leq h+d \tag{61c}$$

$$\phi_n^{(4)} = \tilde{F}_n \, \cosh(\eta^{(4)}y) \qquad , \; 0 \leq y \leq h \tag{61d}$$

where

$$\eta^{(1)^2} = k_x^2 + k_{zn}^2 - k_o^2$$

$$\eta^{(2)^2} = k_x^2 + k_{zn}^2 - \varepsilon_1 k_o^2 \tag{62}$$

$$\eta^{(3)^2} = k_x^2 + k_{zn}^2 - \mu^* \varepsilon_2 k_o^2$$

$$\eta^{(4)^2} = k_x^2 + k_{zn}^2 - \varepsilon_3 k_o^2$$

In (64), μ^* is the effective permeability of the TM^y mode in region 2. $\tilde{A}_n, \ldots, \tilde{F}_n$ are the n-th harmonics of the transformed potential in each region. Since the boundary conditions with respect to the x-coordinates are defined for all x's in the space domain, they will be defined for all k_x's in the transform domain, i.e.,

$$\text{at } y = h \quad : \quad \tilde{H}_x^{(4)} = \tilde{H}_x^{(3)} \tag{63a}$$

$$\tilde{E}_z^{(4)} = \tilde{E}_z^{(3)} \tag{63b}$$

$$\text{at } y = h+d \quad : \quad \tilde{H}_x^{(3)} = \tilde{H}_x^{(2)} \tag{64a}$$

$$\tilde{E}_z^{(3)} = \tilde{E}_z^{(2)} \tag{64b}$$

$$\text{at } y = h+d+l \quad : \quad \tilde{E}_z^{(2)} = \tilde{E}_z^{(1)} = \tilde{E}_z(k_x) \tag{65a}$$

$$\tilde{H}_x^{(1)} - \tilde{H}_x^{(2)} = \tilde{J}_z(k_x) \tag{65b}$$

where $\tilde{E}_z(k_x)$ and $\tilde{J}_z(k_x)$ are the Fourier transforms of the unknown tangential electric field $E_z(x)$ in the slots and the unknown current $J_z(x)$ on the metal portion, respectively, i.e.,

$$E_z(k_x) = \int_{-L/2}^{L/2} E_z(x) \, \exp(jk_x x) \, dx \tag{66}$$

The z-dependence is not affected by the Fourier transform and has been excluded to obtain simplified expressions. Since $\tilde{E}_z(k_x)$ is periodic, we have [54]

$$\tilde{E}_z(k_x, z) = \sum_{n=-\infty}^{\infty} \tilde{E}_{z,n}(k_x) \exp(-jk_{zn}z) \tag{67}$$

or

$$\tilde{E}_{z,n}(k_x) = \frac{1}{d} \int_0^W \tilde{E}_z(k_x, z) \exp(jk_{zn}z) \, dz \tag{68}$$

W is the width of each slot and $\tilde{E}_{zn}$ are the space harmonics of the surface slot field $\tilde{E}_z$. Using (67) and the boundary conditions (63a)-(65a), the unknown harmonic amplitudes can be expressed in terms of space harmonic $\tilde{E}_{z,n}(k_x)$. Finally, the last boundary condition (65b) is enforced to obtain the following expression for $\tilde{J}_z$.

$$\tilde{J}_z(k_x) = \sum_{n=-\infty}^{\infty} \tilde{G}_n(k_x, k_{zn}) \tilde{E}_{z,n}(k_x, k_{zn}) \exp(-jk_{zn}z) \tag{69}$$

where the

$$\tilde{G}_n(k_{xn}, k_{zn}) = \frac{1}{k_{zn}\eta^{(1)}} \left\{ 1 - \frac{\varepsilon_1\eta^{(1)}[P_1\sinh(\eta^{(2)}\ell) + P_2\cosh(\eta^{(2)}\ell)]}{\eta^{(2)}[\cosh(\eta^{(2)}\ell)\,P_1 + \sinh(\eta^{(2)}\ell)\,P_2]} \right\}$$

and

$$P_1 = \varepsilon_1\left\{ \varepsilon_2\eta^{(4)}\cosh(\eta^{(3)}d)\sinh(\eta^{(4)}h) + \varepsilon_3\eta^{(2)}\sinh(\eta^{(3)}d)\cosh(\eta^{(4)}h) \right\}$$

$$P_2 = \eta^{(2)}\left\{ \varepsilon_2^2\frac{\eta^{(4)}}{\eta^{(3)}}\sinh(\eta^{(3)}d)\sinh(\eta^{(3)}h) + \varepsilon_2\varepsilon_3\cosh(\eta^{(3)}d)\cosh(\eta^{(4)}h) \right\}$$

Before applying the Galerkin's procedure, the unknown $\tilde{E}_z(k_x)$ is expanded in terms of known basis functions, i.e.,

$$\tilde{E}_z(k_x, z) = \sum_{m=1}^{M} a_m \tilde{E}_{z,m}(k_x, z) \tag{70}$$

where a_m is the unknown constant, and the basis functions must be chosen such that in the space domain they are non-zero only in the slots. For the LSM^y mode, the basis functions can be chosen as

120

$$E_{z,m}(x,z) = \cos\left[\frac{(2m-1)\pi}{L}\,x\right]\,\cos\left[\frac{2(m-1)\pi}{W}\,z\right]\;,\quad m=1,2,\ldots$$

$$-\frac{L}{2}\le x\le\frac{L}{2}\quad\text{and}\quad-\frac{W}{2}\le z\le\frac{W}{2} \tag{71}$$

From (68), (69) and (70), the transform of the unknown current becomes:

$$\tilde{J}_z(k_x,z) = \sum_{n=-\infty}^{\infty}\sum_{m=1}^{M} a_m \tilde{G}_n(k_x,k_{zn})\,\tilde{E}_{z,m,n}(k_x,k_{zn})\,\exp(-jk_{zn}z)$$

$$= \sum_{n=-\infty}^{\infty}\tilde{J}_n(k_x,z)\,\exp(-jk_{zn}z) \tag{72}$$

where $\tilde{E}_{z,m,n}$ and $\tilde{J}_n$ are the amplitude coefficients of the n-th space harmonic of $\tilde{E}_{z,m}(k_x,z)$ and $\tilde{J}_z(k_x,z)$, respectively. $\tilde{E}_{z,m,n}$ is given by

$$\tilde{E}_{z,m,n}(k_x,k_{zn}) = \frac{1}{d}\int_0^W \tilde{E}_{z,m}(k_x,z)\,\exp(jk_{zn}z)\,dz$$

$$\simeq (2m-1)\,k_{zn}\,\frac{\cos(k_xL/2)}{(k_xL)^2-((2m-1)\pi)^2}\,\frac{\sin(k_{zn}W/2)}{(k_{zn}W)^2-(2(m-1)\pi)^2} \tag{73}$$

Now, over a unit cell, the Galerkin's procedure is applied by taking the inner product of $\tilde{J}_z$ and $\tilde{E}_{z,s}^{*}$ for different values of s and sum over all n. The following matrix equation is obtained.

$$\sum_{m=1}^{M}\left\{\sum_{n=-\infty}^{\infty}\int_{-\infty}^{\infty}\tilde{G}_n(k_x,k_{zn})\,\tilde{E}_{z,m,n}(k_x,k_{zn})\,\tilde{E}_{z,s,m}(k_x,k_{zn})\,dk_x\right\}a_m = 0\;,$$

$$s = 1,2,\ldots M \tag{74}$$

The fact that the left-hand side equals zero comes directly from the Parseval's theorem, since in the space domain, J_z and E_z are zero in the

complementary regions. A nontrivial solution for a_m exists only if
the determinant of (74) equals zero which is also the eigenvalue
equation that determines the phase constant of the dominant space
harmonic. If only one term of the slot field distribution is taken
into account, the complex propagation constant is then obtained from
the following eigenvalue equation.

$$\sum_{n=-\infty}^{\infty} \int_{-\infty}^{\infty} \tilde{G}_n(k_x, k_{zn}) \left| \tilde{E}_{z,1,n}(k_x, k_{zn}) \right|^2 dk_x = 0 \tag{75}$$

The solution for the complex propagation constant of the funda-
mental mode can be obtained by a numerical procedure which searches
the roots of (74) within some numerical tolerance [52]. Since all con-
stituents of (74) and (75) are symmetric with respect to real k_x, the
integration need be carried out only along half of the k_x axis. More-
over, according to Reference 52, there appears to be little or no
contribution to the expression beyond a certain value of k_x, and the
integration can be truncated accordingly. The range of 'n' in these
expressions can be as small as 2 [52].

The real part of the propagation constant controls the main beam
direction while the attenuation constant α determines the beamwidth
and aperture efficiency. It accounts for the radiation loss and is
strongly influenced by the size of the slots. Since the amplitude ratio
of each element in the slot arrays is determined by α, the radiation
pattern in the plane that contains the longitudinal axis of the
antenna can be computed readily. The radiation pattern in the trans-
verse plane can be approximated by that of a slot antenna. The

angular direction of the leaky beam measured from broadside in the y-z plane is approximated by

$$\theta_n = \sin^{-1}(Re(k_{zn}/k_o)) \tag{76}$$

This equation can be used as a tool to determine the relationship between the main beam direction and the periodic spacing d of the slot. For antenna applications, the structure's parameters are usually designed such that only the n = -1 space harmonic will radiate.

5.4   Horn Dielectric-Filled Leaky-Wave Antennas

The antenna described in this section is designed for integration with the millimeter-wave circuits that employ the image guide or the trapped image guide as the guiding medium. In this structure, the dielectric guide with periodic perturbations on top is embedded in a rectangular trough with metal flare attached along each side as shown in Figure 60. With this arrangement, the antenna behaves like a linear array in the longitudinal (or E-) plane which is the plane containing the longitudinal axis of the antenna. In the transverse (or H-) plane, the radiation pattern resembles that of a horn. Unlike the periodic slots of the antenna described in the previous section, the periodic perturbations in this antenna structure are metallic strips which are painted directly on the dielectric guide. These perturbations cause the guided-wave energy to radiate off the dielectric guiding structure. Each of the strips behaves like an element of a linear array. A complete discussion of this antenna structure can be found in Reference [26]. Some excerpts from that reference are presented here.

123
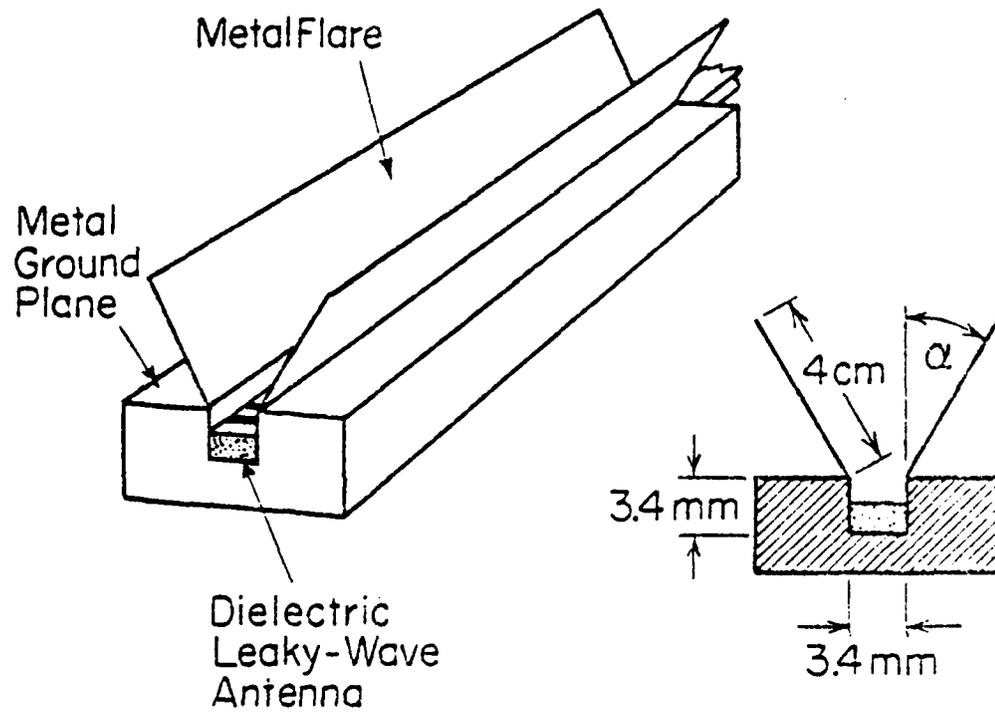
Figure 60. Horn dielectric-filled trough leaky-wave antenna.

124

At each strip, it is desirable that the rate of energy radiated be small. Thus, a portion of the guided-wave energy will propagate through the entire antenna length, which implies a larger aperture. But equally important, the guided energy should be completely radiated by these strips so that there is no energy left at the antenna truncation which would radiate endfire. Experiments show that the rate of energy radiated along the dielectric leaky-wave antenna structure is strongly influenced by the width of the perturbation strips on the top surface of the dielectric guide.

For very narrow strip widths, the radiation from each element is so small that a very long antenna has to be constructed to radiate all energy in an effective manner. On the other hand, if the metal strips are too wide (>0.5 λ_g), the bulk of radiated energy is produced by the first few strips and, consequently, the effective aperature is very small. Also, for large strip widths, the sidelobes are very high, due probably to the large mismatch at the first strip.

It is well-known that if the attenuation rate of the traveling wave in the z-direction due to the energy leakage at the leaky-wave region of the antenna is a constant (neper/m), the radiation pattern is not symmetric about the main beam direction. Therefore, the energy transfer from the leaky beam to the surface wave, and vice versa, is not optimum [55]. A suitable modification of the geometry in the leaky-wave region of the antenna should be made to obtain a slowly varying leaky rate to increase the conversion efficiency [56]. If the variation of the strip width is correct, all the surface energy

will convert into a symmetric leaky beam (and vice versa). This can

be done by tapering the size of the periodic scatterers [55] as

shown in Figure 61. Since the mechanisms of perturbation and radiation

are not clear, only the widths of these metallic strips were experimentally

investigated. The width of the m-th strip is found from the

following empirical relation:

$$W_m = \begin{cases} (0.15 + 0.015(m-1)) \; \lambda_g, & m \leq 18 \\ \\ 0.4 \; \lambda_g, & m > 18 \end{cases} \qquad (77)$$

where λ_g is the guided wavelength. For slight perturbation, the real

part of the propagation constant of the structure is approximated by

that of an unperturbed structure.

For periodic strip spacing, the angular direction θ_n' of the leaky-

wave beam measured from broadside is approximated by Eq. (76), which

for clarity, is given again as

$$\theta_n' = \sin^{-1}(\lambda_o/\lambda_g + n\lambda_o/d) \qquad (78)$$

where d is the perturbation spacing between the centers of two adjacent

strips, λ_o is the free-space wavelength, and n is the index of the

space harmonic $(0, \pm 1, \pm 2, \ldots)$. For the antenna applications, the structure's

parameters are usually designed so that only the n = -1 space harmonic

will radiate, and all the energy will be radiated through this harmonic.

The antenna is frequency scannable if $|\lambda_o/\lambda_g + n\lambda_o/d| < 1$. For a broadside

array, d should be made equal to the guided wavelength λ_g. Figure 62

126
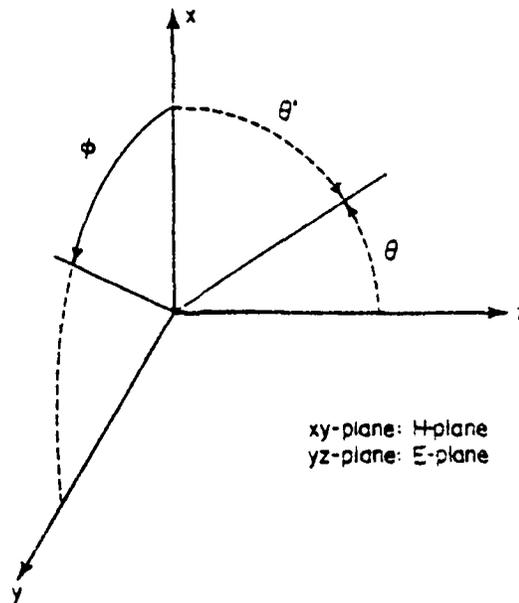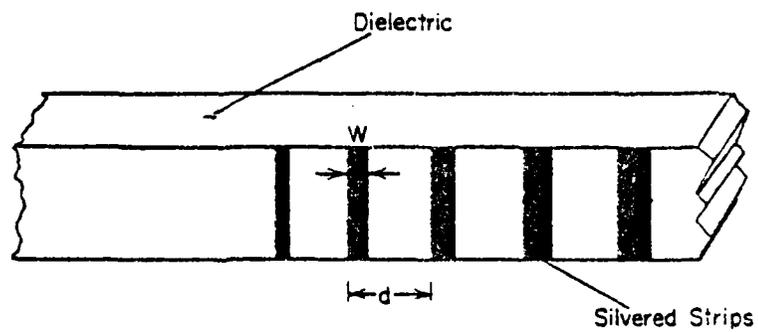
Figure 61. Tapering the width of the metallic strips and the
coordinate system.

127
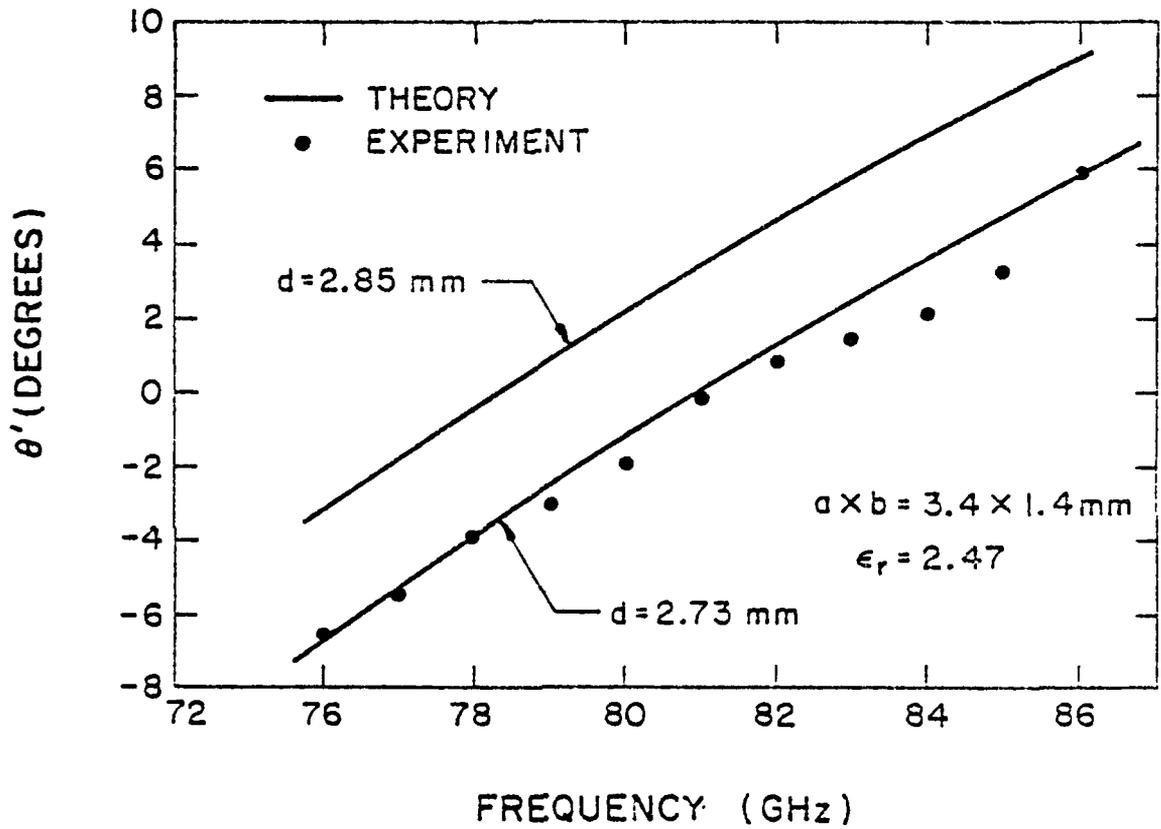
Figure 62. Computed and measured main beam directions.

shows the measured and computed main beam directions as a function of the frequency. The entire angular scanning range can be shifted more positively or negatively by changing the perturbation spacing between the adjacent strips.

In the transverse (or H-) plane, the metal flares are attached to both sides of the trough to improve the radiation characteristics in this plane. With H_x as the major magnetic field component in the dielectric guide, the current element on each metal strip is z-oriented, and the principal aperture field of the metal flares is E_z. Assuming the structure is infinitely long in the z-direction allows the metal flares to be modeled as an H-plane sectoral horn [57],[58].

The dielectric guide was designed to fit snugly against the side walls of the metal trough thus eliminating the need for adhesive materials which were used to bond the dielectric guide to the ground plane. The depth of the trough is such that the propagation constant of the structure can be determined using the dielectric-loaded trough guide model. The height of the dielectric guide is then chosen to provide single-mode operation. Under these guidelines and constraints, a dielectric waveguide of dimensions 3.4 x 1.4 mm was constructed. The trough depth was arbitrarily chosen to be 3.4 mm to simplify the construction. It was observed that as long as the trough was not too shallow, the radiation patterns of the structure were almost independent of the trough depth. The length of the flare horn was chosen to be 4 cm. Figure 63 shows the comparison between the measured relative gain of the constructed antenna as a function of the flare angle
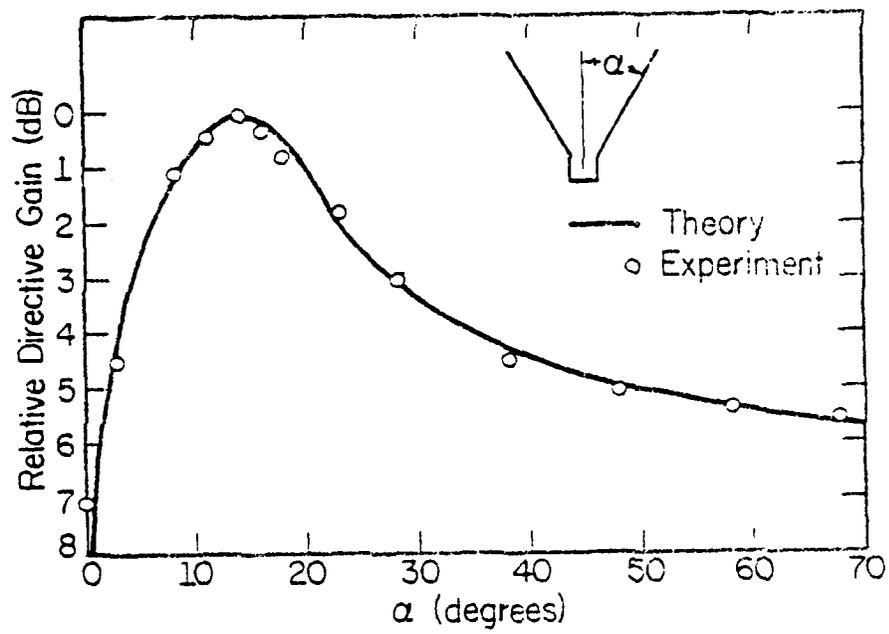
Figure 63. Relative gains of the constructed antenna and an H-plane sectoral horn versus flare angle.

130

and that of an H-plane sectoral horn. The results of this figure have
confirmed the assumption that the H-plane sectoral horn is a reason-
able model to predict the flare angle for maximum gain in the H-plane.
For the strip width distribution chosen according to (77) and the flare
angle selected from Figure 63 for maximum gain, the radiation patterns
in both the E- and H-planes of the horn dielectric-filled trough leaky-
wave antenna were measured and plotted in Figure 64. The number of
the silver strips on top of the dielectric guide was 32. The half-
power beamwidths (HPBW) in the E- and H-planes are 4°, 13°, respectively.

The antenna was designed for broadside radiation. The consequent
experimental beam angle deviated slightly from the normal direction.
This is interesting since the strip width determines the rate of energy
radiated off the guide but does not change the angle of radiation
significantly. The overall gain of the antenna is the product of the
gains in the E- and H-planes and was measured to be 26 dB. The side-
lobe levels were at least 25 dB below the main lobe. Since there is
no endfire radiation detected, it is assumed that most of the radiated
energy is produced by the strip elements.

The main beam level of the antenna is relatively stable through-
out the operating frequency range except at around 84 GHz where it
falls about 2 dB below the reference level (see Figure 65).

131
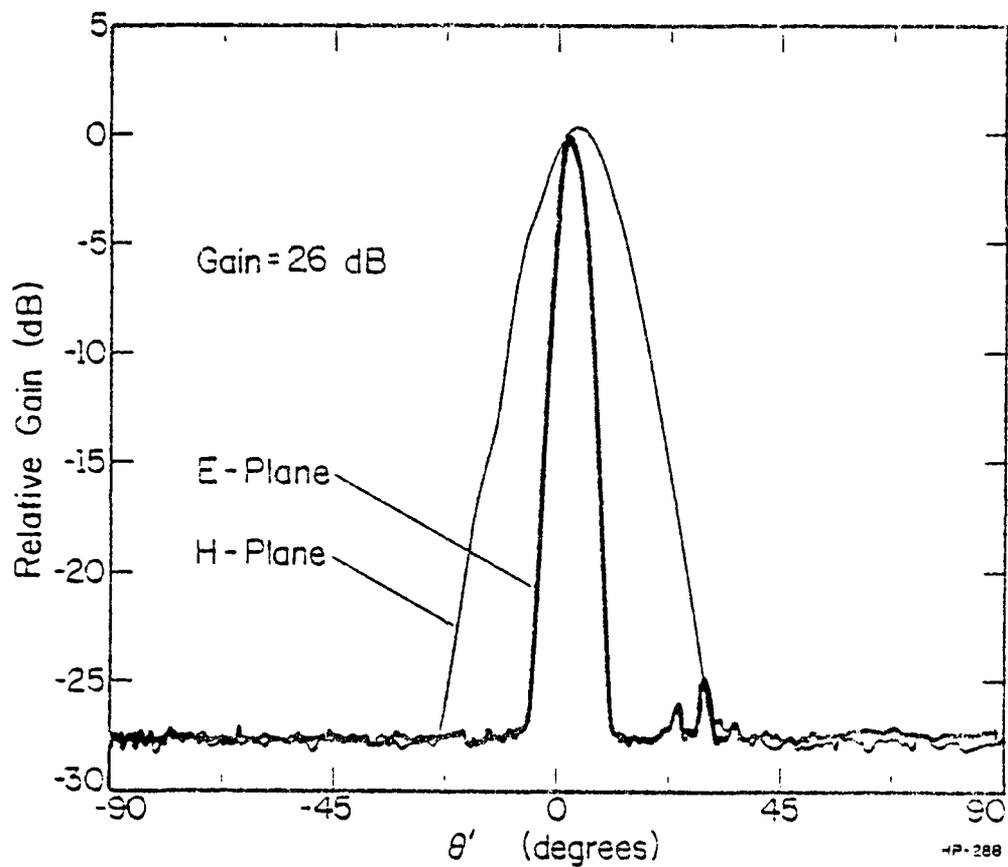
Figure 64. Radiation patterns in the E- and H-planes of the constructed antenna.
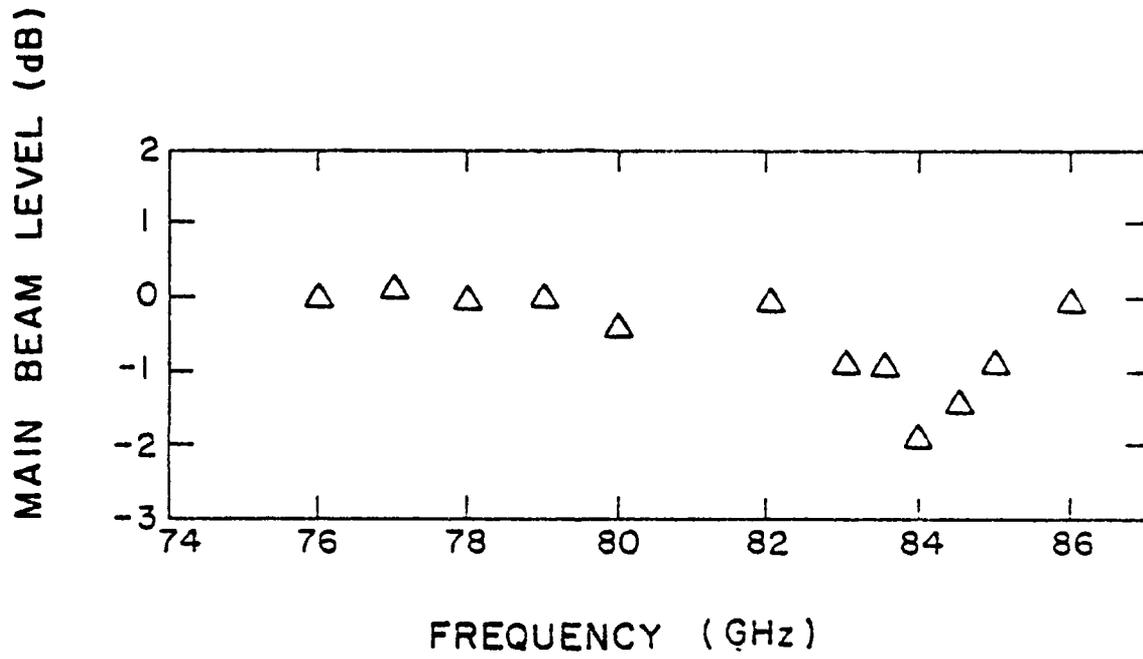
Figure 65. Main beam level versus frequency.

6. CONCLUSIONS

In this thesis, the field and propagation characteristics of many dielectric waveguide structures have been analyzed. Both the mode matching and the effective parameter techniques described in this thesis are very general and can be applied directly to many planar dielectric waveguide structures of rectangular cross section. The theoretical and experimental results agree well throughout. A new dielectric waveguide configuration--the suspended H-waveguide--has been introduced along with a detailed loss analysis. The overall low-loss figure and a superior structural layout of this waveguide promise wider applications in the millimeter-wave integrated circuits. Some essential integrable components, such as dielectric resonators and leaky-wave antennas, have been studied. A theoretical formulation of the eigenvalue equation based on the spectral domain approach for determining the propagation constant of a periodic slot waveguide array has also been presented.

APPENDIX A

MATCHING OF TANGENTIAL FIELD COMPONENTS AT $y = \pm h$

Eight equations resulting from matching the tangential field components E_x, H_x, E_z, and H_z at the planes $y = \pm h$ are

$$\sum_{n=0}^{N} \left(\varepsilon_1 k_o^2 - k_{xn}^{(1)^2} \right) \left\{ \begin{array}{c} \cos\left(k_{xn}^{(1)}(x+a) \right) \\ \sin\left(k_{xn}^{(1)}(x+a) \right) \end{array} \right\} A_n = \sum_{n=1}^{N'} \left(\varepsilon_i k_o^2 - k_{xn}^{(i)^2} \right)$$

$$\cdot \; \phi_{e,n}^{(i)}(x)(I_n + I_n') \tag{A-1}$$

$$\sum_{m=0}^{M} \left(\varepsilon_1 k_o^2 - \tilde{k}_{xm}^{(1)^2} \right) \left\{ \begin{array}{c} \sin\left(\tilde{k}_{xm}^{(1)}(x+a) \right) \\ \cos\left(\tilde{k}_{xm}^{(1)}(x+a) \right) \end{array} \right\} B_m = \sum_{m=1}^{M'} \left(\varepsilon_i k_o^2 - \tilde{k}_{xm}^{(i)^2} \right)$$

$$\cdot \; \tilde{\phi}_{h,m}^{(i)}(x)(J_m + J_m') \tag{A-2}$$

$$\sum_{n=0}^{N} k_z k_{xn}^{(1)} \left\{ \begin{array}{c} -\sin\left(k_{xn}^{(1)}(x+a) \right) \\ \cos\left(k_{xn}^{(1)}(x+a) \right) \end{array} \right\} A_n + \sum_{m=0}^{M} \omega\mu_o \; \tilde{k}_{ym}^{(1)} \left\{ \begin{array}{c} \sin\left(\tilde{k}_{xm}^{(1)}(x+a) \right) \\ \cos\left(\tilde{k}_{xm}^{(1)}(x+a) \right) \end{array} \right\}$$

$$\cdot \; \tan\left(\tilde{k}_{ym}^{(1)}(h-d) \right) B_m = \sum_{n=1}^{N'} k_z \frac{\partial \phi_{e,n}^{(i)}(x)}{\partial x} (I_n + I_n')$$

$$- \sum_{m=1}^{M'} \omega\mu_o \; \tilde{k}_{ym} \; \tilde{\phi}_{h,m}^{(i)}(x) \left(-\tan(\tilde{k}_{ym}h) \; J_m + \cot(\tilde{k}_{ym}h) \; J_m' \right) \tag{A-3}$$

$$\sum_{n=0}^{N} \omega\varepsilon_o\varepsilon_1 k_{yn}^{(1)} \begin{Bmatrix} \cos\left[k_{xn}^{(1)}(x+a)\right] \\ \sin\left[k_{xn}^{(1)}(x+a)\right] \end{Bmatrix} \cot\left[k_{yn}^{(1)}(h-d)\right] A_n$$

$$+ \sum_{m=0}^{M} k_z \tilde{k}_{xm}^{(1)} \begin{Bmatrix} \cos\left[\tilde{k}_{xm}^{(1)}(x+a)\right] \\ -\sin\left[\tilde{k}_{xm}^{(1)}(x+a)\right] \end{Bmatrix} B_m = \sum_{n=1}^{N'} \omega\varepsilon_o\varepsilon_i k_{yn} \phi_{e,n}^{(i)}(x)$$

$$\cdot \left(\cot(k_{yn}h)\ I_n - \tan(k_{yn}h)\ I_n'\right) + \sum_{m=1}^{M'} k_z \frac{\partial\tilde{\phi}_{h,m}^{(i)}(x)}{\partial x}\ (J_m + J_m')$$

$$(A-4)$$

$$\sum_{n=0}^{N} \left(\varepsilon_3 k_o^2 - k_{xn}^{(3)^2}\right) \begin{Bmatrix} \cos\left[k_{xn}^{(3)}(x+a)\right] \\ \sin\left[k_{xn}^{(3)}(x+a)\right] \end{Bmatrix} K_n$$

$$= \sum_{n=1}^{N'} \left(\varepsilon_i k_o^2 - k_{xn}^{(i)^2}\right) \phi_{e,n}^{(i)}(x)(-I_n + I_n') \qquad (A-5)$$

$$\sum_{m=0}^{M} \left(\varepsilon_3 k_o^2 - \tilde{k}_{xm}^{(3)^2}\right) \begin{Bmatrix} \sin\left[\tilde{k}_{xm}^{(3)}(x+a)\right] \\ \cos\left[\tilde{k}_{xm}^{(3)}(x+a)\right] \end{Bmatrix} L_m = \sum_{m=1}^{M'} \left(\varepsilon_i k_o^2 - \tilde{k}_{xm}^{(i)^2}\right)$$

$$\tilde{\phi}_{h,m}^{(i)}(x)(J_m - J_m') \qquad (A-6)$$

136

$$\sum_{n=0}^{N} k_z k_{xn}^{(3)} \begin{Bmatrix} -\sin\left[k_{xn}^{(3)}(x+a)\right] \\ \cos\left[k_{xn}^{(3)}(x+a)\right] \end{Bmatrix} K_n - \sum_{m=0}^{M} \omega\mu_o \tilde{k}_{ym}^{(3)} \begin{Bmatrix} \sin\left[\tilde{k}_{xm}^{(3)}(x+a)\right] \\ \cos\left[\tilde{k}_{xm}^{(3)}(x+a)\right] \end{Bmatrix}$$

$$\cdot \tan\left[\tilde{k}_{ym}^{(3)}(-h+1)\right] L_m = \sum_{n=1}^{N'} k_z \frac{\partial\phi_{e,n}^{(i)}(x)}{\partial x} (-I_n + I_n')$$

$$+ \sum_{m=0}^{M} \omega\mu_o \tilde{k}_{ym} \tilde{\phi}_{h,m}^{(i)}(x)(\tan(\tilde{k}_{ym}h) J_m + \cot(\tilde{k}_{ym}h) J_m') \qquad (A-7)$$

$$\sum_{n=0}^{N} \omega\varepsilon_o\varepsilon_3 k_{yn}^{(3)} \begin{Bmatrix} \cos\left[k_{xn}^{(3)}(x+a)\right] \\ \sin\left[k_{xn}^{(3)}(x+a)\right] \end{Bmatrix} \cot\left[k_{yn}^{(3)}(-h+1)\right] K_n$$

$$+ \sum_{m=0}^{M} k_z \tilde{k}_{xm}^{(3)} \begin{Bmatrix} \cos\left[\tilde{k}_{xm}^{(3)}(x+a)\right] \\ -\sin\left[\tilde{k}_{xm}^{(3)}(x+a)\right] \end{Bmatrix} L_m = \sum_{n=1}^{N'} \omega\varepsilon_o\varepsilon_i k_{yn} \phi_{e,n}^{(1)}(x)$$

$$\cdot (\cot(k_{yn}h) I_n + \tan(k_{yn}h) I_n') + \sum_{m=1}^{M'} k_z \frac{\partial\phi_{h,m}^{(i)}(x)}{\partial x} (J_m - J_m')$$

$$(A-8)$$

The upper line in the brackets indicates the pec wall at x = -a while the lower line applies for a pmc wall. The $\phi_{e,n}^{(i)}(x)$ and $\phi_{h,m}^{(i)}(x)$, i = 2,4,5, are the x-variation components of the Hertzian potentials in respective regions (see Eqs. (3), (4), and (5)). ε_i, i = 2,4,5, is the relative dielectric constant.

APPENDIX B

COUPLING INTEGRAL TERMS

$$P_n(\nu) = \left[k_o^2 - k_{xn}^{(4)^2}\right] K_n^{(G-I)} I_1(\nu) + \left[\varepsilon_2 k_o^2 - k_{xn}^{(2)^2}\right]$$

$$\cdot \left\{ K_n^{(C-I)} I_2(\nu) + K_n^{(D-I)} I_3(\nu) + \left[k_o^2 - k_{xn}^{(5)^2}\right] I_4(\nu) \right.$$

$$R_n(\nu) = K_n^{(G-I)} I_1(\nu) + \varepsilon_2\left\{K_n^{(C-I)} I_2(\nu) + K_n^{(D-I)} I_3(\nu)\right\} + I_4(\nu)$$

$$T_n(\nu) = \begin{Bmatrix} 1 \\ -1 \end{Bmatrix} k_{xn}^{(4)} K_n^{(G-I)} I_5(\nu) + \left[k_{xn}^{(2)} K_n^{(C-I)} I_6(\nu) \right.$$

$$\left. - K_n^{(D-I)} I_7(\nu) \right] + k_{xn}^{(5)} I_8(\nu)$$

$$Q_m(\mu) = \left[k_o^2 - \tilde{k}_{xm}^{(4)^2}\right] K_m^{(H-J)} \tilde{I}_5(\mu) + \left[\varepsilon_2 k_o^2 - \tilde{k}_{xm}^{(2)^2}\right]$$

$$\cdot \left\{ K_m^{(E-J)} \tilde{I}_6(\mu) + K_m^{(F-J)} \tilde{I}_7(\mu) \right\} + \left[k_o^2 - \tilde{k}_{xm}^{(5)^2}\right] I_8(\nu)$$

$$S_m(\mu) = \begin{Bmatrix} 1 \\ -1 \end{Bmatrix} \tilde{k}_{xm}^{(4)} K_m^{(H-J)} \tilde{I}_1(\mu) + \tilde{k}_{xm}^{(2)}\left\{K_m^{(E-J)} \tilde{I}_2(\mu) \right.$$

$$\left. - K_m^{(F-J)} \tilde{I}_3(\mu) \right] + \tilde{k}_{xm}^{(5)} \tilde{I}_4(\mu)$$

$$U_m(\mu) = K_m^{(H-J)} \tilde{I}_5(\mu) + K_m^{(E-J)} \tilde{I}_6(\mu) + K_m^{(F-J)} \tilde{I}_7(\mu) + \tilde{I}_8(\mu)$$

and

<u>LSM modes</u>

$$I_1(\nu) = \int_{-a}^{-w} \begin{Bmatrix} \cos\left[k_{xn}^{(4)} (x+a)\right] \\ \sin\left[k_{xn}^{(4)} (x+a)\right] \end{Bmatrix} \psi_j^{(1)}(x) \, dx$$

$$I_2(\nu) = \int_{-w}^{w} \cos\left[k_{xn}^{(2)}x\right] \psi_\nu^{(1)}(x) \; dx$$

$$I_3(\nu) = \int_{-w}^{w} \sin\left[k_{xn}^{(2)}x\right] \psi_\nu^{(1)}(x) \; dx$$

$$I_4(\nu) = \int_{w}^{b} \cos\left[k_{xn}^{(5)}(x-b)\right] \psi_\nu^{(1)}(x) \; dx$$

$$I_5(\nu) = \int_{-a}^{-w} \left\{ \begin{array}{c} \sin\left[k_{xn}^{(4)}(x+a)\right] \\ \cos\left[k_{xn}^{(4)}(x+a)\right] \end{array} \right\} \psi_\nu^{(2)}(x) \; dx$$

$$I_6(\nu) = \int_{-w}^{w} \sin\left[k_{xn}^{(2)}x\right] \psi_\nu^{(2)}(x) \; dx$$

$$I_7(\nu) = \int_{-w}^{w} \cos\left[k_{xn}^{(2)}x\right] \psi_\nu^{(2)}(x) \; dx$$

$$I_8(\nu) = \int_{w}^{b} \sin\left[k_{xn}^{(5)}(x-b)\right] \psi_\nu^{(2)}(x) \; dx$$

where

$$\psi_\nu^{(1)}(x) = \left\{ \begin{array}{c} \cos\left[k_{x\nu}^{(1)}(x+a)\right] \\ \sin\left[k_{x\nu}^{(1)}(x+a)\right] \end{array} \right\}$$

$$\psi_\nu^{(2)}(x) = \left\{ \begin{array}{c} \sin\left[k_{x\nu}^{(1)}(x+a)\right] \\ \cos\left[k_{x\nu}^{(1)}(x+a)\right] \end{array} \right\}$$

LSE modes

$\tilde{I}_1(\mu), \ldots, \tilde{I}_8(\mu)$ are obtained by replacing $k_{xn}^{(i)}$ in $I_1(\nu), \ldots, I_8(\nu)$ with $\tilde{k}_{xm}^{(i)}$; $\psi_\nu^{(i)}(x)$ by $\psi_\mu^{(i)}(x)$, e.g.,

$$\tilde{I}_8(\mu) = \int_w^b \sin\left[\tilde{k}_{xm}^{(5)}(x-b)\right] \begin{Bmatrix} \sin\left[\tilde{k}_{xu}^{(1)}(x+a)\right] \\ \cos\left[\tilde{k}_{x\mu}^{(1)}(x+a)\right] \end{Bmatrix} dx$$

In these equations, the upper line in { } applies to pec wall (odd mode) at $x = -a$, and the lower line to pmc wall (even mode) at $x = -a$. $k_{xn}^{(i)}$ and $\tilde{k}_{xm}^{(i)}$ are the solutions of the eigenvalue equations (8) and (9). $k_{x\nu}^{(1)}$ and $\tilde{k}_{x\mu}^{(1)}$ are given in (7). $K_n^{(C-I)}, \ldots, K_m^{(F-J)}$ are the coupling terms described in Eqs. (14) and (16).

REFERENCES

[1]   M.V. Schneider, "Millimeter-wave integrated circuits," 1973
       IEEE MTT-S Intl. Microwave Symp. Digest, Boulder, Co., June
       4-6, 1973.

[2]   J.A. Paul and Y-W. Chang, "Millimeter-wave image guide integrated
       passive devices," IEEE Trans. Microwave Theory Tech., vol. MTT-23,
       no. 10, pp. 751-754, October 1978.

[3]   R.M. Knox and P.O. Toulios, "Integrated circuits for the millimeter
       through optical frequency range," in Symp. on Submillimeter Waves,
       New York: Polytechnic Press, pp. 497-516, 1970.

[4]   W. McLevige, T. Itoh and R. Mittra, "New waveguide structures for
       millimeter-wave and optical integrated circuits,' IEEE Trans.
       Microwave Theory Tech., vol. MTT-23, no. 10, pp. 788-794,
       October 1975.

[5]   J.W. Griemsman and L. Birenbaum, "A low-loss H-guide for milli-
       meter wavelengths," in Symp. on Submillimeter Waves, New York:
       Polytechnic Press, pp. 543-562, 1959.

[6]   T. Itoh and B. Adelseck, "Trapped image guide for millimeter-
       wave circuits," IEEE Trans. Microwave Theory Tech., vol. MTT-28,
       pp. 1433-1436, December 1980.

[7]   T. Itoh, "Inverted strip dielectric waveguide for millimeter-
       wave integrated circuits," IEEE Trans. Microwave Theory Tech.,
       vol. MTT-23, no. 11, pp. 821-827, November 1976.

[8]   R.M. Knox, "Dielectric waveguide microwave intregrated circuits -
       An overview," IEEE Trans. Microwave Theory Tech., vol. MTT-24,
       no. 11, pp. 806-814, November 1976.

[9]   R. Mendenez, R. Mittra, P. Yang and N. Deo, "Effective graded-index guides for millimeter-wave applications," IEE J. Microwaves, Opt. and Acoust., vol. 3, no. 2, pp. 51-55, March 1979.

[10]   W. Schlosser and H.G. Unger, "Partially filled waveguides and surface waveguides of rectangular cross section," in Advances in Microwaves, New York: Academic Press, pp. 319-387, 1966.

[11]   K. Solback and I. Wolff, "Electromagnetic fields and the phase constants of dielectric image lines," IEEE Trans. Microwave Theory Tech., vol. MTT-26, no. 4, pp. 266-274, April 1978.

[12]   R. Mittra, Y.L. Hou and V. Jamnejad, "Analysis of open dielectric waveguides using mode matching technique and variational methods," IEEE Trans. Microwave Theory Tech., vol. MTT-28, no. 1, pp. 36-43, January 1980.

[13]   N.C. Deo, "Theoretical and experimental study of millimeter-wave integrated circuits," Ph.D. Thesis, Department of Electrical Engineering, University of Illinois, Urbana, 1980.

[14]   U. Crombach, "Analysis of single and coupled rectangular dielectric waveguides," IEEE Trans. Microwave Theory Tech., vol. MTT-29, no. 9, pp. 870-874, September 1981.

[15]   S. T. Peng and A. A. Oliner, " Guidance and leakage properties of a class of open dielectric waveguides, Part I - Mathematical Formulations," IEEE Trans. Microwave Theory Tech., vol. MTT-29, no. 9, pp. 843-854, September 1981.

[16]   R.E. Collin, Field theory of guided waves. New York: McGraw-Hill, 1960, ch. 6.

[17]   P. Yang, "A new method for the analysis of dielectric waveguides for millimeter-wave and optical integrated circuits," Coordinated Science Laboratory Report, R-813, University of Illinois at Urbana-Champaign, May 1978.

[18]   E.A. Marcatili, "Dielectric rectangular waveguide and directional coupler for integrated optics," Bell Syst. Tech. J., vol. 48, no. 7, pp. 2071-2102, 1969.

[19]   J.E. Goell, "A circular-harmonic computer analysis of rectangular dielectric waveguides," Bell Syst. Tech. J., vol. 48, no. 7, pp. 2133-2160, September 1969.

[20]   R.F. Harrington, Time harmonic electromagnetic fields. New York: McGraw-Hill, 1961, ch. 7.

[21]   J.W. Wilson, "Analysis of fin-line at millimeter wavelengths," Master's Thesis, Department of Electrical Engineering, University of Illinois at Urbana-Champaign, 1982.

[22]   S. Shindo and T. Itanani, "Low-loss rectangular dielectric image line of millimeter-wave integrated circuits," IEEE Trans. Microwave Theory Tech., vol. MTT-26, no. 10, pp. 747-751, October 1978.

[23]   R.E. Horn, H. Jacobs, E. Freibergs and K.L. Klohn, "Electronic modulated beam-steerable silicon waveguide array antenna," IEEE Trans. Microwave Theory Tech., vol. MTT-28, no. 6, pp. 647-653, June 1980.

[24]   B.J. Levin and J.E. Kietzer, "Hybrid millimeter-wave integrated circuits," U.S. Army Electronics Command. Research and Development Technical Report No. ECOM-74-0577-F, July 1975.

[25] H. Jacobs and M.M. Chrepta, "Electronic phase shifter for millimeter-wave semiconductor dielectric integrated circuits," IEEE Trans. Microwave Theory Tech., vol. MTT-22, no. 4, pp. 411-417, April 1974.

[26] T.N. Trinh, R. Mittra and R.J. Paleta, "Horn image guide leaky-wave antenna," IEEE Trans. Microwave Theory Tech., vol. MTT-29, no. 12, pp. 1310-1314, December 1981.

[27] M. Desai and R. Mittra, "A method for reducing radiation losses at bends in open dielectric structures." 1980 IEEE MTT-S Intl. Microwave Symp. Digest, Washington, D.C., pp. 212-213, May 1980.

[28] E.A.J. Marcatili and S.E. Miller, "Improved relations describing directional control in electromagnetic waveguidance," Bell Syst. Tech. J., vol. 48, no. 7, pp. 2161-2188, September 1969.

[29] D. Marcuse, "Bending loss of the asymmetric slab waveguide," Bell Syst. Tech. J., vol. 50, pp. 2551-2563, 1971.

[30] F.J. Tischer, "Properties of the H-guide at microwave and milli-meter-wave regions," Proc. IEE, Suppl. 13, pp. 47-53, 1959.

[31] V.R. Bui and R.R.J. Gagné, "Dielectric losses in an H-plane-loaded rectangular guide," IEEE Trans. Microwave Theory Tech. (short papers), vol. MTT-20, pp. 621-623, September 1972.

[32] P.P. Toulios and R.M. Knox, "Rectangular dielectric image lines for millimeter-wave integrated circuits," Proc. of Western Electronics Show and Convention, Los Angeles, California. vol. 14, pp. 3/3-1 to 10, August 25-28, 1970.

[33] S.K. Chatterjee and R. Chatterjee, "Dielectric loaded waveguides –
      A review of theoretical solutions," Radio Electron. Eng., vol.
      30, pp. 259-288, November 1965.

[34] M. Abramovitz and I.A. Stegun, Handbook of Mathematical Functions,
      U.S. Dept. of Commerce, Nat. Bur. of Stand., 10th ed., 1972.

[35] F.J. Tischer, "Excess conduction losses at millimeter wavelengths,"
      IEEE Trans. Microwave Theory Tech., vol. MTT-20, no. 11,
      pp. 853-858, November 1976.

[36] T. Itanami and S. Shindo, "Channel dropping filter for millimeter-
      wave integrated circuits," IEEE Trans. Microwave Theory Tech.,
      vol. MTT-26, no. 10, pp. 759-764.

[37] K. Solbach, "The calculation and the measurement of the coupling
      properties of dielectric image lines of rectangular cross section,"
      IEEE Trans. Microwave Theory Tech., vol. MTT-27, no. 1, pp. 54-58,
      January 1979.

[38] T.N. Trinh and R. Mittra, "Coupling characteristics of planar
      dielectric waveguides of rectangular cross section," IEEE Trans.
      Microwave Theory Tech., vol. MTT-29, no. 9, pp. 875-880,
      September 1981.

[39] V.P. Nanda, "A new form of ferrite device for millimeter-wave
      integrated circuits," IEEE Trans. Microwave Theory Tech., vol.
      MTT-24, no. 11, pp. 876-879, November 1976.

[40] K. Araki and T. Itoh, "Analysis of periodic ferrite slab waveguides
      by means of improved perturbation method," IEEE Trans. Microwave
      Theory Tech., vol. MTT-29, no. 9, pp. 911-916, September 1981.

[41] H. Jacobs and M. Chrepta, "Electronic phase shifter for millimeter-
      wave semiconductor dielectric integrated circuits," IEEE Trans.
      Microwave Theory Tech., vol. MTT-22, no. 4, pp. 411-417, April 1974.

[42] T. Itoh, "Applications of gratings in a dielectric waveguide for
      leaky-wave antennas and band-reject filters," IEEE Trans.
      Microwave Theory Tech., vol. MTT-25, no. 12, pp. 1134-1138,
      December 1977.

[43] S. Ray, R. Mittra, T.N. Trinh and R.J. Paleta, "Recent developments
      in the millimeter wave antennas," in 1981 Proc. Antenna Applications
      Symp., Univ. of Illinois, September 1981.

[44] S.B. Cohn, "Microwave bandpass filters containing high-Q dielectric
      resonators," IEEE Trans. Microwave Theory Tech., vol. MTT-16,
      pp. 218-299, April 1968.

[45] Y. Garrault and P. Guillon, "Higher accuracy for the resonance
      frequencies of dielectric resonators," Electron. Lett., vol. 12,
      no. 18, pp. 475-476, September 1976.

[46] Y. Konishi, N. Hoshino and Y. Utsumi, "Resonant frequency of a
      $TE_{01\delta}^{o}$ dielectric resonator," IEEE Trans. Microwave Theory Tech.,
      vol. MTT-24, no. 2, pp. 112-114, February 1976.

[47] T. Itoh and R.S. Rudokas, "New method for computing the resonant
      frequencies of dielectric resonators," IEEE Trans. Microwave
      Theory Tech., vol. MTT-25, no. 1, pp. 52-54, January 1977.

[48] R.F. Harrington, Time Harmonic Electromagnetic Fields. New York:
      McGraw-Hill, 1961, ch. 5.

[49]   S.F. Adam, Microwave Theory and Applications. New Jersey:

       Prentice-Hall, 1969, ch. 3.

[50]   R. Levy, "Directional Coupler," in Advances in Microwaves, vol.

       1. New York: Academic Press, 1966, pp. 115-209.

[51]   K. Tomiyasu and S.B. Cohn, "The transvar directional coupler,"

       Proc. IRE, no. 41, pp. 922-926, 1953.

[52]   R. Mittra and R. Kastner, "A spectral domain approach for computing

       the radiation characteristics of a leaky-wave antenna for milli-

       meter-waves," IEEE Trans. Antenna Propagat., vol. AP-29, no. 4,

       pp. 652-654, July 1981.

[53]   K. Ogusu, "Propagation properties of a planar dielectric wave-

       guide with periodic metallic strips," IEEE Trans. Microwave

       Theory Tech., vol. MTT-29, no. 1, pp. 16-21, January 1981.

[54]   J. Arnaud, "Periodic structures," in Cross-Field Microwave

       Devices, vol. 1, E. Okress, Ed. New York: Academic Press, 1961,

       ch. 2.

[55]   T. Tamir and H.L. Bertoni, "Unified theory of optical-beam couplers,"

       in Digest. Tech. Papers, Topical Meet. on Integrated Optics-Guided

       Waves, Materials and Devices, (Las Vegas, NV, 1972).

[56]   R.E. Collin and F.J. Zucker, Antenna Theory, vol. 2. New York:

       McGraw-Hill, 1969, ch. 19, 20.

[57]   W.L. Weeks, Antenna Engineering. New York: McGraw-Hill, 1968,

       ch. 6.

[58]   S.A. Schelkunoff and H.T. Fris, Antennas: Theory and Practice.

       New York: Wiley, 1952, ch. 16.

END

FILMED

8